EUROPEAN COMMISSION

Community Research

TIMODAZ

Thermal Impact on the Damaged Zone Around a Radioactive Waste Disposal in Clay Host Rocks

(Contract Number : FI6W-CT-2007-036449)

Deliverable D13 – Simulation of lab and in situ tests

Editor(s): **Robert Charlier**

Authors : Robert Charlier, René Chambon, Frédéric Collin, Fabian Dedecker, Arnaud Dizier, Suzanne Fauriel, Bertrand François, Jan Fokkens, Benoit Garitte, Antonio Gens, Pierre Gérard, Chen Guangjing, Lyesse Laloui, Xiang-Ling Li, Yu Li, Severine Levasseur, Ferdinando Marinelli, Thibaut Meynet, Jean-Pol Radu, Yannick Sieffert, Xavier Sillen, Philippe Van Marcke, Jean Vaunat, Tim Vietor, Lian Wang, Chunliang Zhang

Laboratories: CIMNE, ESV EURIDICE GIE, EPFL, ULg, GRS, UJF, NAGRA, NRG, SCK-CEN, ITASCA

Reporting period: **01/10/2009 - 31/03/2010**

Date of issue of this report: **31/08/2010**

Start date of project: **01/10/2006** Duration : **48** Months

Project co-funded by the European Commission under the Euratom Research and Training Programme on Nuclear Energy within the Sixth Framework Programme (2002-2006)		
Dissemination Level		
PU	Public	PU
RE	restricted to a group specified by the partners of the TIMODAZ project	
CO	confidential, only for partners of the TIMODAZ project	

DISTRIBUTION LIST

Name	Number of copies	Comments
Mr. Christophe Davies (European Commission)	One electronic copy on CIRCA One paper copy	
All consortium members	One electronic copy available on the restricted area of the TIMODAZ web portal	

1 Introduction

This report is concerned with the Timodaz work package WP 5.2. This work package was proposed in order to allow better understanding and quantifying the thermal impact of heat emitting radioactive waste on the host-rock and the Damaged Zone, and to realise predictive modelling of a repository scale experiment (the PRACLAY experiment). The aim of the work package is to assess the performance of coupled THM analysis, using different codes, of proposed laboratory tests and in situ tests (available and prospective), with a main focus on the development and evolution of the DZ. The modelling work together with the results of the lab and the in-situ tests should give clear indication on the evolution of the DZ with time: What are the risks of fracturation? What are the favourable and the unfavourable effects of the thermal load on sealing? What are the THMC governing processes and parameters at repository time and spatial scale?

Description of work

The modelling work focuses on the following topics:

- Investigation of the thermal impact on EDZ
- Investigation of possible additional damage due to thermal load
- Transition between brittle and visco-plastic behaviour due to thermal loading
- Difference between continuum modelling and discrete element modelling

Different codes are evaluated by participation in Benchmark exercises for modelling of THM processes in clays. The benchmarks allow to assess the influence of the constitutive laws on the long term and large scale predictions, and to see if different modelling teams using different codes and/or constitutive laws can obtain similar predictions. The work package is divided in three tasks:

Task1: Benchmark 1: laboratory experiments modelling

The benchmark 1 consists in modelling the simulation tests performed in laboratory (see Deliverable D7 and sub-work package 3.3) on Boom Clay, Opalinus Clay and Callovo-Oxfordian Argillite.

Task 2: Benchmark 2: small scale in-situ experiments modelling

The benchmark 2 consists in modelling the small scale in situ tests performed in sub-work package 4.2., i.e. the Mt. Terri experiment and the Atlas experiment

Task 3: Blind prediction of the PRACLAY experiment

This task consists mainly in, using different codes, blind prediction of the large scale heater test PRACALY experiment.

The deliverable reports the numerous numerical simulations done by the Timodaz partners. Full length description is reported in 5 extensive annexes, where the reader can find any detail of interest. We have here only reported short synthesis of the full work.

2 Simulation of hollow cylinder tests

2.1 Boom Clay

2.1.1 Introduction

In the context of the TIMODAZ project, hollow cylinder tests have been designed and performed on Boom Clay in the framework of the workpackage WP3.3. The experiment has been developed to study the fracturing and others irreversible processes that develop in the Excavation Damaged Zone (EDZ) around galleries in clayey formations and the impact of a thermal phase on their evolution. It consists in hollow cylinder samples of Boom Clay which are submitted to mechanical and thermal loadings fairly similar to the evolution that will be encountered around disposal galleries for heat emitting radioactive waste. In parallel to the experimental aspects, numerical simulations was performed in order, first, to predict the expected thermo-hydro-mechanical behaviour of Boom Clay in the experiment and, then, to interpret the obtained results in term of constitutive behavioural features.

In the definition of the time schedule of WP 5.2, it has been decided to perform the numerical simulations in parallel with the design and the carrying out of the experiment. So doing, a benchmark exercise has been proposed to the team involved in the numerical modelling of the hollow cylinder on Boom Clay. This exercise has been defined in agreement with the planned experimental procedure, in term of thermo-hydro-mechanical conditions. However, in the course of the design of the experiment, the conditions have been slightly modified, which explain the small difference between the conditions applied during the tests and for the numerical simulations.

In a second step, in addition to the benchmark exercise, as series of additional computations have been carried out in order to study some more specific features of behaviour that have been underlined during the experiment. Those simulations consist, for most of them, in an analysis and a constitutive interpretation of experimental results in order to validate and calibrate the used numerical models and materials parameters. For this step of the work, the liberty was given to use the constitutive models, the geometry of the mesh and the boundary conditions that each team considers as the most appropriate regarding to the features of behaviour that they expected to observe. Also, for this part, the boundary conditions have been taken in agreement with the experimental conditions.

This executive summary presents the main concepts and results that have been obtained in the framework of the numerical modelling of the hollow cylinder experiment on Boom Clay. It is divided in two parts: the benchmark exercise and the additional computations.

2.1.2 The benchmark exercise

Problem definition

The problem is treated as a one dimensional process (radial-axisymmetric) that is an idealization of the hollow cylinder sample of a porous isotropic medium. At the inner end of the mesh, the boundary conditions is governed by the evolution of radial stress, pore water pressure and temperature imposed while the THM conditions at the outer end is kept constant, corresponding to the in-situ conditions of Boom Clay at the depth of the repository.

The geometry, the initial and the boundary conditions of the sample are illustrated in Figure 1(a). The internal radius R_i is equal to 7 mm and the external radius R_e to 43 mm. The clay is supposed to be homogeneous and isotropic. It is considered to be fully saturated. The considered initial conditions (isotropic total stress field of 4.5 MPa and pore water pressure of 2.2 MPa) are close to the one encountered in Boom Clay at the depth of the repository. This modelling includes two steps: the first one represents the process of excavation under isothermal condition and during the second step a thermal loading is applied at the inner cavity of the cylinder (Figure 1(b)).

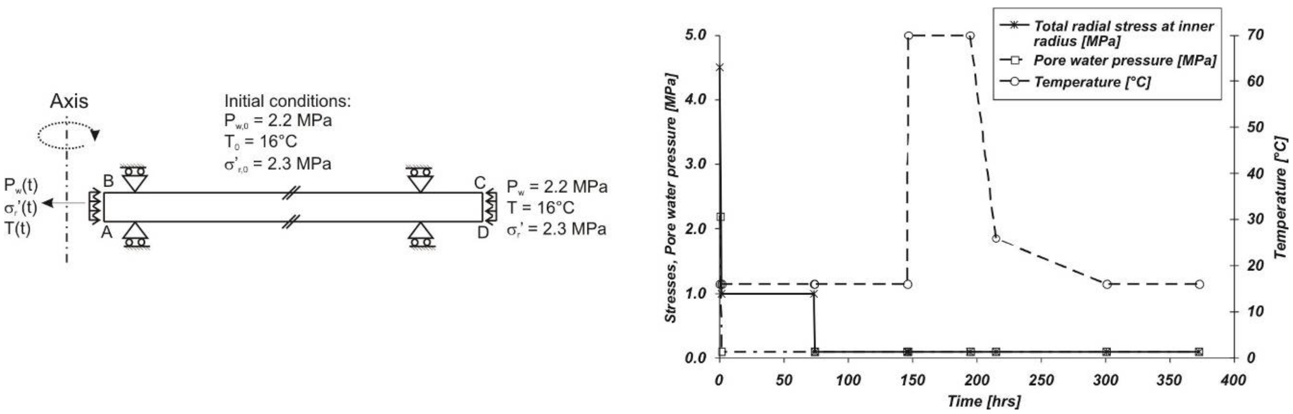

Figure 1: Geometry, initial and boundary conditions (a). THM loading paths (b)

Governing equations and parameters

The mechanical model used for the plastic clay is a non-associated elastoplastic constitutive law. The yield surface is defined by a Drucker-Prager criterion characterized by a circle in the deviatoric plane. The Drucker-Prager yield limit is given by the following equation:

$$f \equiv II_{\hat{\sigma}} + m\left(I_{\sigma} - \frac{3c}{\tan\phi_c} \right) = 0 \tag{0.1}$$

with ϕ_c the friction angle in compression and c the cohesion, $I_{\sigma} = \sigma_{ii}$ the first stress invariant, $II_{\hat{\sigma}} = \sqrt{\frac{1}{2}\hat{\sigma}_{ij}\hat{\sigma}_{ij}}$ the second deviatoric stress invariant with $\hat{\sigma}_{ij} = \sigma_{ij} - \frac{I_{\sigma}}{3}\delta_{ij}$ and $m = \frac{2\sin\varphi_c}{\sqrt{3}(3-\sin\varphi_c)}$.

In this modelling, two processes of isotropic hardening (friction angle) and softening (cohesion) are possible. Thus, different cases will be considered as a function of the hardening/softening. The thermo-mechanical model is based on thermo-elasticity. So, the thermal strain is defined as $\dot{\varepsilon}_{ij}^{e,th} = \beta_s \dot{T} \delta_{ij}$ where β_s is the solid thermal expansion coefficient and δ_{ij} is the Kronecker symbol.

The field equations consider the medium as a deformable two-phases material (i.e., a water saturated medium) in which mass transfers occur. The general Darcy flow law is used and defines the Darcy fluid velocity $\underline{q}_w$ as a linear function of permeability and the gradient of fluid pressure p_w :

$$\underline{q}_w = -\frac{k_{\text{int}}}{\mu_w}(\nabla p_w) \tag{0.2}$$

where k_{int} is the intrinsic permeability and is considered as a scalar in isotropic situation. μ_w is the fluid dynamic viscosity which is supposed to be linearly dependent of temperature following:

$$\mu_w(T) = \mu_{w0} - \alpha_w \mu_{w0}(T - T_0) \tag{0.3}$$

where α_w is the liquid dynamic viscosity thermal coefficient.

In order to investigate the modification of the permeability in the damage zone, a modification of the permeability with the porosity is taken into account. In this model, two cases can be studied:

- The permeability k_{int} is constant: $k_{\text{int}} = k_{\text{int}}^{sat}$
- The permeability k_{int} is a function of porosity: $k_{\text{int}} = k_{\text{int}}^{sat}.k_{r,n}$,

with:

$$k_{r,n} = 1 \qquad \text{if } n - n_0 < 0$$

$$k_{r,n} = 1 + 2.10^9 (n - n_0)^3 \qquad \text{if } 0 < n - n_0 < 10^{-2}$$

$$k_{r,n} = 1 + 2.10^3 \qquad \text{if } n - n_0 > 10^{-2}$$

The heat flow is governed by the following equation:

$$q_T = -\Gamma.\underline{\nabla} T + c_{p,w}.\rho_w.\underline{q}_w.(T - T_0) \tag{0.4}$$

where Γ is the thermal conductivity of the saturated material, $c_{p,w}$ the heat capacity of water and ρ_w the density of water.

The material parameters are summarized in Table 1 and Table 2. Let's note that four different versions of the Drucker-Prager model have been considered. Case A is the elastic perfectly plastic model. Case B considers a friction angle hardening elastoplastic model. Case C corresponds to a combination of a friction angle hardening elastoplastic model with cohesion softening. Finally case D is the same elastoplastic model as case C but the permeability is considered as a function of the porosity.

Geomechanical characteristics		Case A	Case B	Cases C and D
Young elastic modulus [MPa]	E_0	300	300	300
Poisson ratio [-]	υ	0.125	0.125	0.125
Specific mass [kg/m³]	ρ	2682	2682	2682
Initial cohesion [kPa]	c_0	300	300	300
Final cohesion [kPa]	c_f	300	300	100
Softening parameter [-]	β_c	-	-	0.01
Initial friction angle [°]	ϕ_{c0}	18	5	5
Final friction angle [°]	ϕ_{cf}	18	18	18
Hardening parameter [-]	β_ϕ	-	0.01	0.01
Dilatation angle [°]	ψ	0	0	0

Table 1: Geomechanical characteristics

Hydraulic characteristics		
Initial porosity	n_0	0.39
Initial intrinsic permeability [m²]	k_{int}^{sat}	4.10^{-19}
Water specific mass [kg/m³]	ρ_w	1000
Fluid dynamic viscosity [Pa.s]	μ_w	10^{-3}
Liquid compressibility coefficient [MPa^{-1}]	$1/\chi_w$	5.10^{-4}
Thermal characteristics		
Thermal conductivity [W/(mK)]	λ	1.35
Volumetric heat capacity [J m^{-3}.K^{-1}]	ρC_p	2.84E6
Linear solid thermal expansion coefficient [K^{-1}]	β_s	10^{-5}
Volumetric liquid thermal expansion coefficient [K^{-1}]	β_w	3.10^{-4}
Liquid dynamic viscosity thermal coefficient [K^{-1}]	α_w	0.01

Table 2: Hydraulic and thermal characteristics

Results

The first objective of this benchmark exercise was to validate the numerical tools used by the different modelling teams by comparing simulation results of each team (i.e., EPFL, EURIDICE, ULg, UJF and CIMNE). EPFL, UJF and ULg have used the finite element code LAGAMINE while CIMNE and EURIDICE used CODE_BRIGHT.

For the hydro-mechanical parts, the four different versions of the Drucker-Prager model, as defined in Table 1, have been considered by each teams. On the contrary, for the non-isothermal part, Case A was imposed for each team and the liberty was given to consider an additional case per team. So, the comparison between the results of each team was only possible for the perfectly plastic model (case A of Table 1).

In this benchmark, results of each team have been compared in term of the radial profiles of the three principal stresses, the pore water pressure, the radial displacements, the water flux and the temperature. It has been concluded that the results obtained by the different teams are very similar. The only very slight difference comes from the pore water pressure and temperature profiles obtained by CIMNE at the end of the heating phase. However, this discrepancy is really negligible.

The second objective of this benchmark exercise was to evaluate the response of each version of the constitutive model. First, it has been observed that the radial displacement grows with the successive introductions of hardening and softening processes. Also, the increase of water permeability with the porosity (Case D) decreases the final convergence of the hole because of the strengthening effect of the water drainage (Figure 2).

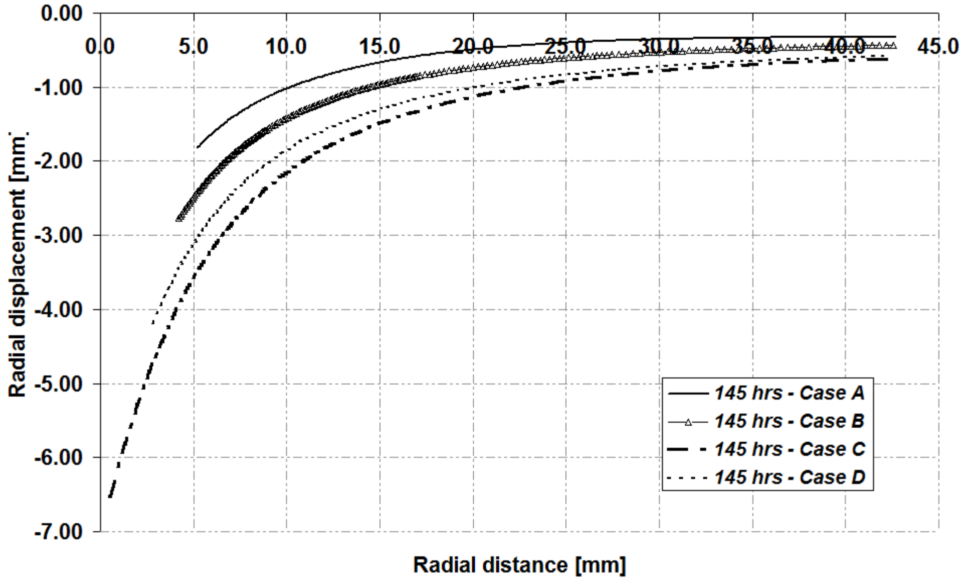

Figure 2: Comparison of the radial displacement profile at the end of the second stabilization period (t = 145 hours) obtained with the four versions of the Drucker-Prager model

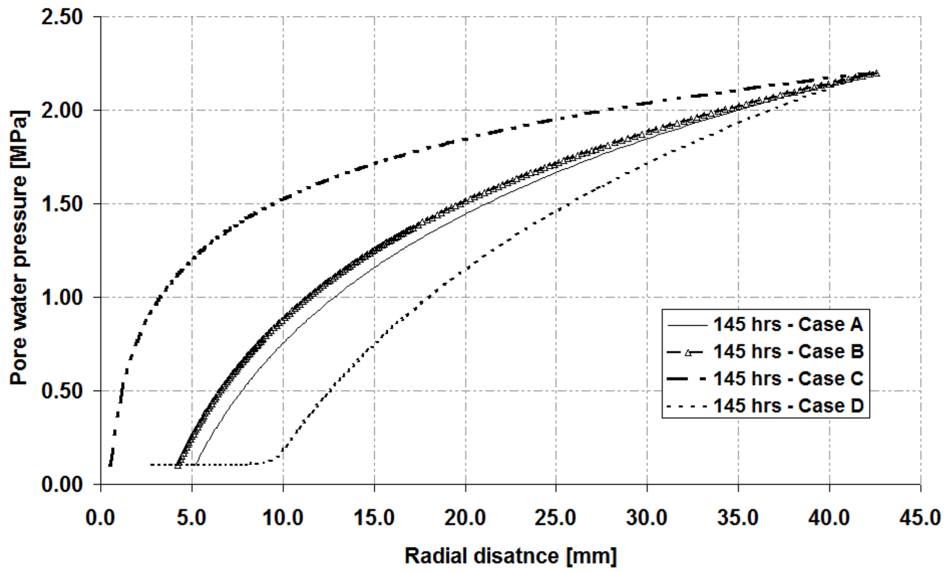

Figure 3: Comparison of the pore water pressure profile at the end of the second stabilization period (t = 145 hours) obtained with the four versions of the Drucker-Prager model

In term of pore water pressure evolution, during the stabilization periods, the pore water pressure reaches equilibrium between the two imposed values at the inner and outer faces. So, at the end of the each stabilization phase, the pore water pressure profile obtained in cases A, B and C are very similar. The only difference is due to the change of the geometry of the cylinder, different with each model. Excepted that, the profile of the pore water pressure at equilibrium is independent of the mechanical and hydraulic parameters, assuming that the Boom Clay characteristics remain homogeneous (Figure 3). Nevertheless, if the damage process induces a modification of the water permeability (i.e., a lost of the sample homogeneity), the pore water pressure at equilibrium is modified, as it is observed in Case D. Also, let's note that the permeability enhancement due to the porosity increase induces a higher level of water flux passing across the hollow cylinder.

In term of the principal stresses (radial, orthoradial and axial stresses), the predicted profile are affected by the plastic processes. Starting from an isotropic stress state, the decrease of the radial effective stress at the inner face produce a stress redistribution and an increase of the orthoradial stress with respect to the axial and radial stresses. As a consequence, the orthoradial stress is the major principal stress. Using the perfectly plastic model (Case A), the plastic zone is clearly identified because of the peak of the orthoradial stress that characterized the limit between the elastic zone (in the external region of the cylinder) and the plastic zone (in the vicinity of the hole). At the end of the second mechanical unloading, the plastic radius is about 35 mm (with respect to the 43 mm of the external radius). On the contrary, the use of hardening/softening model (Case B, C and D) does not allow us to evidence the sharp transition between the elastic and plastic regions. Indeed, due to the progressive mobilization of the plastic mechanisms, it is no longer possible to distinguish a clear elastic zone because the entire domain is plastic. Figure 4 displays the profile of the orthoradial effective stress at the end of the second stabilization period for each case.

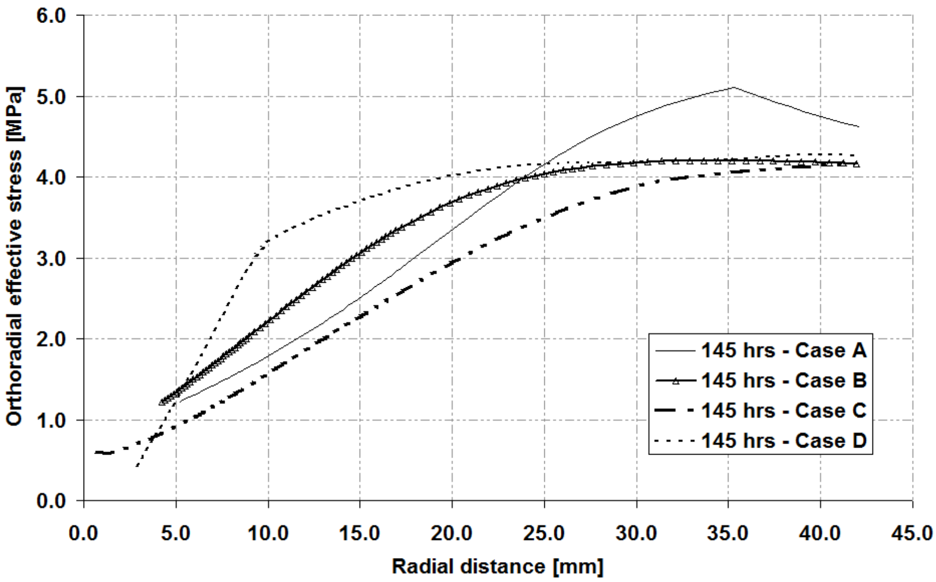

Figure 4: Comparison of the orthoradial effective stress profile at the end of the second stabilization period (t = 145 hours) obtained with the four versions of the Drucker-Prager model

At the inner phase, the process occurs under drained condition and the stress path in the ($I_{\sigma} - II_{\hat{\sigma}}$) plane is at 45° ($dI_{\sigma} = dII_{\hat{\sigma}}$) as long as the stress point remains in the elastic domain, as shown in Figure 5. Then, at the inner face, when plasticity occurs, the increment of deviatoric stress is reduced. Then, the deviatoric stress passes through a peak value and finally decreases. This process occurs along with a strong reduction of the mean effective stress during the mechanical unloading. This reduction of the mean stress induces a porosity increase in the vicinity of the hole. Each version of the model predicts similar trends. The perfectly plastic model predicts the maximum value of deviatoric stress that the material can sustain and the minimum reduction of the mean effective stress. The successive introductions of the friction hardening and then the cohesion softening induce a reduction of the maximum deviatoric stress and an increase of the mean effective stress drop. So, the magnitude of plasticity increases successively between case A, B and C.

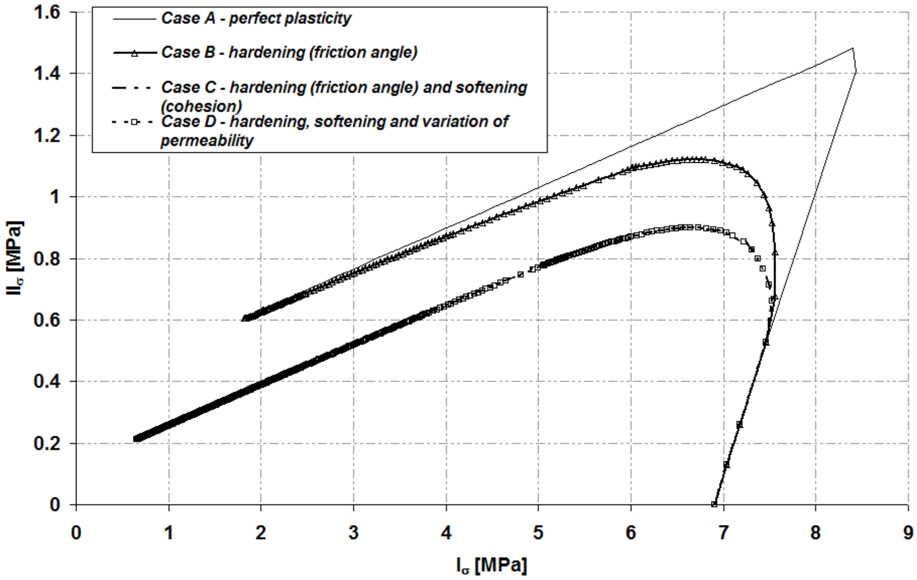

Figure 5: Comparison of the followed stress path stress obtained with the four versions of the Drucker-Prager model

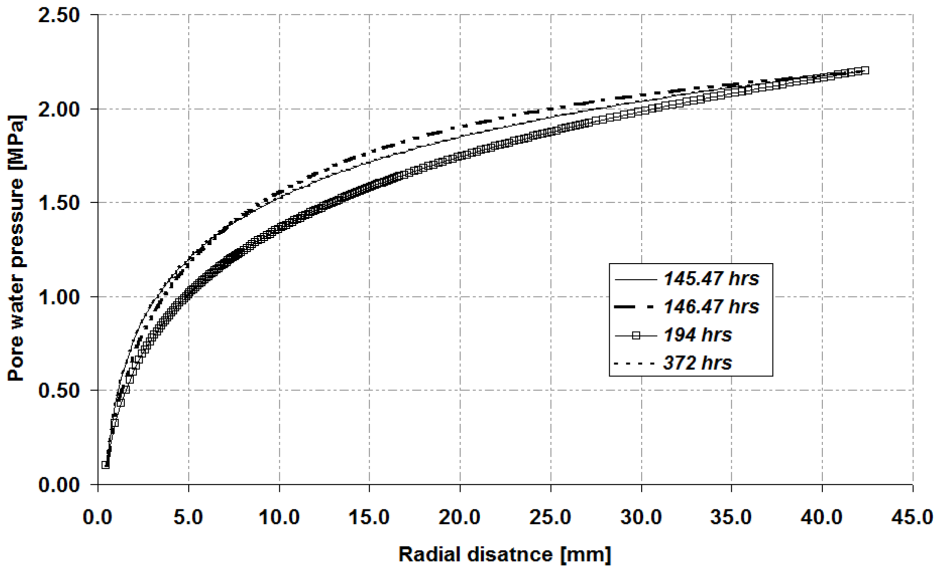

Figure 6: Evolution of pore water pressure with radial distance during the thermal phase in case C. Results obtained in cases A and B are very similar

During the thermal phase, the higher thermal expansion of water than that of the solid skeleton induces pore water pressure increase in the hollow cylinder (Figure 6, t = 146,47 hrs). Then, during the thermal stabilization, the thermal increment of the pore water pressure dissipates and a new pore water pressure profile is reached. The pore water pressure at high temperature is slightly lower than the one at ambient temperature (Figure 6, t = 194 hrs) because of the enhancement of water permeability with temperature that is more important in the vicinity of the hole (because temperature is higher). Finally, after cooling, the pore water pressure profile before heating is recovered (Figure 6, t = 372 hrs). The prediction of the temperature profile and pore water pressure in the four cases are very similar. With the used constitutive models and the imposed boundary conditions, the hydro-mechanical processes that occur in the hollow cylinder during the thermal cycle appear to be reversible because the followed stress path takes place in the elastic domain.

2.1.3 Additional computations

In addition to the benchmark exercise, when the first experimental results have been obtained, it has been decided to perform additional computations in order to reproduce some of the experimental observations that were not considered in the benchmark statement. Each modelling team has considered their own model, set of parameters and geometry that they considered has the most appropriate or relevant to reproduce the experimental observations.

ULg addressed three distinct aspects. (i) Applying the same geometry and boundary conditions that the ones defined in the benchmark exercise, a Mohr-Coulomb criterion, in stead of the Drucker-Prager yield limit, has been considered. (ii) Then, in order to study a possible anisotropic response of the Boom-Clay, numerical simulations considering 2D plane strain problem have been performed. (iii) Finally, 2D axisymmetric conditions have been assumed in order to study the effects of axial boundary conditions on the behaviour of the mid-plane section.

The Soil Mechanics Laboratory of EPFL has performed the simulations of the hollow cylinder tests considering the parameters of Boom Clay with the ACMEG-T model, in addition to the Drucker-Prager model. This model considers non-linear elasticity, hardening and/or softening irreversible processes, multi-mechanism plasticity, a progressive mobilization of plasticity inside the external yield limit and the possible irreversible strain induced by thermal loading (thermo-plasticity).

EURIDICE performed two kinds of simulation using successively a 2D plane strain model and a 2D axisymmetric model. The first one aims at studying the role of elastic cross-anisotropy on the global elasto-plastic response of Boom Clay while the latter one has been done in order to evaluate the relevance of the plane strain assumptions with respect to the real axial strain conditions.

UJF has simulated the effect of strain softening and strain localization on the global response of the hollow cylinder, assuming 2D plane strain conditions and cross-anisotropic elasticity coupled with a Drucker-Prager plastic model. To describe the post-peak behaviour, where the localized zones appear, a second gradient model is added to the mechanical part.

CIMNE has implemented and used a anisotropic linear elastic law with a perfect plastic Mohr Coulomb type yield surface and non associated plasticity allowing null volumetric plastic strain. A number of simulation has shown the effect of each ingredient, with comparison with the experimental results.

In the following sub-sections, the main conclusions of each modelling teams are successively presented.

EPFL contributions

The Soil Mechanics Laboratory of EPFL has performed the simulations of the hollow cylinder tests as defined in the benchmark statement with the ACMEG-T model and compares the obtained results with the prediction of the perfectly plastic Drucker-Prager model. The behaviour is assumed isotropic. The parameters of the ACMEG-T model were determined from calibration on laboratory tests. The Drucker-Prager model predicts a sharp transition between the elastic and plastic states, as seen on the orthoradial effective stress profile (Figure 7(c)). On the contrary, the results obtained with the ACMEG-T model exhibit a progressive mobilization of the plastic mechanisms, and it is no longer possible to distinguish a clear elastic zone because the entire domain is plastic (Figure 7(d)).

The numerical modelling reveals the drastic increase of the deviatoric stress in the inner part of the cylinder induced by the inner radial stress decrease. Dilatancy plastic strain is produced at the inner hole face, while the external part of the cylinder is subjected to slight plastic hardening characterized. This distinction is clear visible in the (p'-q) plane (Figure 8) where the point at the vicinity of the hole is subject to a strong decrease of mean effective stress while this mean stress increases at the outer face. The predicted convergence of the inner hole clearly depends on the model used. The Drucker-Prager model forecasts 2 mm of radial displacement while the ACMEG-T model predicts a quasi-closure of the inner hole (6.8 mm of convergence on the 7 mm of initial radius) (Figure 7(a) and Figure 7(b)). The convergence of the hole is split up into 1.6 mm of convergence during the first unloading and the rest during the second unloading. During the thermal phase, a small thermo-plastic hardening produces 2% of the volumetric plastic contraction strain in the first millimetres around the hole. However, this thermo-plastic process does not affect significantly the convergence of the hole because this hole is already almost closed before the heating phase.

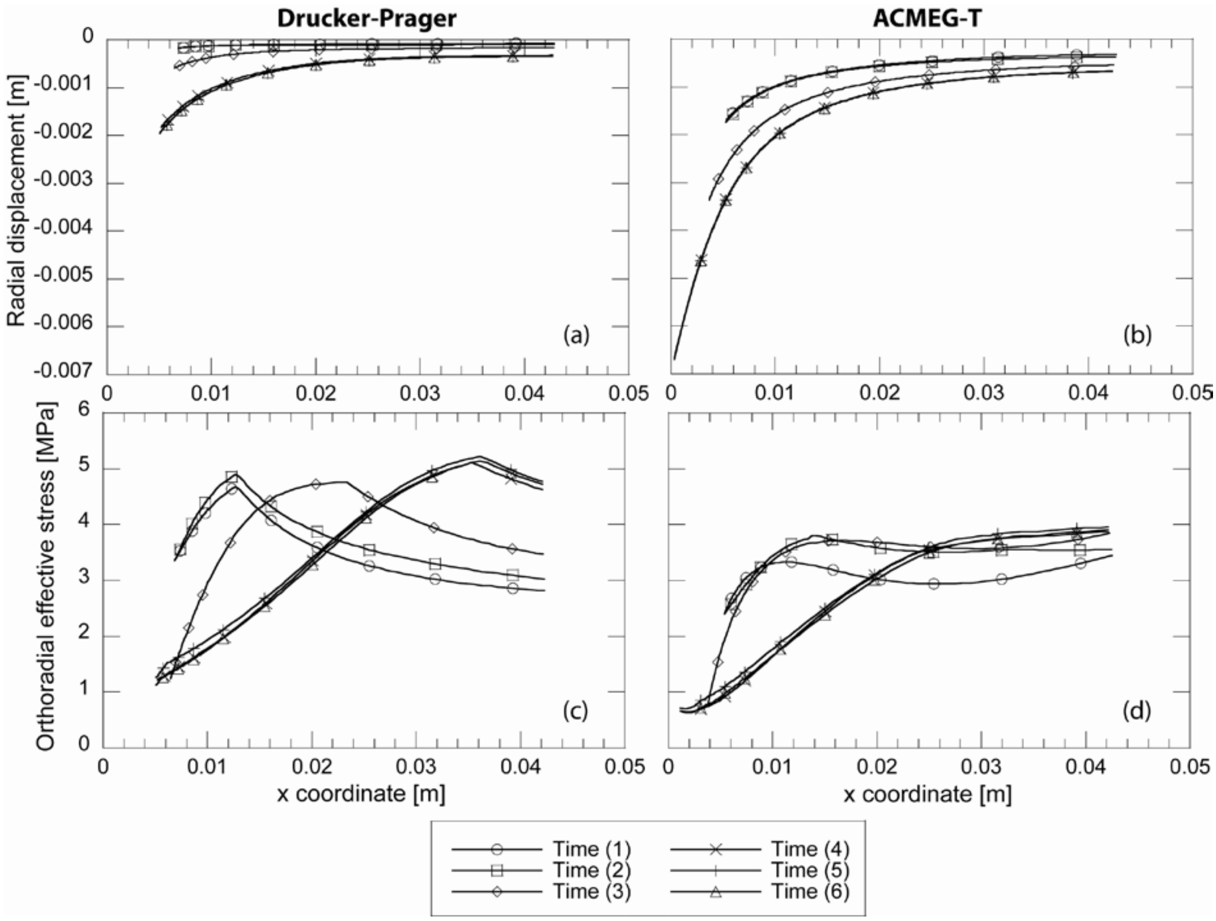

Figure 7: For different times, distribution in space of computed (a, b) radial displacement and orthoradial effective stress (c, d). Comparisons between predictions using the Drucker-Prager model (left) and ACMEG-T model (right). The selected times correspond to the end of the first mechanical unloading (1), the end of the first stabilization phase (2), the end of the second unloading phase (3), the end of the second stabilization phase (4), the middle of the thermal phase (5) and the final state (6)

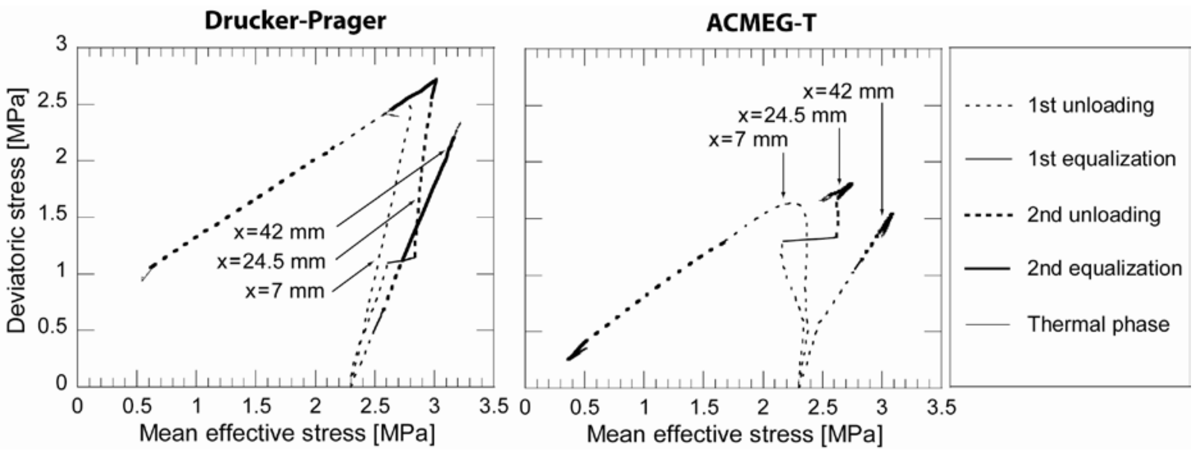

Figure 8: Stress paths in the (p'-q) plane at three different radial coordinates (7 mm, 24.5 mm and 42 mm). Comparisons between predictions using the Drucker-Prager model (left) and ACMEG-T model (right)

It is to note that the imposed mechanical unloading defined in the benchmark exercise was higher that the unloading that has been applied experimentally. It explains the higher convergence of the central hole obtained numerically.

CIMNE contributions

As Boom clay presents a bedding plane structure due to its sedimentary origin, some anisotropic features may be considered. In the elastic domain, the stress-strain relationship is described by an anisotropic linear elastic constitutive law. The elastic domain is limited by a Mohr-Coulomb type yield surface. Plastic deformations are non-associated (null volumetric plastic strain) and perfect plasticity is considered.

With the basic case, a qualitative agreement between measurements and simulation is observed (Figure 9): both shows a more important cavity wall displacement in the direction of the bedding plane, a displacement plateau (equivalent to 0 strain) in the farther field and a less displacement of the outer cylinder wall in the bedding plane direction.

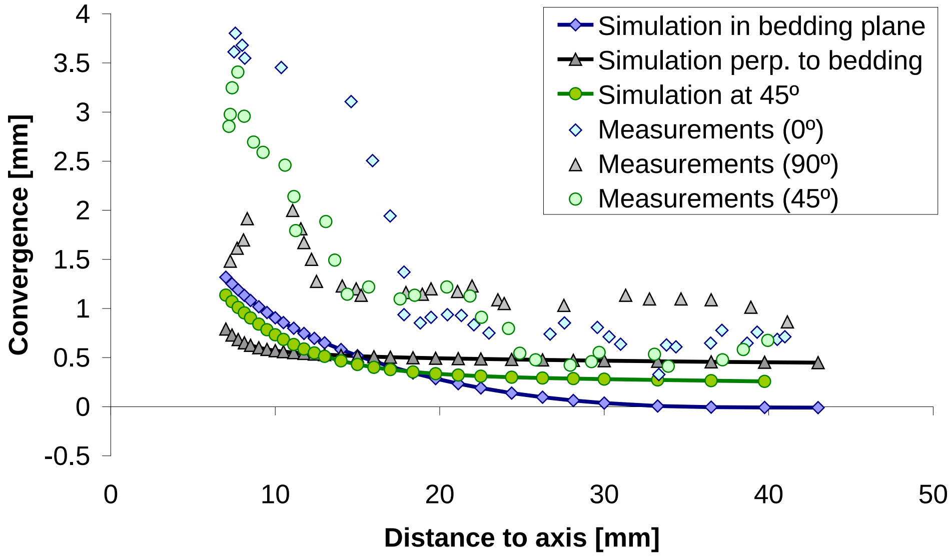

Figure 9: Comparison of measured and simulated displacement profiles in the three directions

Some changes were applied to the base case in order to increase the understanding of the system:

- Variant 1: only elastic case (no yield limit)
- Variant 2: associated flow rule (plastic volumetric strain is allowed)
- Variant 3: reduced friction angle, resulting in an increased intensity of the plastic mechanisms

The simulation results for variant 1 (elastic case) differs one order of magnitude from the measurements. This is an indication that most of the strain observed in the experiment is due to plastic mechanisms. Moreover, the simulated convergence (radial displacement of the inner wall) shows an inverse tendency as the displacements.
If volumetric plastic strains are allowed, the influence of the anisotropic part of the mechanical law (i.e. in the elastic region) is minimized and the sample behaviour seems to be most isotropic
Finally the friction angle was reduced to quite a low (and unrealistic) value of 10° in order to achieve a quantitative match of the measured displacement profiles (Figure 10).

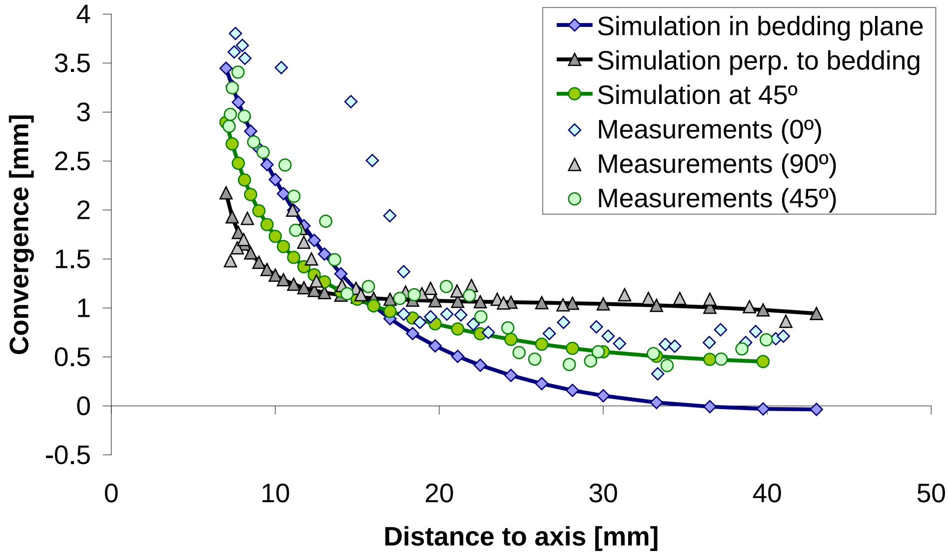

Figure 10: Comparison of measured and simulated displacement profiles in the three directions (reduced friction angle, 10º)

EURIDICE contributions

EURIDICE simulated the hollow cylinder test, applying the experimental boundary conditions with two distinct models: 2D plane strain model and 2D axisymmetric model.

2D plane strain model

Due to the symmetric nature and plane strain condition of the problem, a quarter of the cross section is selected for numerical modelling. The boundary conditions are in agreement with the experimental conditions. Three cases are simulated to investigate the effects of hydro-mechanical anisotropy on the radial displacement in the sample. In each case, the friction angle is limited to 10°.

Case 1 considers cross-anisotropic elasticity with the perfectly plastic Drucker-Prager. The modelling gives the consistent trend of the anisotropic radial displacements to that of measured displacements, and the magnitude of the displacements could be considered good.

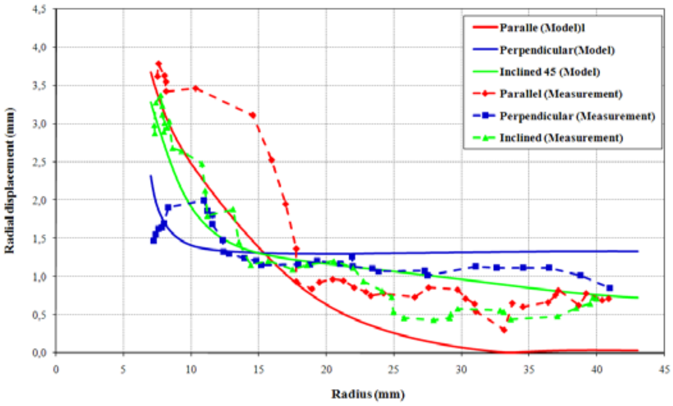

Figure 11: Radial displacement profile after mechanical unloading and water pressure dissipation in the direction parallel, perpendicular and at 45° to the bedding plane

Case 2 only investigates the hydraulic anisotropy with mechanical behaviour being isotropic. The modelled radial displacements give the reverse trend of the anisotropic radial displacements to that of Case 1, the displacement being larger in the direction perpendicular to bedding. It is not in agreement with experiment. Case 3 investigates both hydraulic anisotropy and mechanical anisotropy. The modelling also gives the reverse trend of the anisotropic radial displacements to that of Case 1.

As a conclusion, it seems that the mechanical anisotropy might contribute to the experimentally measured anisotropic convergence, while hydraulic anisotropy presents anisotropic convergence on the contrary.

2D axisymmetric model

2D axisymmetric model without considering the anisotropic hydro-mechanical behavior of the sample has been simulated. The bottom of the sample is assumed to be impermeable and vertically fixed. The top of the cap is subjected to the same history and magnitude of pressure as the radial pressure at the outer surface. To compare with the 2D axisymmetric model, 2D plane strain model has been simulated with isotropic hydro-mechanical conditions with a friction angle of 10° and a cohesion of 300 kPa. It reveals that the 2D axisymmetric model underestimates the measured axial displacement, but gives the similar trend of the displacement (Figure 12). So, based on the present modelling, it is indicated that hollow cylinder test is not exactly plane strain problem.

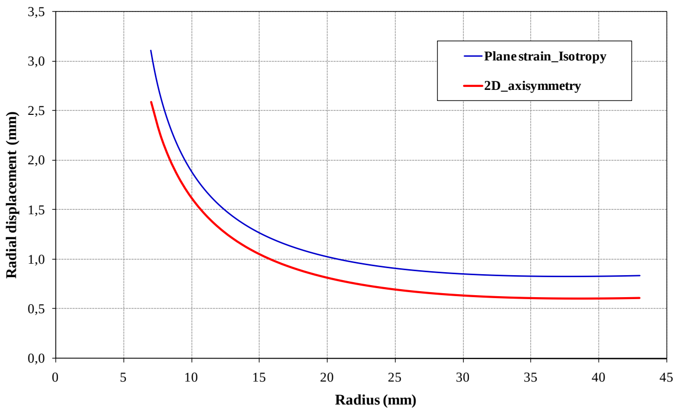

Figure 12: Comparison between the radial displacement profiles obtained with the 2D axisymmetric and the 2D plane strain problems

UJF contributions

2D plane strain problem have been simulated considering a quarter of the entire section. A strain cohesion softening Drucker-Prager model coupled with cross-anisotropic elasticity has been used. To describe the post-peak behaviour, where the localized zones appear, a second gradient model is added to the mechanical part. Doing so, the computation is not affected by mesh-dependency and the objectivity of the solution is reached. The cohesion varies between 300 kPa at the peak until 100 kPa at the residual state. Friction angle is maintained constant at a value of 18°. The hydro-mechanical loading path is in agreement with the experimental test. Only, the 70 minutes of the unloading phase has been modelled.

The focus has been made on how the localization phenomenon appears around the inner part of the sample. At the beginning of the unloading, the plastic deformation appears around the element at 45° with respect to the bedding plane (Figure 13). Then, the strain localization begins in the direction of bedding plane, accumulating plastic strains. As a consequence the displacements are bigger in the direction of bedding. Indeed, the plastic strain clearly tends to move in the direction of the most rigid plane (the bedding plane). At the beginning of the plasticity process, the maximum displacement is in the direction perpendicular to bedding that is characterized by the lower Young modulus. Due to the localization of plastic deformation, the horizontal becomes the direction where the displacements are more important.

The results gives a good qualitatively distribution of the displacement fields. However, the order of magnitude of the displacement between numerical and experimental results is not comparable (from 0.2 to 0.3 mm in stead of 2 to 4 mm).

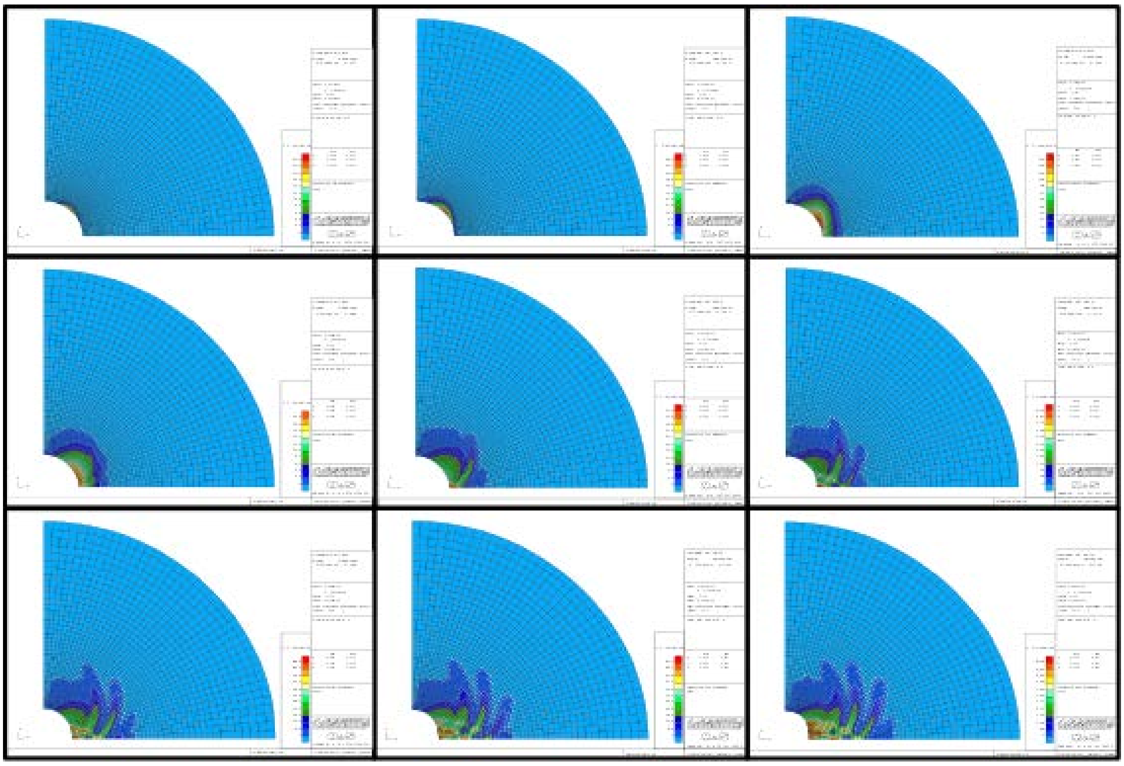

Figure 13: Equivalent plastic strains at different times: 2268 s - 2940 s – 3360 s - 3617 s – 3711 s - 3900 s - 4026 s- 4100 s - 4200 s

ULg contributions

<u>*Mohr Coulomb criterion*</u>

Using the same problem definition as for the benchmark exercise (1D axisymmetric conditions), a Mohr-Coulomb plastic criterion has been used instead of the Drucker-Prager yield limit. The results show an increase of radial displacement (from 2 mm with the Drucker-Prager model to 5.2 mm with the Mohr-Coulomb criterion) because the Mohr-Coulmb model allows a plastic behaviour at a lower stress than the Drücker-Prager criterion (for the same friction angle and cohesion) (Figure 14(a)). As a consequence, the maximum deviatoric stress that the material may sustain is reduced which is clearly visible in the stress path in ($I_{\sigma} - II_{\hat{\sigma}}$) plane (Figure 14(b)).

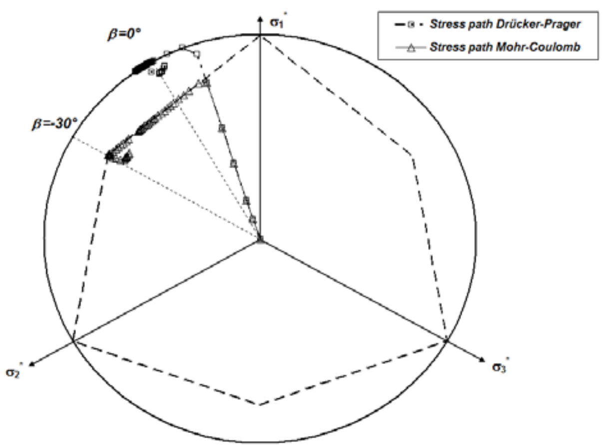

(a)

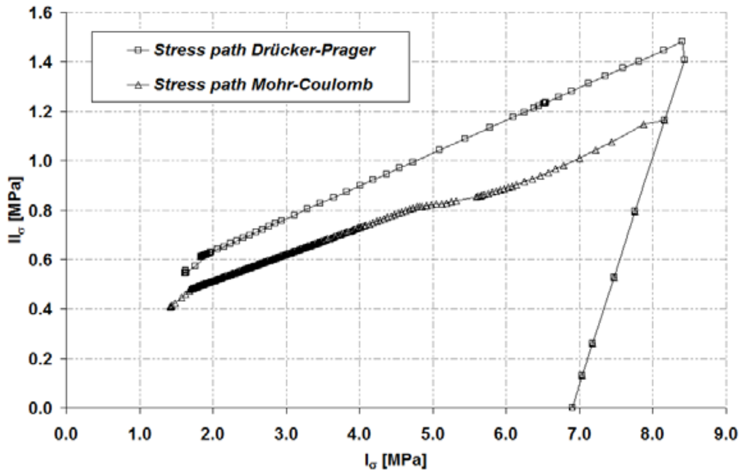

(b)

Figure 14: Representation of the stress path for the Drucker-Prager model and the Mohr-Coulomb model : (a) in the principal stress plane and (b) in the ($I_\sigma - II_{\hat{\sigma}}$) plane

During the thermal heating-cooling cycle, no clear difference can be observed between both models predictions because in both case, the thermo-mechanical response is governed by the same thermo-elastic processes.

2D plane strain case

In order to catch the anisotropic response of the material and the possible strain localisation, 2D plane strain modelling has been performed. The objective of this simulation is to reproduce the behaviour of the material in the mid-plane section of the hollow cylinder, assuming plane strain conditions. Because of the symmetry of the problem, a quarter of the entire section is considered. To reproduce as well as possible the experimental results, the boundary conditions that have been applied experimentally have been considered. The total stress and the pore water pressure at the external boundary are kept constant at 4.5 MPa and 2.2 MPa, respectively. At the inner face, a decrease of total stress from 4.5 MPa to 1.0 MPa is considered, while the pore water pressure is reduced from 2.2 to 0.6 MPa. This mechanical unloading is applied in 70 minutes and then an 11h20min period is imposed to reach a hydro-mechanical steady-state. No thermal phase is considered.

In order to reproduce the anisotropic response of the materials, a Drucker-Prager hardening model (similarly to the benchmark exercise) has been coupled with cross-anisotropic elasticity as well as a dependency of the cohesion with respect to the angle between the major principal stress direction and the normal to bedding plane.

A parametric study has been performed in order to determine the most suitable set of parameters able to reproduce the intensity of radial displacement as a function of the radial direction with respect to the bedding orientation. Five cases have been considered: cross-anisotropic elasticity (no plasticity, case 1), cross-anisotropic elasticity and perfectly plastic Drucker-Prager model (case 2), cross-anisotropic elasticity and hardening/softening Drucker-Prager model (case 3), cross-anisotropic elasticity and perfectly plastic Drucker-Prager model with reduced friction angle of 10° (case 4), cross-anisotropic elasticity and hardening/softening Drucker-Prager model with anisotropic cohesion (case 5). The material parameters are summarized in Table 3.

Geomechanical characteristics		Case 1	Case 2	Case 3	Case 4	Case 5
Young elastic modulus [MPa]	$E_{//}$	500	500	500	500	500
Young elastic modulus [MPa]	$E_{\perp}$	250	250	250	250	250
Poisson ratio [-]	$\upsilon_{////}$	0.125	0.125	0.125	0.125	0.125
Poisson ratio [-]	$\upsilon_{//\perp}$	0.125	0.125	0.125	0.125	0.125
Initial cohesion [kPa]	c_0	-	300	300	300	270 (0°) 255 (45°) 525 (90°)
Final cohesion [kPa]	c_f	-	300	100	300	90 (0°) 85 (45°) 175 (90°)
Softening parameter [-]	β_c	-	-	0.01	-	0.01
Initial friction angle [°]	ϕ_{c0}	-	18	5	10	5
Final friction angle [°]	ϕ_{cf}	-	18	18	10	18
Hardening parameter [-]	β_ϕ	-	-	0.01	-	0.01
Dilatation angle [°]	ψ	-	0	0	0	0

Table 3: Geomechanical characteristics used in the 2D plane strain problem

The purely elastic case (Case 1) emphasises the anisotropic behaviour of the material with the larger displacements being obtained in the more compressible direction (perpendicular to bedding). However, this case largely underestimates the obtained displacement (around 0.1 mm) with respect to experimental results (2 to 4 mm). In case B, the directional dependency of the radial displacement is obtained but the displacements remains much lower than the experimental results (0.3 mm instead of 2 to 4 mm).

In case C, the cohesion softening allows us to model the post peak response of the Boom Clay. The magnitude of displacements obtained in the simulations is now more in agreement with the experimental displacements. However, the effect of the direction on the central hole displacements is not large enough with respect to the experimental observations (Figure 15 (a)). In case D, a perfectly plastic Drucker-Prager model is kept and the friction angle is reduced from 18° to 10°. In that case, the anisotropic radial displacements of the central hole are much better reproduced but the displacements of the outer region perpendicularly to bedding are negative which correspond to extension of that external zone. This aspect is not in agreement with experiment (Figure 15 (b)). Finally, an anisotropic plastic criterion coupled with a hardening/softening Drucker-Prager model, assuming that the material cohesion depends on the angle between major principal stress and the normal to the bedding plane, allows us to get the best agreement with respect to the experimental measurements (Figure 15 (c)).

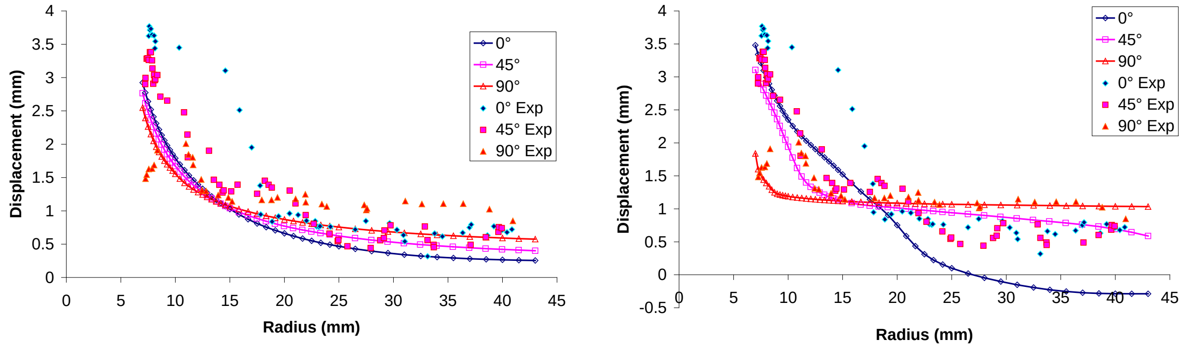

(a) (b)

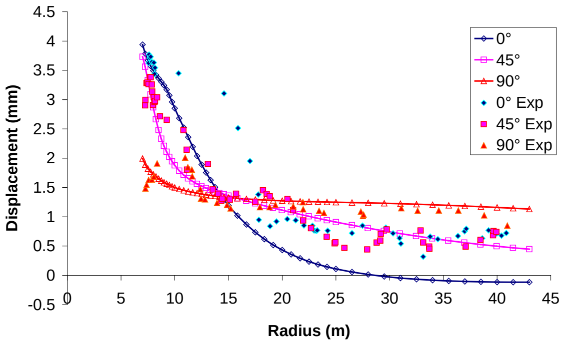

(c)

Figure 15: Radial displacement profile after mechanical unloading and water pressure dissipation in the direction parallel, perpendicular and at 45° to the bedding plane. Comparison with experimental measurements for case 3 (a), case 4 (b) and case 5 (c)

Also, the aspects of strain localization have been considered, using the local second gradient model in order to properly model the post-peak behaviour by introducing an internal length scale. The strain localization has been studied for the case 3. After the excavation, almost all the section is plastic but it is clear that some shear bands pattern appears. Between these bands, the behaviour is elastic and the contour of the increment deviatoric strain highlights the activity of the bands in terms of shear strains. At t = 5000 s and t = 6000 s, the process of shear banding shows that some bands occur and then become less active. The competition between these different bands is clearly observed. At t = 10000 s, the localization pattern becomes more stable and the final structure of the most active shear bands is only composed of three bands.

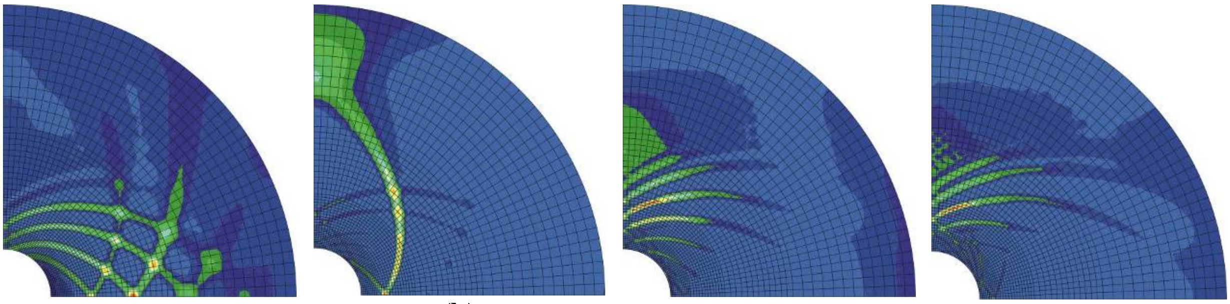

(a) (b) (c) (d)

Figure 16: Contour of normalized increment of deviatoric strain at t = 4200 s (a), t = 5000 s (b), t = 6000 s (c), t = 10000 s (d)

2D axisymmetric case

The previous simulations assume plane strain state while the experimental conditions are stress-controlled in the axial direction and the radial displacements are constrained at the top and at the bottom of the hollow cylinder. In order to study the effects of axial boundary conditions on the behaviour of the mid-plane section, 2D axisymmetric modelling have been performed with two models: the perfectly plastic Drucker-Prager model and the hardening/softening Drucker-Prager model. The comparisons between the radial displacements obtained in the mid-plane section with the 2D plane strain and 2D axisymmetric conditions shows almost identical results (Figure 17). It proves that the effect of axial boundary conditions on the behaviour of the mid-section may be considered as negligible.

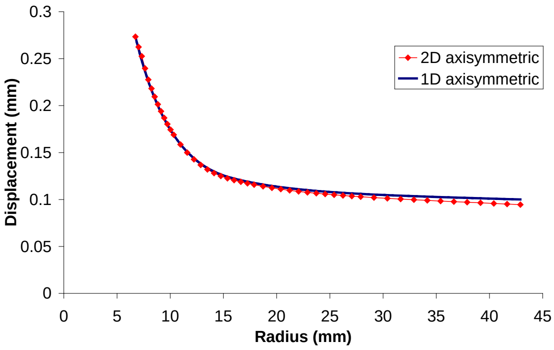

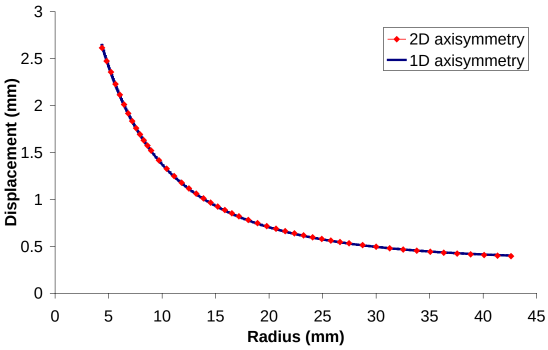

Figure 17: Comparison of the radial displacement profile after mechanical unloading and water pressure dissipation with the 2D plane strain and the 2D axisymmetric conditions: (a) the perfectly plastic Drucker-Prager model, (b) the hardening/softening Drucker-Prager model

2.2 Conclusions

The numerical modelling of the hollow cylinder experiment on Boom Clay has been carried out in two successive steps. First, a benchmark exercise has been defined before obtaining the experimental results. The results of this exercise were used to validate the numerical tools used by the different teams (ULg, EPFL, EURIDICE, CIMNE, UJF). Then, after obtaining the first experimental results, a second series of numerical simulations have been performed to reproduce the experimental evidences.

During the benchmark exercise, agreement between the predicted results of the different teams has been obtained. Also, first interpretations of predicted results have been made in term of principal stress evolution, followed stress path, pore water pressure and displacement profiles. Those simulations consisted in blind predictions.

Then, in the second phase of simulations, the liberty was given to each team to focus on any specific features of behaviour related to the experimental evidences. The following aspects have been mainly addressed: (i) the anisotropic response of Boom Clay, (ii) the strain localisation process, (iii) the strain softening behaviour and (iv) the effect of the axial boundary conditions on the global response of the hollow cylinder.

To reproduce the magnitude of displacements measured in the hollow cylinder experiment, it has been noticed that the plastic strength must be drastically reduced with respect to the usual values of 18° for the friction angle and 300 kPa for the cohesion of Boom Clay. Three alternatives have been used: (i) a reduced friction angle of 10°, (ii) a strain cohesion softening from 300 kPa (at peak) to 100 kPa (at the residual state) or (iii) a Cam-Clay type model that allow softening in the wet part of the yield limit. The strain cohesion softening model induces strain localization that has been model with a second gradient model including an internal length scale.

We have no clear experimental evidences on the possible development of shear bands in the hollow cylinder, probably because the X-Ray Tomography scan has been performed after reaching a steady state. At that time, the sum of each localized phenomenon produces quite a diffuse pattern of the shear strain distribution that could avoid any clear observation of localized phenomenon at that moment of observation. However, the irregularity in the measured displacement profile could be an indication of possible localized phenomena.

An other important aspect on the mechanical behaviour of Boom Clay that as been observed during the hollow cylinder experiment is the cross-anisotropic response. From a constitutive point of view, it has been addressed with cross-anisotropic elasticity and also a possible dependence of the cohesion with respect to the direction of bedding.

As a conclusion, through numerical modelling of the hollow cylinder experiment, we have shown that the developed numerical models are able to reproduce the main processes that occur in Boom Clay during the hydro-mechanical hollow cylinder tests.

2.3 COX

Hollow cylinder tests have been performed by GRS on COX argillite samples within Timodaz WP 3.3 (Deliverable 7). The experimental results have evidenced the axial permeability increases by fracturing due to the mechanical and thermal loadings. Within Timodaz WP5.3 ULg and GRS perform thermo-hydro-mechanical modelling of this experiment. New hydro-mechanical couplings are proposed in order to reproduce the increase of the permeability with the mechanical load:

- ULg uses a hydro-mechanical model where an additional coupling between the permeability and the tensile strains is associated. This embedded fracture model allows the reproduction of the development of preferential pathways along fractures generated by tensile strains. This model is introduced in the finite element code Lagamine developed by ULg.
- GRS uses a damage-elastoplastic model, which takes into account the permeability evolution with porosity according to the Kozeny relationship. The modelling from GRS is performed with the Code_Bright finite element code.

2.3.1 Large hollow cylinder tests on COX argillite

Within TIMODAZ-WP3.3 (Deliverable 7), GRS carried out EDZ-simulation tests on four large hollow cylinders of the COX argillite to investigate fracturing and sealing processes of the host rock around HLW disposal boreholes. The large COX cores were extracted from the MHM-URL at Bure and prepared to hollow cylinders of ~0.5 m length and 280 mm outer diameter with axially-drilled central boreholes of 100 mm diameter. High saturation degrees were achieved between 82 % and 100 %.

Regarding damage development and recovery in the host clay rock around HLW disposal boreholes, the tests were designed and carried out in the GRS big triaxial apparatus by simulation of the relevant processes such as borehole excavation, backfilling / lining, heating, and cooling. Figure 18 illustrates a typical test layout and the pictures of a large hollow cylinder before and after testing.

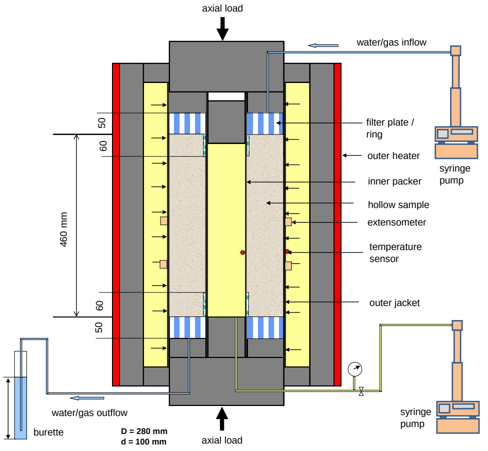

Figure 18 : Test layout of EDZ-simulation with large hollow cylinders of COX argillite

The main observations from the four large hollow cylinder tests are:

1. The borehole excavation simulated by reducing the inner borehole pressure from 15 MPa down to 1 MPa resulted in convergence of the borehole but not any increase in permeability along the cylinder axis, indicating no build up of pathway through the samples. Further increase of the external confining stress beyond 20 to 24 MPa (corresponding to depths of 800 – 1000 m) led to fracturing and flow pathway, indicated by the drastic increase in gas permeability from 10^{-21} m^2 to 10^{-14} m^2.
2. The backfill impact simulated by increasing the inner borehole pressure from 1 to 15 MPa led to a strong reduction of the gas permeability by several orders of magnitude from 10^{-17} down 10^{-21} m^2, depending on the initial characteristics of the excavation-induced fractures in the argillite.
3. The water transport through the fractures in the claystone led clay minerals swelling into the interstices and thus sealing the fractures, whereby the permeability decreased drastically to $2 \cdot 10^{-18}$ m^2, four orders of magnitude lower than that by gas flowing.
4. Heating from 29 °C to 74 °C accelerated the borehole convergence and the water inflow. The thermal impact on the water conductivity of fractured claystone is governed by the change of the water viscosity, while the intrinsic permeability is less affected by heating.
5. Cooling down slowed the deformation and the water transport through the fractured claystone. The permeability after cooling was between $1.0 \cdot 10^{-18}$ and $3.5 \cdot 10^{-18}$ m^2, nearly the same as that before heating.
6. The post-investigation on a tested sample showed a significant increase of the water content up to 9.3 % at the inlet side to 6.2 % at the outlet. The most part of the sample was “over saturated”, i.e. the water content was higher than that in the natural and saturated state (w ≈ 7.0 %). The water uptake was accompanied by volume expansion of the clay matrix into the fracture space under confined conditions.

Details of the test results are given in Deliverable 7.

2.3.2 Numerical results of ULg

ULg numerical modelling of hollow cylinder tests is performed by using Lagamine finite element code. One EDZ-simulation test is modelled: the BMT4 hollow cylinder test. Initial state of argillite is desaturated ($S_{rw} \approx 0.86$), which implies the need of a thermo-hydro-mechanical model for unsaturated media. The initial stress state is isotropic.

2.3.2.1 Constitutive models

The main relationships of the thermo-hydro-mechanical model for unsaturated media are based on Bishop effective stress. The mechanical model used for the COX argillite is a non-associated elastoplastic constitutive law. The yield surface is defined by a Van Eekelen criterion. Isotropic hardening of the friction angle is considered in the model.

The mass flow into the porous medium is defined by the sum of the advection of the liquid water (Darcy’s law for unsaturated cases) and the diffusion of water vapour (Fick’s diffusion law). The advective flux of the gaseous phase is neglected. The water retention curve is given by the van

Genuchten relationship and the water relative permeability function proposed by van Genuchten is also adopted.

The heat transport is related to three effects: conduction, convection by the fluids and evaporation. The enthalpy of the system is given by the sum of each component's enthalpy. Further details about the balance equations and the coupled thermo-hydraulic formulation can be found in Collin et al. (2002) and in Deliverable 10.

2.3.2.2 Permeability-strain coupling model

A specific permeability model (Olivella and Alonso, 2008; Levasseur et al., 2010) is considered in order to reproduce the development of preferential pathways into argillite. It adds new hydro-mechanical coupling between permeability and the strain state. The basic idea consists in the appropriate representation of single discontinuity representing the rock bedding, which is embedded in a continuous finite element. As presented in Deliverable 10, the increase of permeability in the damage zone is linked with the development of tensile strains:

$$K_{ij} = K_0\left(1+\lambda\left(\varepsilon^T-\varepsilon_0\right)\right)^3 \text{ if } \varepsilon^T > \varepsilon_0 \tag{0.5}$$

with K_0 the initial permeability, ε^T the tensile strain, ε_0 a threshold strain for the permeability increases and λ a fitting parameter corresponding to the fracture density. The threshold strain could be considered as the strain corresponding to the tensile strength of the rock. Aperture opening cannot therefore be initiated before a failure by tension occurs.

2.3.2.3 Experiment numerical idealization

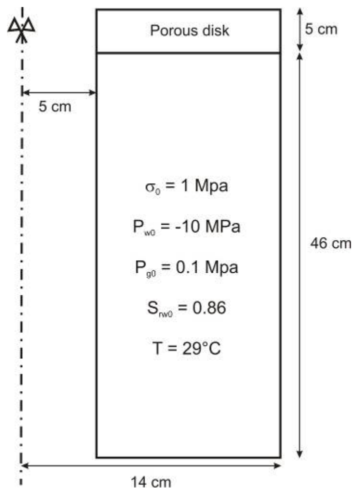

(a)

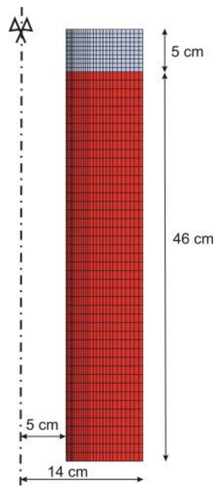

(b)

Figure 19 : BMT4 hollow cylinder test (a) Geometry and initial conditions – (b) Mesh for finite element modelling

A 2D axisymetric modelling of the BMT4 hollow cylinder test is performed. Injection filter is taken into account in the modelling (Porous disk), because it influences the water volume injected during the four injection steps. Indeed when the injection system is shut-off the water in the porous disk continues flowing into the sample. The porous volume of the injection system influences thus the water volume injected in the sample. The geometry and the initial conditions of the modelling are presented in Figure 19.

There are 6 steps in the thermo-hydro-mechanical modelling of the BMT4 hollow cylinder test: the consolidation, the borehole excavation, the EDZ intensification, the water injection tests, the cooling and the heating stages. Gas permeability tests are performed at the end of the consolidation stage and during the borehole excavation and EDZ intensification stages. However they are not modelled, which should not influence a lot the numerical results owing to the low gas volume injected in argillite. Gas pressure remains thus constant at the atmospheric pressure during the modelling.

Concerning the filter, high permeability is defined and the water relative permeability curve is based on a cubic law. A small air entry value and a sharp decrease are used for the retention curve of the filters. A linear elastic model is used for the mechanical behaviour with the same Young modulus and Poisson ration as for argillite. It allows avoiding the development of stresses concentration and traction strains at the contact between the filter and argillite. The porosity of the filters is provided by GRS and is needed in order to reproduce the correct porous volume of the injection system. The thermal characteristics are the same as for argillite.

2.3.2.4 Conclusion on ULg modelling

An elastoplastic model with a hardening of the friction angle provides a good reproduction of the experimental strains measured at the sample inner and outer during the different mechanical loading steps.

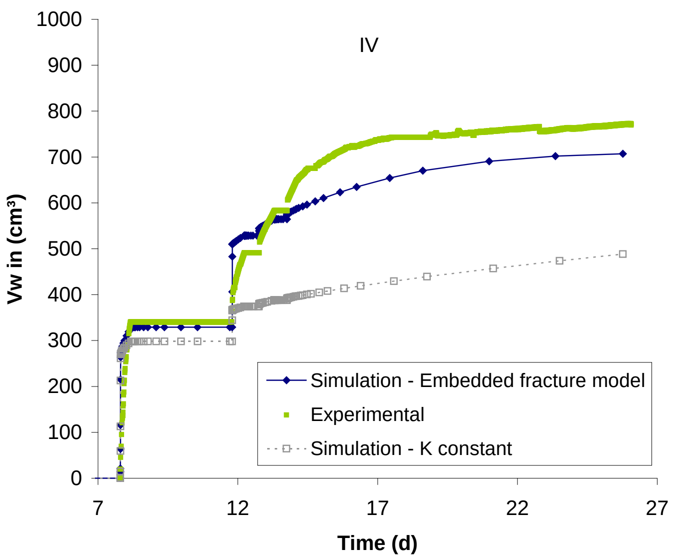

Figure 20 : Water volume injected during the injection tests – Comparison between experimental and numerical results

The embedded fracture model has been used for the modelling of the different steps. It allows the increase of the permeability assuming the development of preferential pathways in the zones where tensile strains are developed (Figure 20). Aperture of discrete paths is the main variable that controls the permeability evolution. This model allows the reproduction of the permeability increase observed at the inner of the COX hollow cylinders submitted to mechanical load. Nevertheless the experimental results seem to be strongly influenced by the initial desaturation of the porous disk, which makes difficult an accurate reproduction of the injected water volume through the sample during the water hydraulic tests.

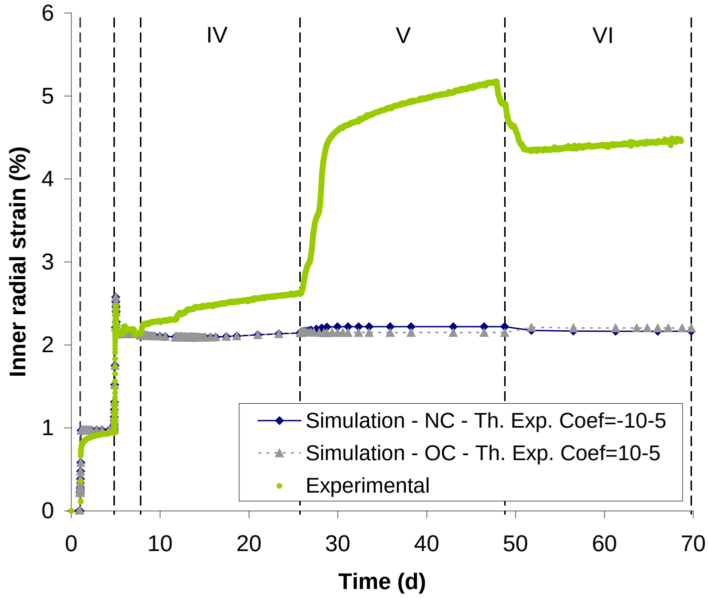

Figure 21 : Inner radial strain during heating and cooling stages (V and VI) – Comparison between experimental and numerical results

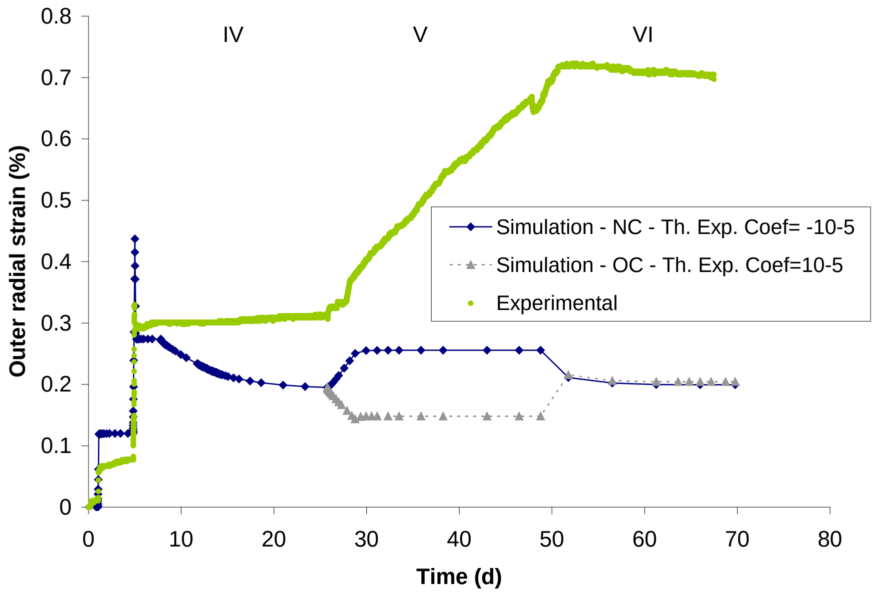

Figure 22 : Outer radial strain during heating and cooling stages (V and VI) – Comparison between experimental and numerical results

During the heating and the cooling stages, the modelling could reproduce the general tendency of the water inflows or outflows (Figure 21 and Figure 22), but underestimate the experimental water volume. The thermo-mechanical model of the COX hollow cylinder does not take into account the influence of temperature on the mechanical characteristics, but argillite seems to behave as a normally consolidated rock with the development of compressive strains when the temperature increases. For long term predictions, the modelling underestimates the experimental radial strains, but the development of potential thermo-plasticity is not taken into account in the model.

2.3.3 Numerical results of GRS

GRS benchmark modelling was performed by using CODE_BRIGHT (version cdv3, 2004). Two EDZ simulation tests BMT1 and BMT4 were modelled.

2.3.3.1 Constitutive models

Considering the complex testing procedure and boundary conditions of the large hollow cylinder tests, coupled THM calculations were carried out by solving a set of balance equations of energy, solid mass, water mass, air mass and stress equilibrium with selected constitutive models. The main assumptions were made:

1. The COX clay rock is relatively isotropic and homogeneous because of the insignificant bedding planes;
2. Heat transport includes conduction (Fourier's law) through the porous medium, advection of liquid water and vapour flow;
3. Water transport is controlled by liquid water advection (Darcy's law), vapour diffusion in air (Fick's law), and liquid / gas phase changes (psychrometric law);
4. Gas migration is governed by advection (Darcy's law), dissolution in liquid (Henry's law) and the ideal gas law;
5. The damage-elastoplastic model developed by CIMNE for argillaceous rocks (Vaunat et al., 2003; 2004; 2009) is applied for description of the mechanical behaviour of the COX claystone. COX is considered as a composite material made of a clay matrix connected by bonds (Figure 23). The clay matrix behaves like a typical elastoplastic soil Hoek and Brown's criterion as yield surface, while the bonds behave like a typical quasi-brittle material that can be represented by a damage elastic law. Bond damage or degradation occurs as the result of apparition of micro-fissures within the bonds, which reduces the surface on which stresses and strains are active. Any load applied to an element of cemented material is distributed itself between the soil matrix and the bonds according to a ratio that depends on the geometric arrangement of both components.

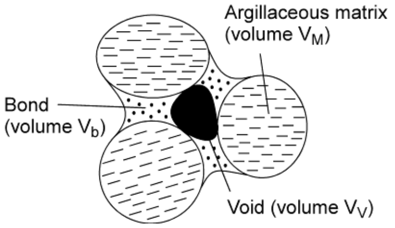

Figure 23 : Conceptual model of claystone as composite material with clay matrix and bonds

Details of the formulations and applications of the applied balance equations and constitutive models are given in a number of CIMNE's publications (Gens et al., 2006; 2007; Vaunat et al., 2003; 2004; 2009).

2.3.3.2 Permeability porosity coupling model

The Kozeny's model is employed for the relationship of permeability k with porosity φ:

$$k = k_o \frac{\varphi^3}{(1-\varphi)^2} \frac{(1-\varphi_0)^2}{\varphi_0^3} \tag{0.6}$$

with the initial permeability value of $k_0 = 2 \cdot 10^{-20}$ m^2 at the initial porosity of φ_o = 15% for the COX argillite.

2.3.3.3 Experiment numerical idealizations

<u>BMT1</u>

The EDZ-simulation test BMT1 was performed on a COX hollow cylinder (DIR2003-K4) of D/d/L= 280/100/525 mm at ambient temperature of 26 °C in four steps:

i. <u>Initial state</u> at the same outer and inner borehole pressure of $\sigma_R = \sigma_r$ = 15 MPa and axial stress of σ_a = 17 MPa;

ii. <u>Borehole excavation</u> by decreasing the inner pressure down to σ_r = 2.6 MPa;

iii. <u>Unloading</u> in radial direction down to σ_R = 3 MPa for 4 days;

iv. <u>Loading</u> in axial direction to failure.

During the test, gas flow was recorded at injection pressure of 1.5 MPa at the bottom. This test was simulated in a hydro-mechanical coupling way using an axisymmetric model. Because the sample was initially not saturated at a degree of 82 %, the corresponding suction of s = 22 MPa is adapted as the initial condition in the sample. The modelling steps with application of the corresponding boundary conditions are illustrated in Figure 24.

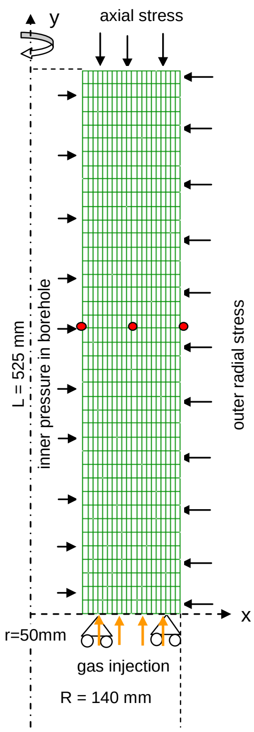

Calculation procedure:

<u>Step 1</u>: t = 0 – 0.9 day, pre-consolidation

temperature T = 26 °C

pore water pressure p_l = -22 MPa

gas injection pressure p_g = 1.5 MPa

vertical stress σ_y = 17 MPa

outer radial stress σ_R = 15 MPa

inner radial stress σ_r = 15 MPa

<u>Step 2</u>: t = 0.9 – 1.8 day, borehole excavation

inner radial stress from σ_r = 15 to 2 MPa

<u>Step 3</u>: t = 1.8 – 5.9 day, radial unloading

outer radial stress from σ_R = 15 to 3 MPa

<u>Step 4</u>: t = 5.9 – 6.0 day, axial loading

axial stress from σ_y = 17 MPa up to failure

Figure 24 : Geometry and boundary conditions for modelling of the hollow cylinder test BMT1

BMT4

The EDZ-simulation test BMT4 was performed on a COX hollow cylinder (DIR1004-EST27312) of D/d/L= 280/100/460 mm. The test procedure involved six phases with respective boundary conditions:

I. Initial state at the same outer and inner borehole pressure of $\sigma_R = \sigma_r = 15$ MPa and at fixed axial strain ($\Delta\varepsilon_a = 0$);

II. Borehole excavation by reducing the borehole pressure down to $\sigma_r = 1.0$ MPa;

III. EDZ-intensification by increasing the external radial load till gas breaking through;

IV. Water injection to the top of the fractured sample at pressures of 0.5 to 0.3 MPa for 17 days;

V. Heating by increasing the temperature from 29 °C to 74 °C at the outer surface during 3 days and kept constant for 19 days;

VI. Cooling down by reducing the temperature to the initial level of 29 °C over 3 days and kept for 18 days.

Considering the complex testing procedure and conditions, coupled THM calculations were carried out. The initial porosity of 15.8 % and saturation degree of 90 % (suction s = 10 MPa) are taken into account. An axisymmetric model is adopted for the hollow cylinder (Figure 25). The realized test procedure with the above mentioned steps is simulated by applying the corresponding conditions to the model.

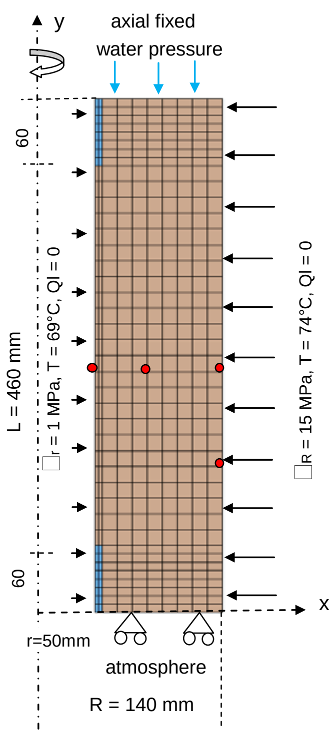

Calculation procedure:

Step 1: pre-consolidation, t = 0 – 1 day,
$T = 29°C$, $p_l = -10$ MPa, $p_g = 0.1$ MPa
$\sigma_y = 1.7$ MPa, $\sigma_R = \sigma_r = 15$ MPa

Step 2: borehole excavation, t = 1 – 4.85 day
$\sigma_r = 15 \rightarrow 1$ MPa

Step 3: fracturing, t = 4.85 – 5.0 day
$\sigma_R = 15 \rightarrow 17$ MPa ($\sigma_{R\text{-}max}$ limited before failure)

Step 4: unloading, t = 5.0 – 7.9 day
$\sigma_R = 17 \rightarrow 15$ MPa

Step 5: water injection, t = 7.9 – 26 day
$p_{in} = 0.5$–0.3 MPa or $Q_{in} = 0$, $p_{out} = 0.1$ MPa
at $T = 29°C$, $\sigma_R = 15$ MPa, $\sigma_r = 1$ MPa, $\Delta\varepsilon_y = 0$

Step 6: ramp heating, t = 26 – 28 day
$T = 29°C \rightarrow T_{out} = 74°C$, $T_{in} = 69°C$
at $p_{in} = 0.3$ MPa, $p_{out} = 0.1$ MPa

Step 7: heating conitues, t = 28 – 48 day
$T_{out} = 74°C$, $T_{in} = 69°C$, $p_{in} = 0.3$ MPa or $Q_{in} = 0$

Step 8: ramp cooling, t = 48 – 50 day
$T_{out} = 74°C$, $T_{in} = 69°C \rightarrow T = 29°C$

Step 9: cooling down, t = 50 – 69 day
$T = 29°C$, $p_{in} = 0.3$ MPa or $Q_{in} = 0$

Figure 25 : Geometry and boundary conditions for modelling of the hollow cylinder test BMT4

The following boundary conditions are applied: (1) instead of the fixed axial strain, the recorded axial stress of 1.7 MPa is applied in the model within the first three steps (I-III) because the poor control of the axial strain and possible weak contacts between the load pistons and the end faces of the sample; (2) the gas migration test during the first three steps (I-III) is not simulated by keeping the gas pressure atmosphere; (3) the temperature measured at the inner borehole wall is applied as a boundary condition because some amounts of heat lost from the sample ends; and (4) various values of the intrinsic permeability between $4 \cdot 10^{-20}$ and $5 \cdot 10^{-18}$ m^2 are examined by comparing the water flow and pressure with the measured data.

2.3.3.4 Conclusion on GRS modelling

In the GRS benchmark modelling, the capabilities of the THM constitutive models in CODE_BRIGHT (cdv3), particularly the damage-elastoplastic model for argillaceous rocks, have been examined by comparison with the results of the large hollow cylinder tests on the COX claystone in regard to the development and recovery of the EDZ around HLW disposal boreholes. The results indicate that:

- The short-term deformation behaviour of the hollow cylinders is reasonably represented by the model with indication of micro-damage evolution, but the post-failure behaviour could not be modelled due to earlier stop of the computation.
- The drastic increase in permeability by fracturing and the permeability decrease by re-compaction of the fractures cannot be captured by the Kozeny's permeability – porosity relationship for porous media without fractures (Figure 26).
- The observed water inflow into the fractured claystone is significantly underestimated by the modelling even though the real permeability value of the fractured claystone is used.
- The significant responses of deformation in the damaged claystone to heating and cooling are weakly revealed by the modelling (Figure 27).

Generally speaking, the THM behaviour of damaged claystones can not reasonably be approached by the constitutive models for continuum porous media without involving effects of discontinuities. From our knowledge, the behaviour of damaged claystones is not yet well characterized and understood. Further research work is obviously necessary to improve the constitutive models for the prediction of the development and recovery of the EDZ and to enhance the certainty of the long-term performance and safety assessments of HLW repositories in argillaceous formations.

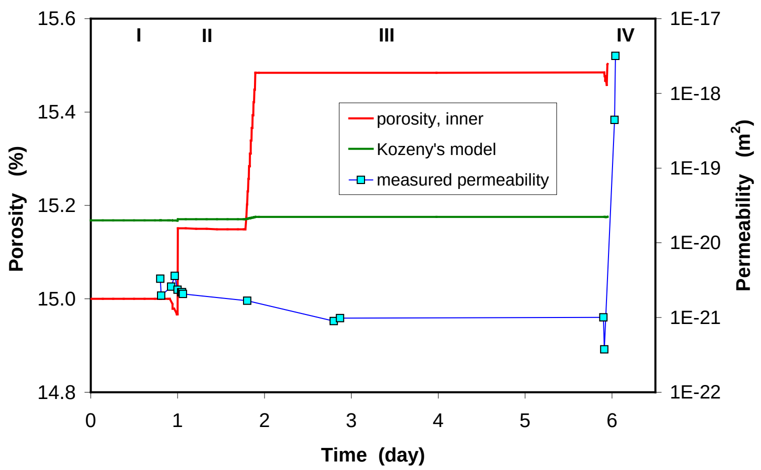

Figure 26 : Calculated permeability variations in comparison with the measured data

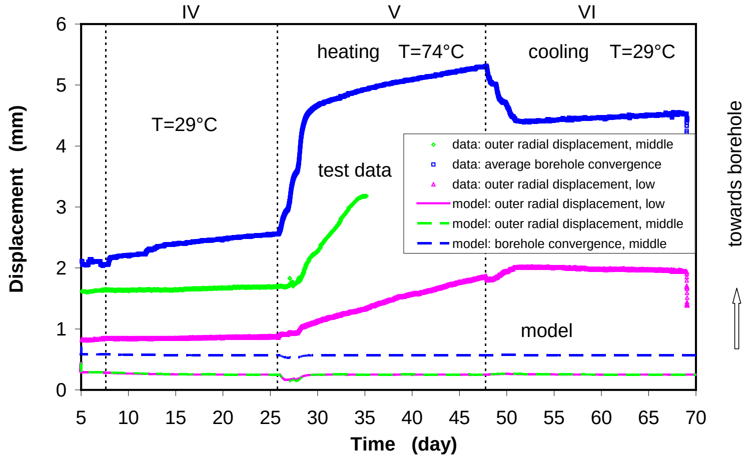

Figure 27 : Calculated and observed deformations before, during and after heating

2.3.4 Conclusions

Numerical results obtained by ULg and GRS show that the embedded fracture model (permeability-strain coupling model) allows the reproduction of the permeability increase of the damaged sample, whilst the Kozeny relationship is not sufficient to reproduce the drastic increase of the permeability. Nevertheless the experimental results seems to be strongly influenced by the initial desaturation of the porous disk, which modifies the injected water volume during the water injection tests and complicates an accurate reproduction of the numerical results.

2.4 Opalinus clay

Hollow cylinder tests have been performed at LMR-EPFL on Opalinus clay samples within Timodaz WP 3.3 (Deliverable 7). The first tests on a sample cored parallel to the bedding planes revealed the development of a fracture pattern around the central hole after the mechanical unloading and cracks sub-parallel to the bedding plane. The experimental results have evidenced the radial permeability increase by fracturing due to the mechanical and thermal loading.
Within Timodaz WP5.3 Itasca performs thermo-hydro-mechanical modelling of this experiment. A new thermo-hydro-mechanical coupling is proposed in order to reproduce the increase of the permeability with the mechanical and thermal loads. Itasca uses a permeability-porosity coupling model where permeability evolution is based on micro crack formation and local displacement increment. This model reproduces the increase of permeability parallel to fractures. The simulations involve a discrete numerical code (*PFC2D*) coupled with a continuum code (*FLAC3D*). A pure hydraulic computation is performed using *FLAC3D* (three-dimension Finite Difference Method) while the thermal-mechanical response is calculated using *PFC2D* (two-dimension Discrete Element Method).

2.4.1 Hollow cylinder tests on Opalinus clay

Within TIMODAZ-WP3.3 (Deliverable 7), EPFL carried out EDZ-simulation tests on four hollow cylinders of Opalinus clay to investigate fracturing and sealing processes of the host rock around HLW disposal boreholes.

Laboratory tests are performed at the LMR-EPFL on thick-walled hollow cylindrical samples prepared by drilling a coaxial central hole in a drill core (14 and 86 mm in diameter respectively). The tests aim at modelling at small-scale mechanical and thermal loads fairly similar to those that will be experienced by the host rock around disposal galleries for heat emitting radioactive waste. After recovery of the in situ stress conditions, the pressure in the central hole is reduced to model the gallery construction and to induce a damaged zone, similar to the Excavation Damaged Zone observed around galleries. Then a heating and cooling cycle is imposed in the central hole to simulate the thermal loading by the nuclear waste.

The first test on a sample cored parallel to the bedding planes developed a fracture pattern around the central hole after the mechanical unloading. Cracks sub-parallel to the bedding planes opened and lead to a buckling failure in two regions extending from the borehole in the direction normal to bedding. The geometry and extent of the "Excavation" Damaged Zone induced in this laboratory simulation test are similar to breakout patterns around openings parallel to bedding in the Mont Terri Underground Laboratory. A striking similarity is also found with the fracture pattern observed in a small-scale in-situ test performed by NAGRA in the framework of Work Package 4.1. In experiments performed on specimens cored perpendicular to bedding, there is no indication of failure around the hole and the response of the hollow cylinder sample is mainly isotropic. As for Boom Clay, this underlines the significance of the pre-existing planes of weakness (bedding planes) in Opalinus clay and the need for a correct consideration of the related mechanical anisotropy. This conclusion of a bedding controlled "Excavation" Damaged Zone is consistent with the distinct fracture patterns observed at Mont Terri depending on the orientation of holes/galleries with respect to the bedding planes.

Details of the test results are given in Deliverable 7.

2.4.2 Numerical results

The Itasca numerical simulation of a hollow cylinder test involves a discrete numerical code (*PFC2D*) coupled with a continuum code (*FLAC3D*). A pure hydraulic computation is performed using *FLAC3D* (three-dimension Finite Difference Method) while the thermal-mechanical response is calculated using *PFC2D* (two-dimension Discrete Element Method).
One EDZ-simulation test is modelled: the Test N°2/5 hollow cylinder test, performed by LMR-EPFL. The initial stress state is isotropic.

2.4.2.1 Constitutive models

The Discrete Element Code *PFC* allows simulating the movement and interactions of discrete bodies. The discrete medium is treated in 2D as an assembly of circular particles. *FLAC*^{3D} simulates transient fluid flow in saturated porous materials, coupled – or not – to the usual mechanical calculations of *FLAC*^{3D}.
The thermal option of *PFC* simulates transient heat conduction and storage in materials consisting of *PFC* particles, and the development of thermally induced displacements and forces. However, we chose not to model transient heat conduction at the microscopic level, because of

the time needed to propagate temperature at this scale. We perform independently a *FLAC3D* thermal model (in conduction only).

2.4.2.2 Creep model and sealing process

Creep is a time dependent deformation process occurring at the microscopic scale. It is assumed that microscopic bonds break during a small deformation under load. Simultaneously, new microscopic bonds will emerge when new contacts occur between particles (sealing process). Dependent on the ratio of breaking and emerging bonds the number of total bonds can increase or decrease. Bonds between particles weaken or strengthen with time.

2.4.2.3 Permeability-strain coupling model

The mechanical cycling is performed in *PFC2D*. *PFC2D* receives the hydraulic pressure data from *FLAC3D* and applies an equivalent hydraulic force on its particles. A porosity data feedback is then sent from *PFC2D* to *FLAC3D*. This enables *FLAC3D* to update the permeability field, for the next step in the evolution of the hydraulic pore pressures.
Porosity variation is translated in term of permeability evolution according to the initial permeability and a permeability multiplier, based on micro crack formation and local displacement increment.

2.4.2.4 Experiment numerical idealization

The hollow cylinder test has axisymetrical geometry. However, axisymetrical conditions have no physical meaning in a particle-based model. Moreover, the mechanical conditions (stresses, structural anisotropy of the Opalinus clay) are not axisymetrical. It is hardly possible at the present time to use a 3-dimensionnal discrete numerical model. However, due to the elongated shape of the experiment test specimen, we assume plane strain conditions for studying the mechanical effects. Thus, we develop the following numerical models:

- A three-dimension *FLAC3D* model is constructed for which the anisotropic of permeability is taken into consideration. A XY cross-section in the *FLAC3D* model corresponds to a quarter circle section.
- A two-dimension *PFC2D* model, taking into account structural anisotropy, is then integrated to be coupled with an XY cross section located at the middle of the *FLAC3D* model.

The test (N°2/5) aims at modelling at small-scale mechanical and thermal loads fairly similar to those that will be experienced by the host rock around disposal galleries for heat emitting radioactive waste.

2.4.2.5 Conclusion on modelling

A discrete numerical code (*PFC2D*) coupled with a continuum code (*FLAC3D*) provides a good reproduction of the experimental results.

- After the mechanical unloading, we observe a small increase of the permeability due to radial displacements, as a limited number of cracks appears near the borehole.
- After the thermal heating phase, the permeability increases by 2-3 orders of magnitude in the Y direction due to structure anisotropy, whereas as in the X direction the increase is by only one order of magnitude. The cooling phase leads to a compression of the borehole due to contraction of particles, and thus permeability decreases. The final

permeability in the X direction is the same as the initial one, whereas the Y permeability stays one order of magnitude higher than its initial value.

Mechanical and thermal loadings lead to an ovalisation of the borehole. This deformation is due to the orientation of the bedding planes, which induces more cracks in the bedding planes and thus more deformation in the direction normal to the bedding.

The numerical model produces evolutions similar to the ones observed in the experimental test (Test N°2/5). However, in the model, the larger permeability does not decrease back to its original value at the end of the test.

2.4.3 Conclusion

Numerical results obtained show that the numerical model associating permeability-strain coupling model and creep/sealing model allows the reproduction of the permeability increase/decrease of the damaged sample.

Nevertheless the experimental results seem to be strongly influenced by the probable desaturation after sample removal from the testing cell (several hundred days of waiting before analysis). Desaturation is likely to have modified the fracture pattern (as observed in sample N°12) and thus complicates comparison with the numerical results.

3 Simulation of small scale in-situ tests

3.1 *ATLAS III*

Within the TIMODAZ project, a small-scale in situ test named ATLAS III has been performed in order (1) to obtain a more accurate and extended field of the temperature and pore water pressure by recently drilling two additional boreholes equipped with more sensors, which enables to check the possible thermal anisotropy. (2) To test a new data acquisition system which has a higher data acquisition rate and is fully automatic instead of a low-rate and manual data acquisition system used in ATLAS I and II. (3) To have better assessment of THM characterisation of Boom clay at larger scale and at different temperature levels. (4) To serve as preparation for Praclay Heater Test, which is a large scale heater test in Boom clay intending to simulate a disposal gallery at real scale, and to provide a good link with Praclay heater test by up-scaling. (5) To provide data for a modelling benchmark in the European project TIMODAZ (2006~2010).

Withing the work package WP5.2, it has been decided to perform a modelling benchmark based on this in situ test. In a first step, the benchmark has been defined as a blind prediction test with three different geometries, enabling the participating teams to consider different levels of complexity. A one-dimensional axisymmetric model is easy to handle and gives first insights of the relevant physical phenomena. A 2D axisymmetric geometry helps to reproduce better the experiment, in the radial direction and the axial as well. Finally, as far as anisotropy was suspected to play an important role, a fully 3D model has been also proposed for the benchmark exercise. Of course, all the teams were let free to select the geometry they want to deal with for this benchmark.

In a second step, in addition to the benchmark exercise, series of additional computations have been carried out in order to study some more specific features of behaviour that have been underlined during the experiment. Those simulations consist, for most of them, in an analysis and a constitutive interpretation of in situ results in order to validate and calibrate the used numerical models and materials parameters. For this step of the work, the liberty was given to use the constitutive models, the geometry of the mesh and the boundary conditions that each team considers as the most appropriate regarding to the features of behaviour that they expected to observe.

This executive summary presents the main concepts and results that have been obtained in the framework of the numerical modelling of the ATLAS III in situ test. It is divided in three parts: the in situ test brief description, the benchmark exercise and the additional computations.

3.1.1 Test setup and field data

The original set-up was developed in 1992 by SCK-CEN within the framework of the European project Interclay II (1990~1994). The test was re-activated from June 1996 to May 1997 (ATLAS II). In 2006, the set-up has been refurbished; the heater was activated from April 2007 to April 2008. This was thus the third life of ATLAS test and therefore named ATLAS III.
One of the objectives of ATLAS III test is to provide data for a modelling benchmark in the European project TIMODAZ (2006-2010); that's why it is now briefly described.

Test set-up

The test setup is composed of a central borehole with heater and of four boreholes with instrumentation. To obtain measurement over a larger range in ATLAS III than that in ATLAS I and ATLAS II, to test the piezometer design and installation envisaged for Praclay gallery, to serve as a far field piezometer for the future large scale Praclay Heater Test, and to get a better picture of the possible thermal anisotropy, the two additional boreholes AT97E and AT98E have been drilled. The main borehole (AT89E) with heater and three other boreholes (AT85E, AT93E, and AT98E) are in the same horizontal plane while a last borehole (AT97E) is slightly inclined towards the heater borehole. The inclination is about 10° down and 10° towards the heater borehole. Figure 28 illustrates the layout of the ATLAS III test.

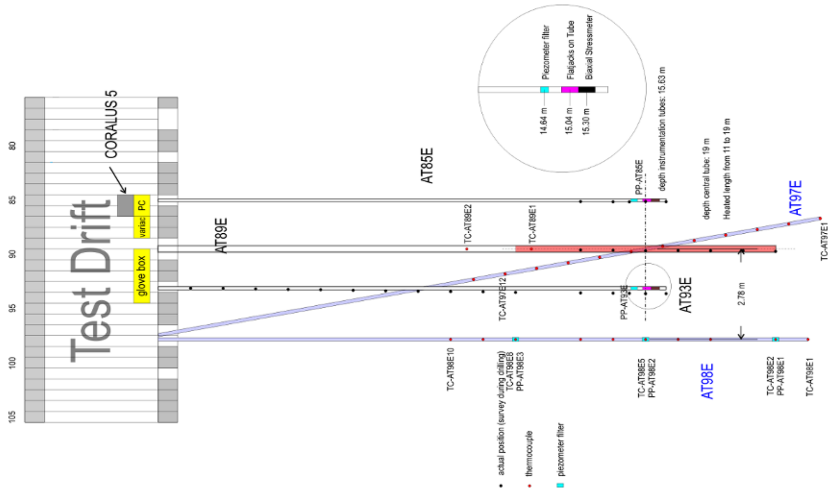

Figure 28: Layout and instrumentation of ATLAS III in situ test

The heater has been re-activated on April 2, 2007 starting with a relatively low heating power of 400 W, the power has been increased step wisely to 900 W then to 1400 W and was finally shut off instantaneously on April 17, 2008 to observe the effects of the cooling transient. Until Nov. 2, 2009, ATLAS III test has lasted for 945 days, with heating for 381 days and cooling for 564 days.

Field data

ATLAS III test yielded a large amount of good-quality data on the thermal, hydraulic and mechanical perturbations. Some interesting phenomena are revealed by the measurements of temperature, pore water pressure and total stress.

Measured temperature

As indicated in Figure 28, there is one temperature sensor in AT85E, one temperature sensor in AT93E, twelve temperature sensors in AT97E, and ten temperature sensors in AT98E. The measured temperature are displayed in Figure 29, where the vertical dashed lines indicate the times of increasing power or shutting down the power. The experimental measurements of temperature can be summarized as follows. First, the temperature increase is inversely proportional to the distance from the heater (Figure 29): the shorter the distance is, the larger the increase of temperature is. Secondly, the successive heating steps are well visible at all the sensors (Figure 29). Thirdly, all measured temperatures by sensors show a delay of the temperature decrease after switching off the heater. This delay is proportional to the distance from the heater.

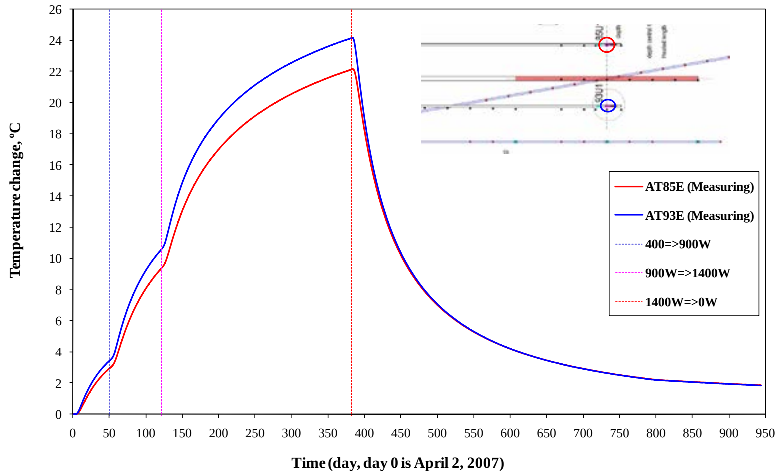

Figure 29: Temperature increase of sensors located in boreholes AT85E and AT93E

Measured pore water pressure

Figure 30 shows the evolution of the pore water pressure. The maximum pore water pressures increase ranges between 0.5 MPa and 1.0MPa. At the end of March 2008, the sudden drop of pore pressure is imposed on the piezometer PP-AT85E in order to determine the permeability of the massif near this sensor. It is interesting to observe that at the start of each heating phase, a temporary decrease of the pore pressure occurs in all the piezometers. The opposite phenomenon is observed when switching off the heater. The pore water pressures are now tending to recover slowly to their initial states before heating.

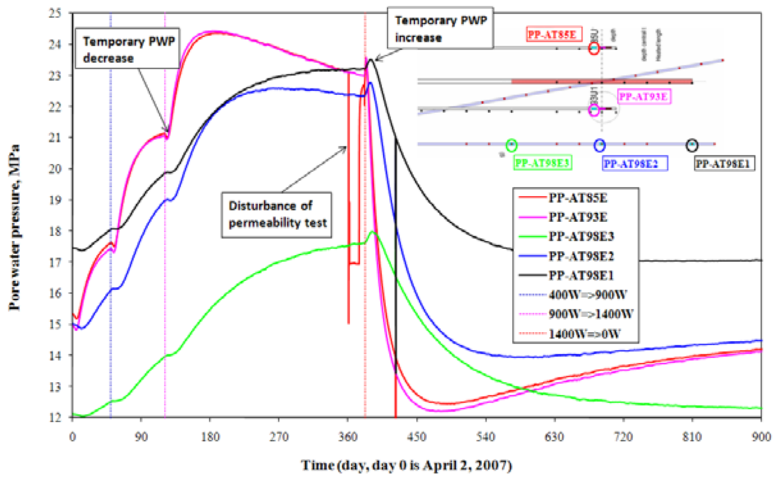

Figure 30: Evolution of pore water pressures in five sensors located in boreholes AT85E, AT93E and AT98E

Measured total stress

From the temporal evolution of the total stress measured by flatjacks, it can be observed that the total stresses present variations with the different sensors orientations for both AT85E and AT93E; besides, the temporary decrease of total stress at the start of each heating phase and temporary increase of total stress at the start of cooling phase are also noticed.

3.1.2 Benchmark exercise

Problem definition

The benchmark exercise consists in the reproduction of the heating and the cooling phases. Figure 31 presents the geometry of the experiment used for the modelling.

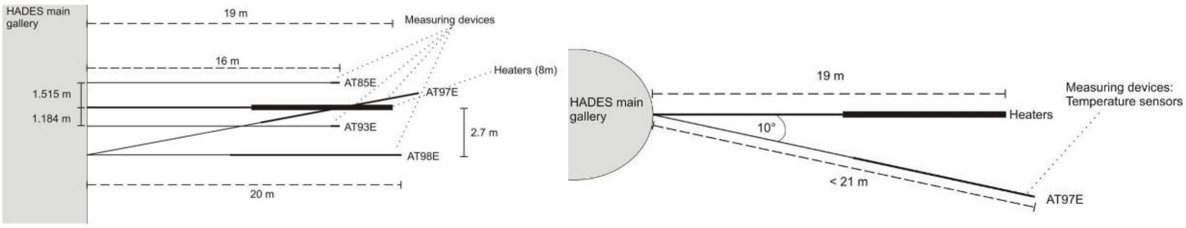

Figure 31: Geometry of ATLAS III. View in a horizontal plane and in a vertical plane

The experimental procedure consists in a thermal loading applied at the heater borehole. The thermal loading is composed of three steps. The first one rises the power from 0 to 400 W in four days and a period of 45 days of stabilisation is allowed. The second one enhances the power from 400 W to 900 W in five days and a period of 66 days of stabilisation is allowed. Finally, the third one, the power is increased up to 1400 W in five days and a period of 256 days of stabilisation is allowed. Then, the power is shut off instantaneously and a cooling phase goes on 69 days. At the difference to the experiment, the modelling stops after 450 days. Indeed, all the cooling phase is not modelled because the benchmark exercise was launched in January 2009 and the experiment ends in November 2009. As a consequence, only 69 days of the cooling cycle have been considered in this exercise. Of course, all the heating phases are considered.

The clay is initially considered as homogeneous. It is supposed to be fully saturated. Initial conditions are listed in Table 4. For Boom Clay, they are close to the ones encountered in the clay formation. The gravity will not be considered in the modelling. These initial conditions are the same for the three geometries used for the computations.

Initial state		Boom Clay
Total stresses [MPa]	$\sigma_x=\sigma_y=\sigma_z$	4.5
Pore pressure [MPa]	p_{w0}	2.25
Temperature [°C]	T_0	16.5

Table 4: Initial state – stresses, pore water pressure and temperature

The three proposed geometries correspond to an idealization of the ATLAS III experiment with an increasing complexity. The first model is a 1D axisymmetric model, which is the easiest model to realise. This model rapidly permits to have an overview of the physics implied in this modelling. The problem is of course not only a one-dimensional (radial) experiment and a 2D axisymmetric model is also proposed in order to quantify the effects (THM) of the heating in the axial direction. Finally, a 3D model is also proposed to evidence the impact of some anisotropy in the constitutive models.

Geometry

Figure 32 and Figure 33 present the geometry for one-dimensional problem (radial-axisymmetric) and the 2D axisymmetric and 3D model respectively. The inner and the external radius are respectively equal to 0.095 m and 100 m. For the 2D and 3D modelling, the height of the model is 119 m. The inner radius corresponds to the radius of the borehole equipped with heaters.

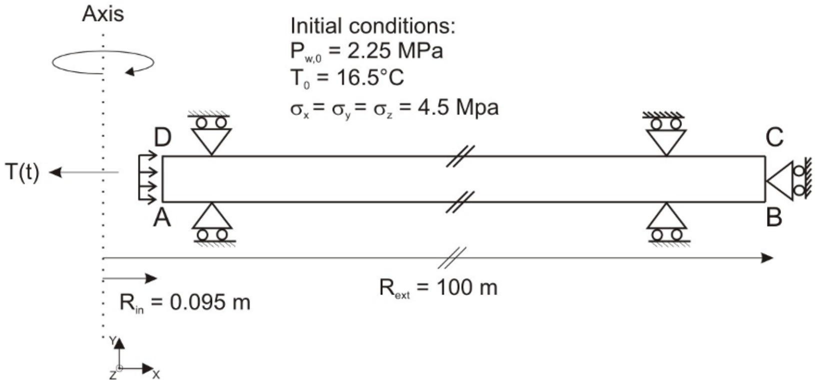

Figure 32: Illustration of the geometry of the 1D modelling

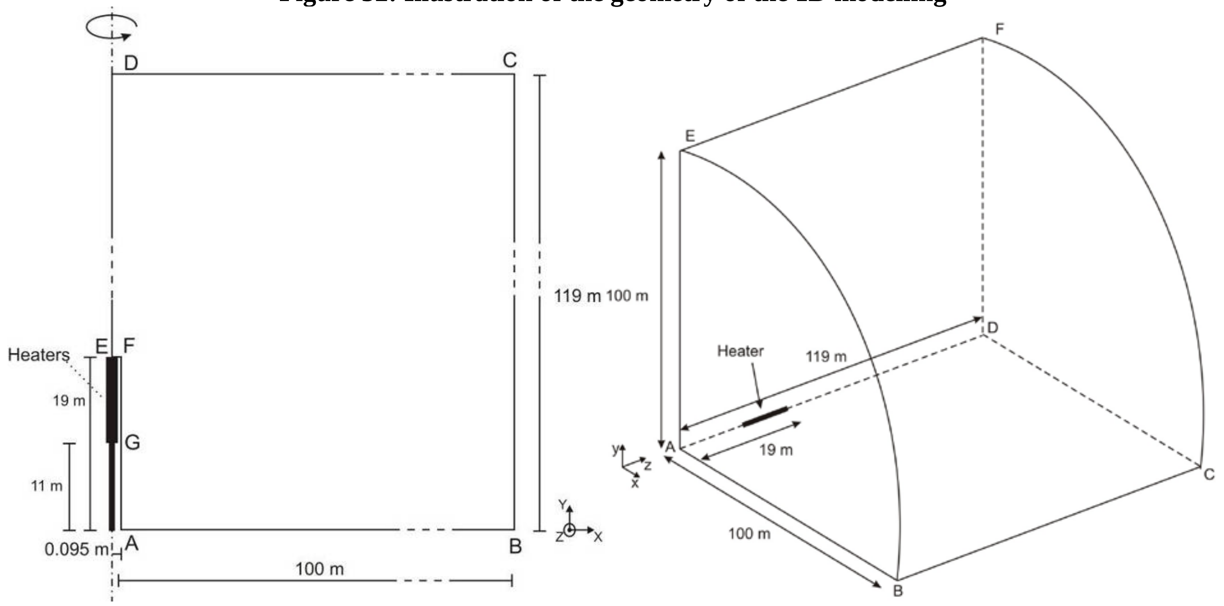

Figure 33: Schematic representation of the 2D axisymmetric and 3D modelling

Boundary conditions

We present in the following the boundary conditions used in this 2D modelling. The 1D axisymmetric and the 3D boundary conditions derive directly from the ones depicted in the following.

Mechanical boundary conditions are defined as followed: (1) Axial displacements are fixed on the external boundaries DC, AB and EF. (2) Radial displacements are fixed on the boundaries ED, BC and AF.

Hydraulic boundary conditions: (1) Pore water pressure are fixed on the boundaries DC, CB. (2) Boundary from the point A to point D is impervious. The boundary AB is also impervious.

Thermal boundary conditions: (1) Boundaries AB, BC, CD, DE and FA are adiabatic. (2) Heat flux is imposed on boundary FG.

Mechanical model

In this benchmark, the mechanical properties of Boom clay may be considered as isotropic or anisotropic. Indeed, the structure of clay in band layers (Mertens et al., 2003) permit to consider this material as transversely isotropic. Only elastic model have been considered in this modelling because the size of the EDZ is relatively small (as the borehole diameter is small) compare to the extent of host rock affected by the thermal process. That is the reason why the excavation of the borehole has not been considered: no EDZ has been created and a thermo-elastic modelling seems sufficient to reproduce the effect of the temperature far away from the heater. For both mechanical models, the total strain rate $\dot{\varepsilon}_{ij}$ is considered as the sum of the mechanical elastic strain rate $\dot{\varepsilon}_{ij}^{m,e}$ and the thermal elastic strain rate $\dot{\varepsilon}_{ij}^{e,th}$:

$$\dot{\varepsilon}_{ij}^{e} = \dot{\varepsilon}_{ij}^{m,e} + \dot{\varepsilon}_{ij}^{th,e} \quad \text{with} \quad \dot{\varepsilon}_{ij}^{th,e} = \beta \dot{T} \delta_{ij} \tag{0.7}$$

Linear isotropic elasticity

The first mechanical model considers only an isotropic elastic law, which can be summarised by the following equation:

$$\dot{\sigma}_{ij} = C_{ijkl}^{e} \dot{\varepsilon}_{kl}^{m,e} \tag{0.8}$$

with two elastic parameters, E is the Young’s modulus and υ the Poisson’s ratio.

Linear transversely isotropic elasticity

The second proposed mechanical model still considers an elastic model but, in this case, the Hooke’s law defines a transversely isotropic elastic medium. The behaviour of a transversely isotropic material may be described by five independent parameters (Love, 1944). The required material parameters are two Young’ modulus (E_v and E_h), two Poisson’s ratio (ν_{vh} and ν_{hh}) and a shear modulus (G_{vh}). The subscripts *v* and *h* will be used for stiffness parameters to indicate vertical and horizontal directions respectively. Poisson’s ratio for strain in the vertical direction due to a horizontal direct stress is ν_{vh}. Poisson’s ratio for strain in any horizontal direction due to a horizontal direct stress at right angles is ν_{hh}. The remaining parameters are not independent.

Hydraulic and thermal constitutive models

Darcy’s Law

The general Darcy flow law is used and defines the Darcy fluid velocity $\underline{q}_w$ as a linear function of permeability and the gradient of fluid pressure p_w:

$$\underline{q}_w = -\frac{\underline{\underline{k}}_w}{\rho_w . g} \left(\underline{\nabla} p_w \right) \tag{0.9}$$

where $\underline{\underline{K}}_w$ is the anisotropic tensor of permeability. This tensor has nine components and may be written in a general form as follows:

$$\underline{\underline{k}}_w = \begin{bmatrix} k_{xx} & k_{xy} & k_{xz} \\ k_{yx} & k_{yy} & k_{yz} \\ k_{zx} & k_{zy} & k_{zz} \end{bmatrix} \tag{0.10}$$

If the medium is supposed to be isotropic, the relation becomes:

$$\underline{q}_w = -\frac{k_{\text{int}}}{\mu_w}\left(\underline{\nabla} p_w\right) \tag{0.11}$$

where k_{int} is a scalar in isotropic situation [m²] .

Fourier's Law

The general Fourier's law is used to describe the conduction of heat in the medium. This law is expressed by:

$$\underline{i}_{cond} = -\underline{\underline{\lambda}}_m . \underline{\nabla} T \tag{0.12}$$

Where $\underline{\underline{\lambda}}_{\text{m}}$ is the anisotropic tensor of the conductivity of the medium. In a general form, this tensor has 9 components and is written:

$$\underline{\underline{\lambda}}_m = \begin{bmatrix} \lambda_{xx} & \lambda_{xy} & \lambda_{xz} \\ \lambda_{yx} & \lambda_{yy} & \lambda_{yz} \\ \lambda_{zx} & \lambda_{zy} & \lambda_{zz} \end{bmatrix} \tag{0.13}$$

In the same way as the Darcy' law, the Fourier' law for an isotropic material is:

$$\underline{i}_{cond} = -\lambda_m . \underline{\nabla} T \tag{0.14}$$

Liquid dynamic viscosity (μ_w [Pa.s])

$$\mu_w(T) = \mu_{w0} - \alpha_w . \mu_{w0} . (T - T_0) \tag{0.15}$$

where α_w is the liquid dynamic viscosity thermal coefficient [K^{-1}], T_0 is a reference temperature and μ_{w0} is liquid dynamic viscosity at reference temperature.

Water density (ρ_w)

$$\rho_w(T, p_w) = \rho_{w0} . \left[1 + \frac{p_w - p_{w0}}{\chi_w} - \beta_w . (T - T_0) \right] \tag{0.16}$$

where β_w is the liquid volumetric thermal expansion coefficient [K^{-1}], $1/\chi_w$ is the liquid compressibility coefficient [MPa^{-1}], ρ_{w0} is the density at reference temperature and p_{w0} is a reference pore pressure.

1D RESULTS

Figure 34 represents the evolution of the pore water pressure and the temperature with time. The power of the heater is increased in 3 steps. After each increase, the power is maintained constant. Figure 34 shows that a maximum of 100 °C at the inner radius is attained at the end of the third heating phase. Finally, when the heater is switched off, the temperature quickly decreases. The evolution of the pore water pressure is related to the thermal dilation of water, which is more important than the dilation of the solid. When the power is maintained constant, the pore water pressure is quiet stabilised. Finally, a decrease of pore pressure is observed during the cooling phase.

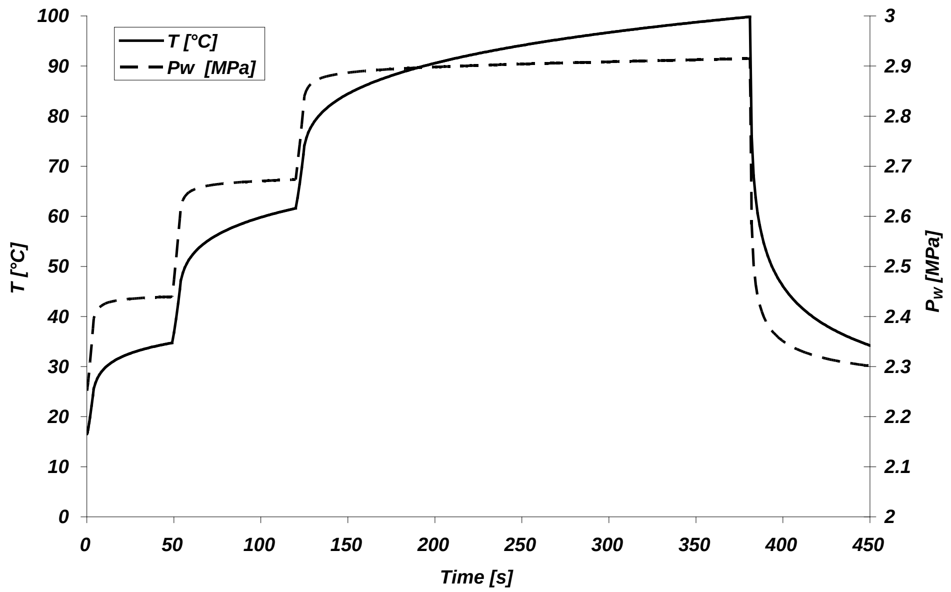

Figure 34: Evolution of the temperature and the pore water pressure at the inner cavity

The heat generated by the increase of the power dissipates into the medium. As a consequence, the temperature increases around the heater during the three phases of heating. The thermally affected zone grows with time due to the dissipation of the heat. When the power is switched off, the temperature near the cavity decreases but dissipation of the heat goes on and the temperature continues to increase in the far field.

The evolution of the pore water pressure with the radial distance is described in Figure 35, which shows the pore water pressure increases around the heater during the heating phase (profiles at 4, 54, 125 and 250 days). On the contrary, the reduction of the temperature induces a decrease of the pore pressure near the heater (profile at 450 days). But due to the dissipation of the heat, during the cooling phase, the pore water pressure continues to increase in the far field.

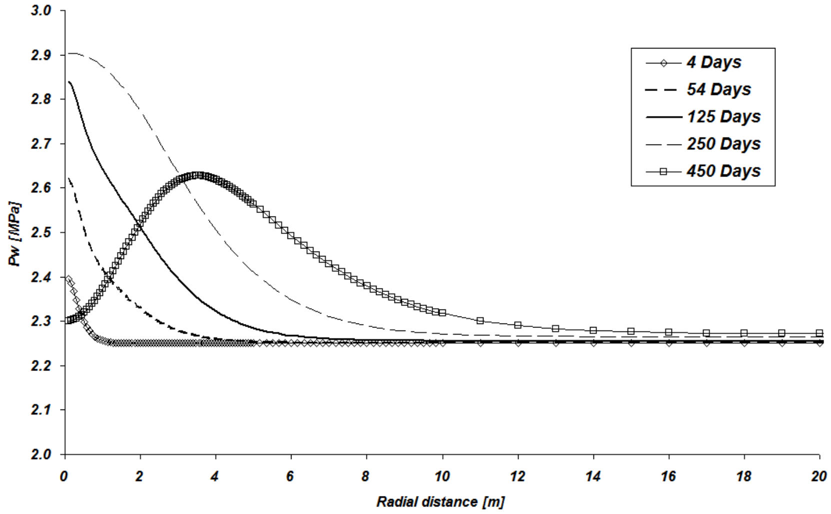

Figure 35: Evolution of the radial profiles of pore water pressure for various times

2D RESULTS

The radial distribution of the temperature leads to the same conclusion as previously in 1D modelling. The increasing power induces an increase of the temperature, whereas a decrease is observed during the cooling phase when the heater is switched off. However, at the difference to the 1D modelling, the dissipation of the heat in the 2D model can occur in 2 directions, whereas this dissipation concerns only one direction in 1D modelling. That is the reason why the maximum temperature at the inner radius is lower in the 2D modelling.

The evolution of the pore water pressure is analogous to the results obtained in the 1D modelling. But, on the contrary of the 1D case, the pore water pressure reaches a value lower than the initial value at the end of the modelling. This effect is related with the drainage, which has two components in 2D. Actually, the drainage can be axial or radial unlike in the 1D where the component of the drainage is radial.

3D RESULTS

This section presents the results obtained with the 3D modelling considering mechanical, hydraulical and thermal anisotropies.

Figure 36 presents the spatial distribution of the temperature at different times for the profile 1 and the profile 4. Due to the difference of thermal conduction, the temperature is greater in the far field for the profile 4 as compared to profile 1.

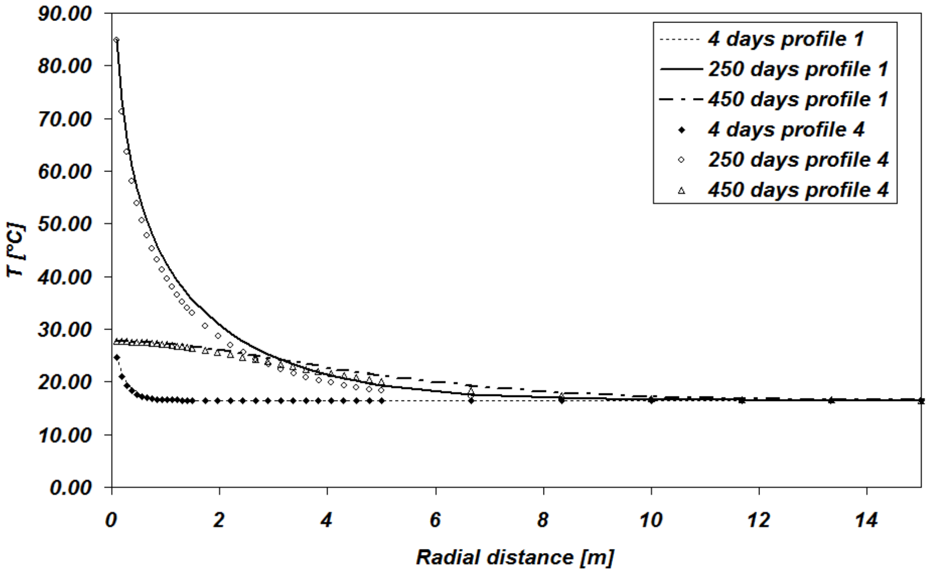

Figure 36: Distribution of the temperature according profile 1 and profile 4

As compared to isotropic case, the effect of all this anisotropy is to generate higher pore water pressures. Figure 37 shows the difference obtained for the pore water pressure evolution at AT85E between this anisotropic case and the isotropic case.

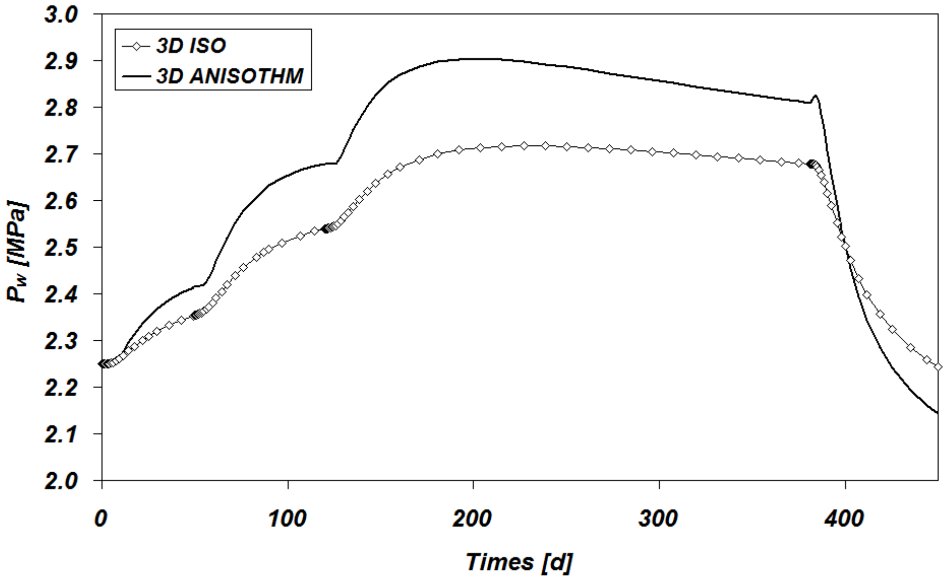

Figure 37: Evolution of the pore water pressure in the full anisotropic model and in the isotropic model at AT85E

COMPARISON WITH EXPERIMENTAL RESULTS

This section presents some comparisons between experimental and predicted data. Figure 38 presents a comparison of the temperature changes for the 1D and the 2D calculations. We show that the temperature increase is quite similar between the 2D and the experimental results.

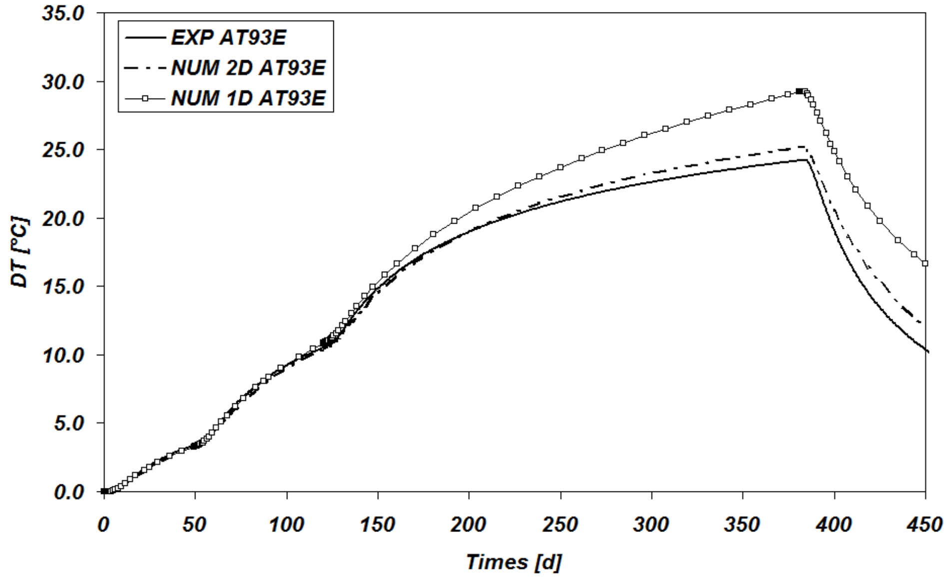

Figure 38: Comparison between the experimental results and the numerical results for the sensor located in the boreholes AT93E

In 2D modelling, the comparisons between the temperature evolution recorded and the numerical results show good agreement for some sensors in the horizontal plane. Figure 39 presents a comparison between the temperature recorded and the numerical results for some sensors of AT97E. This borehole is inclined compared with the horizontal plane. The result of this comparison shows that all the numerical results do not fit the experimental curves.

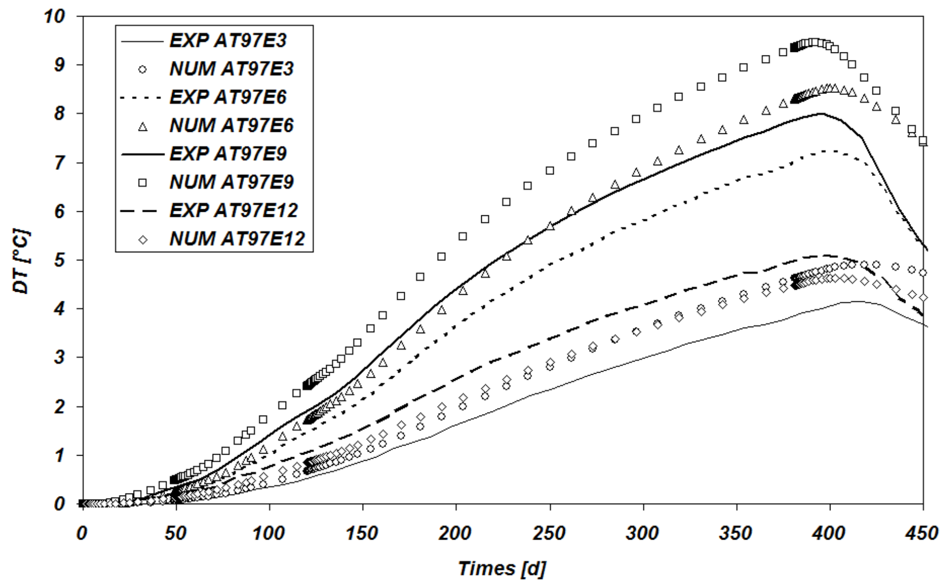

Figure 39: Comparison between experimental results and numerical results for sensors in the borehole AT97E

The evolution of the pore water pressure is different between modelling and experiment. Figure 40 presents the comparison between the experiment and the modelling. In both case, we see that the evolution of the pore pressure is underestimated.

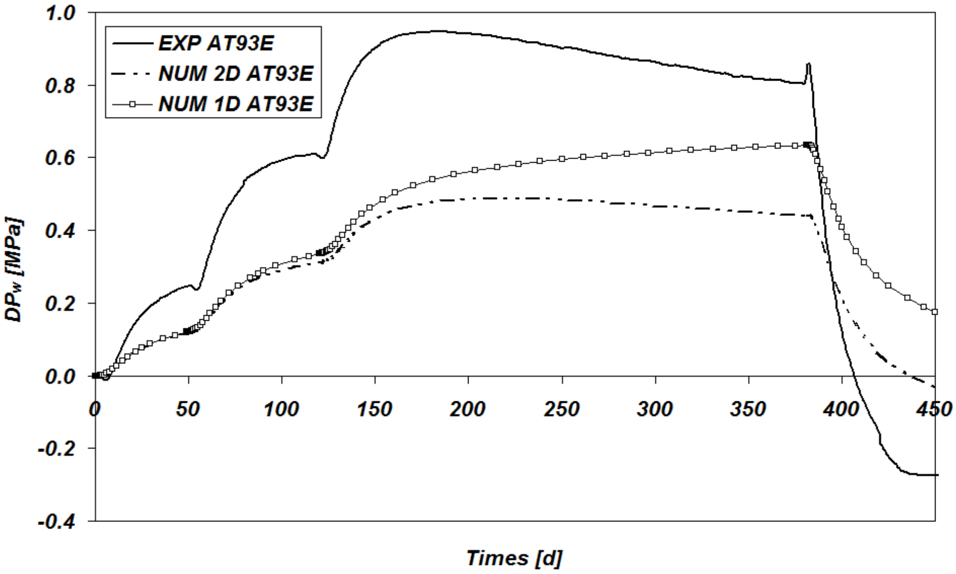

Figure 40: Comparison of the evolution of the incremental pore water pressure between experimental and numerical results

In 3D modelling, a comparison between the evolutions of the temperature for the different sensors has been realised. Figure 41 presents a comparison between the experimental data and the numerical results for the sensor AT97E. We can observe that the comparison between experimental and numerical results is quiet good for these sensors. The anisotropic parameters of the thermal conductivity permits to better reproduce the observed evolution as compared with the isotropic case. For the sensors of AT98E, the 3D numerical results are good except for AT98E10 and AT98E5. This means that some improvements have to be done in the calibration of the thermal parameters.

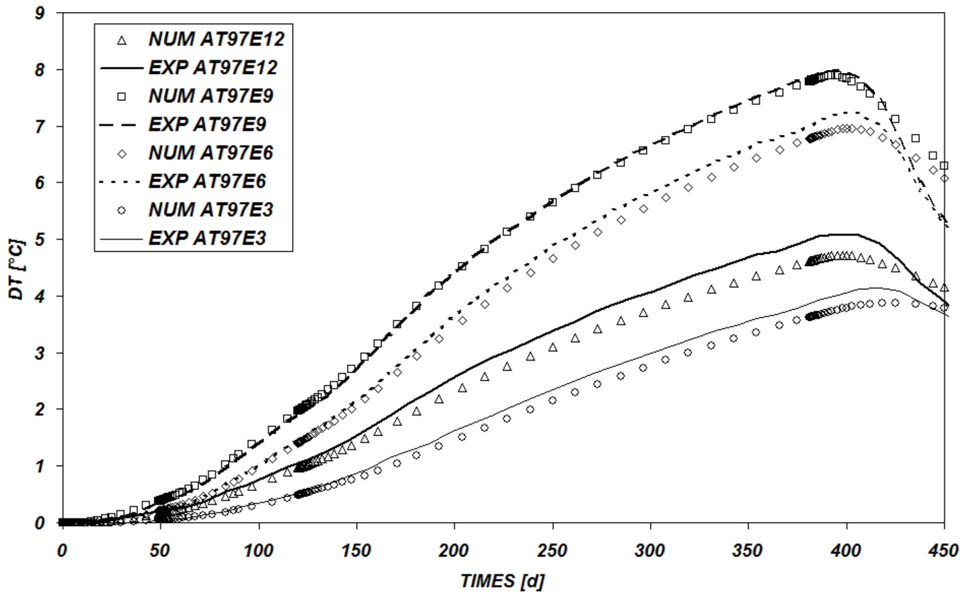

Figure 41: Comparison between the experimental and the numerical data for some sensors of AT97E

Concerning the evolution of the pore water pressure, the evolution is similar for 3D numerical results and experimental data, but the numerical results underestimate the observed evolution. This comparison is done in Figure 42 for the sensors AT85E and AT93E.

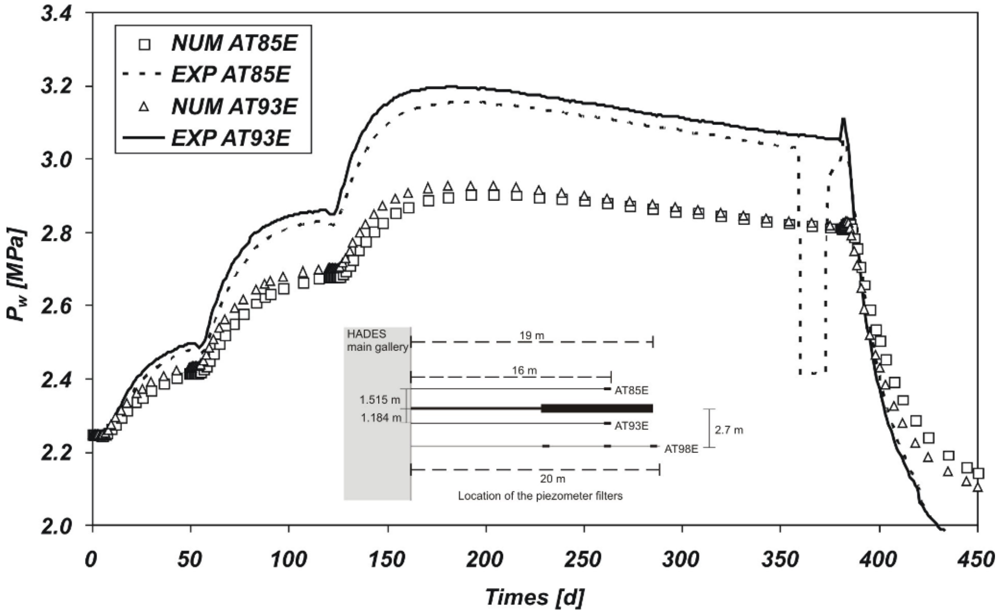

Figure 42: Comparison of the observed excess pore water pressure and the numerical result

3.1.3 Additional computations

Additional computations by ULg

During this benchmark exercise, ULg has realised different 3D modellings considering different sources of anisotropy. Indeed, the anisotropy can be considered in the mechanical, the hydraulical or thermal problem. The aim of this work is to study each case of anisotropy separately, in order to better understand their influence on the results and especially on the excess pore water pressure and on the thermal dissipation.

Considering anisotropy in the mechanical model, ULg uses a transversely isotropic elastic law with five independent parameters. The anisotropic model has two consequences (Figure 43): on one hand, a higher pore water pressure is obtained with this law due to a higher value of the elastic moduli. On the other hand, it is important to note that, only with the anisotropic mechanical model, an increase of pore pressure is observed when decreasing the heat power. The same observation has been made based on the in situ measurements. The phenomenon is also observed when increasing the heat power. But the numerical increase is less large than that of the in situ measurements.

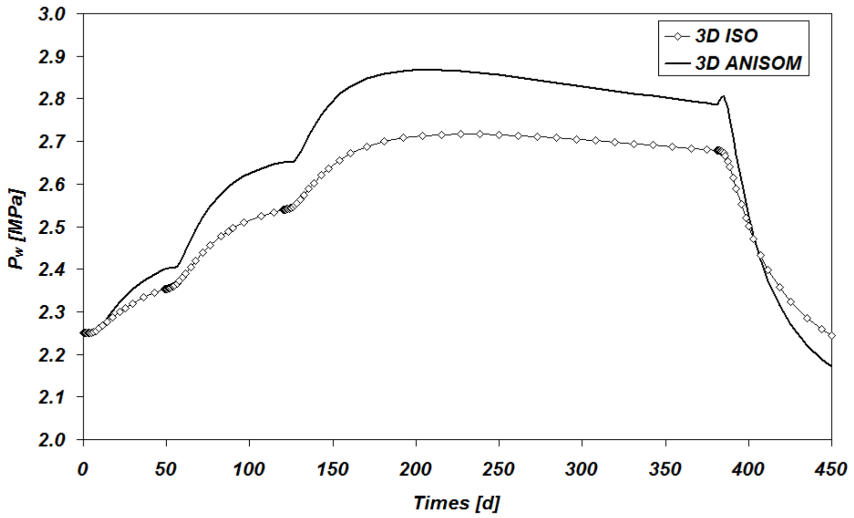

Figure 43: Comparison of the evolution of the pore water pressure for the senor AT85E between the isotropic case and the mechanical anisotropic case

The hydraulic anisotropy has also an influence on the results but can not produce a significant improvement of the predictions for the range of permeability considered in the modelling.

The thermal anisotropy is characterised by a vertical thermal conductivity smaller than the horizontal conductivity. As a consequence, the dissipation of the heat in the horizontal direction is larger than in the vertical direction (Figure 44). This anisotropy allows a better fitting of the temperature measurements at the different boreholes.

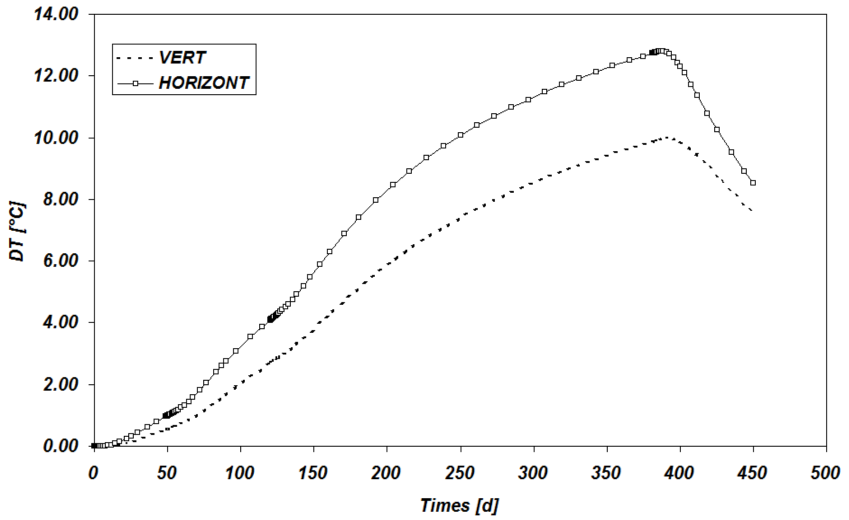

Figure 44: Evolution of the temperature for two points located at a distance of 2.75 m from the heater

Additional computations by EPFL

The EPFL team carried out the computations with an additional objective in mind; to assess the influence of non-linear thermo-elasticity and thermo-plasticity on the THM response of the repository.

Mechanical model

The ACMEG-T constitutive model accommodates non-linear thermo-elasticity coupled with a multi-dissipative thermo-plasticity in order to reproduce most thermo-mechanical features. The elastic part of the deformation increment $d\boldsymbol{\varepsilon}^e$ is expressed as following:

$$d\boldsymbol{\varepsilon}^e = \boldsymbol{D} d\boldsymbol{\sigma}' - \boldsymbol{\beta}'_T \, dT \tag{0.17}$$

$\boldsymbol{D}$ is the mechanical elastic tensor defined by the non-linear bulk and shear modulus, K and G, respectively,

$$K = K_{ref}\left(\frac{p'}{p_{ref}}\right)^{n^e} \; ; G = G_{ref}\left(\frac{p'}{p_{ref}}\right)^{n^e} \tag{0.18}$$

where p' is the mean effective stress, n^e the non-linear elasticity exponent, p'_{ref} the reference pressure, K_{ref} and G_{ref} the bulk and shear modulus at the reference pressure, respectively. $\boldsymbol{\beta}'_T$ is the thermal expansion tensor. Considering an isotropic thermal dilatation, one can express the thermal expansion tensor as $\boldsymbol{\beta}'_T = 1/3\beta'_s \boldsymbol{I}$ with β'_s being the volumetric thermal expansion coefficient of the solid skeleton.

Using the concept of multi-mechanism plasticity, the total irreversible strain increment $d\boldsymbol{\varepsilon}^p$ is induced by two coupled dissipative processes: an isotropic and a deviatoric plastic mechanism. Each of them produces plastic strain increment, $d\boldsymbol{\varepsilon}^{p,iso}$ and $d\boldsymbol{\varepsilon}^{p,dev}$, respectively.

The 2D results of EPFL are briefly presented to highlight the influence of non-linear thermo-elasticity and thermo-plasticity on the THM response of the repository (Figure 45).

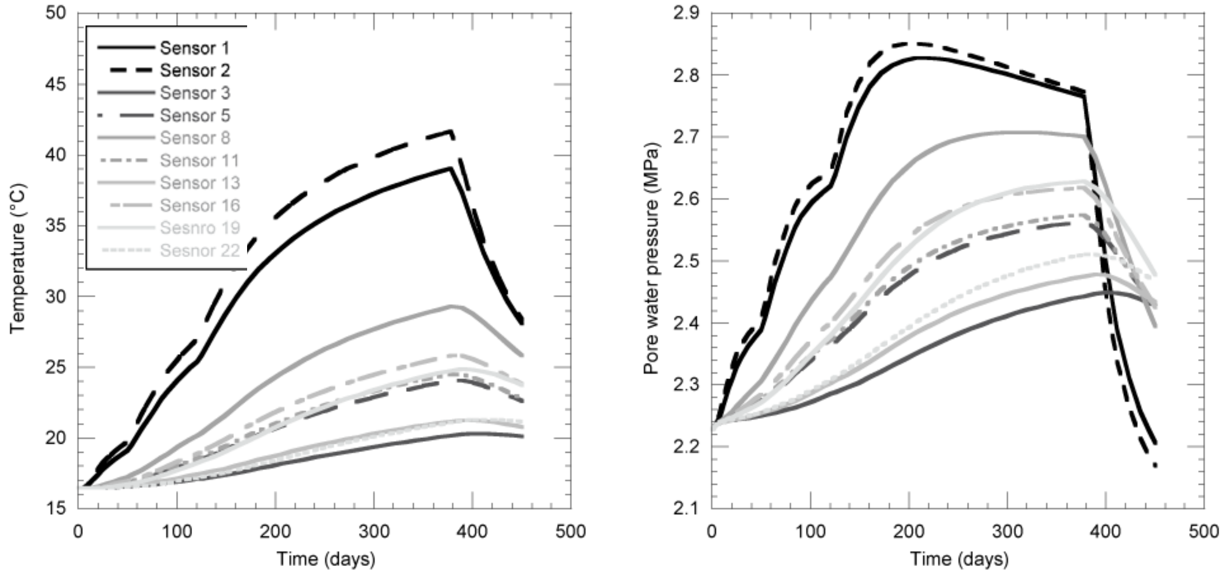

Figure 45: Time evolution of temperature, pore water pressure in the 2D modelling

The obtained pore pressures and stress fields differ from those obtained by the other teams. The differences are mainly due to the non-linear elasticity and the thermo-plasticity of the ACMEG-T model. An increase in rigidity as well as progressive plasticity induced by heating, causing an increase of the preconsolidation pressure, is considered in ACMEG-T. This causes an increase in excess pore water pressures, and consequently in effective stresses.

Additional computations by EURIDICE

Several additional cases of three dimensional coupled THM modellings were performed for ATLAS III test in order to interpretate the field data of pore water pressure. The 3D model was the same that the model proposed in the benchmark exercise, except that a steel tube with 19 m length, 95 mm external radius and 15 mm thickness was included in the geometry. The initial stress state differs from the proposed one by the fact that a lateral total stress coefficient $K_0 = 0.85$ is considered in the modelling.

Based on the selected THM parameters, especially the thermal conductivity, the best comparison of temperature between measurement and modelling we obtained is presented in Figure 46, and the comparison can be considered excellent.

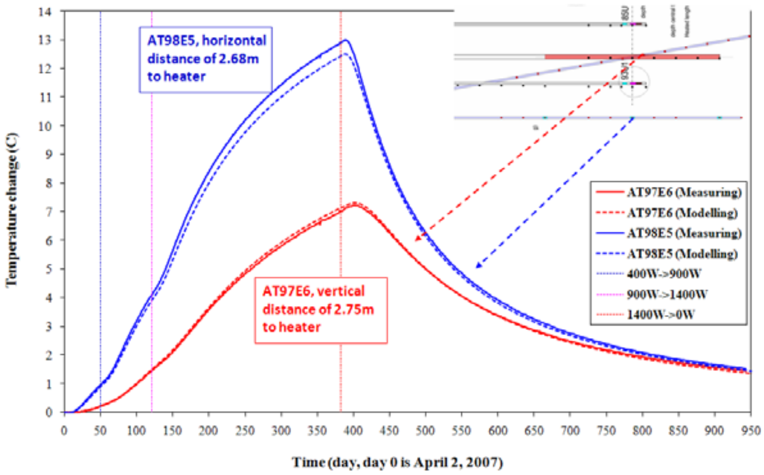

Figure 46: Comparison between modelling and measurement of temperature in sensors TC-AT98E5 and TC-AT97E6

To reproduce the measured pore water pressure by modelling, many cases have been calculated: isotropic elasticity, anisotropic elasticity and a Camclay model. The conclusion is that only with the anisotropic elastic parameters (E_h=700 MPa, E_v=350 MPa, G_v=140 MPa being used), the temporary pore pressure decrease (increase) after increasing (switching off) the power can be reproduced, but the measured pore pressure change is still around 30% underestimated by modeling. The comparison with good match between measured pore water pressure and modelled one is obtained especially by using the doubled moduli than in case 2: the modelling can not only well reproduce the temporary pore water pressure decrease after increasing power and temporary pore water pressure increase after cooling in all the five piezometers, but also it gives the close magnitude of the pore water pressure change to the measured one. The magnitude of the used Young's modulus is close to the one that can be obtained from the wave velocities of seismic tests on undisturbed Boom clay in HADES [9].

From the above several cases, it could be found that (1) only when anisotropic mechanical parameters are used, the modelling can reproduce the temporary pore water pressure decrease after increasing power and temporary pore water pressure increase after cooling observed in all the five piezometers, which provides the indirect evidence of the mechanical anisotropic behaviour of Boom clay; (2) Higher Young's moduli could be reasonably employed to obtain better comparison of pore water pressure between modelling and measurement.

Additional computations by CIMNE

CIMNE did a number of additional 3D THM computations to analyse the temperature and pore water pressure measurements registered in the third phase of the ATLAS experiment. The code used is Code_Bright and a description of the Thermo-Hydro-Mechanical formulation may be found in (CODE-BRIGHT, 2004). Anisotropic thermal conduction law, anisotropic water flow and anisotropic elastic constitutive law were used. The gallery from where the heating borehole was drilled and the heater itself are discretized explicitly. In contrast with other teams, a draining boundary condition was applied on the heater walls.

The thermal problem was solved for any possible combination of thermal conductivity couple. The best fitting thermal conductivity couple was determined for each sensor and each heating stage according to a method developed in (Garitte et al., 2009). The results are summarized in Figure 47-a. The average obtained from all the sensors is very close to the reference values (1.7-1.2W/m/K**)**. The same exercise was repeated using a power loss coefficient. For a power loss coefficient of 85%, the best fitting thermal conductivity couple converges 1.4-0.9W/m/K for all sensors as shown in Figure 47-b (1.4-0.95W/m/K).

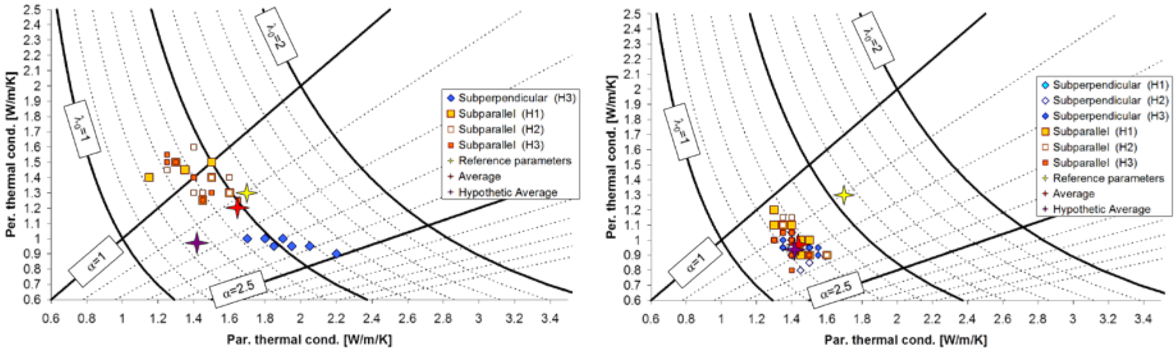

(a) (b)

Figure 47: Thermal conductivity values determined for each sensor and each heating period in the ATLAS experiment (a) 100% of the power (b) power loss coefficient of 85% . The yellow four branches star indicates the reference thermal conductivity values and the red four branches star the average thermal conductivity from this study.

The applied thermal load triggers a Hydro-Mechanical response of the rock as both, the rock skeleton and the water in the rock pores expand when heated. The hydro- and the mechanical response are tightly coupled. The heated volume around the heater undergoes an expansion as a consequence of the temperature increase. The constant temperature rock volume reacts mechanically to the expansion of the heated volume: the non-heated volume has a tendency to radial compression and circumferential expansion (relative to the heater).

As soon as the temperature starts to increase, two processes are in competition: compression of the water because thermal expansion of the water is larger than that of the rock skeleton and dissipation of the generated excess pore pressure. In a first stage, pore water pressure will increase: compression of the water is stronger than the dissipation. It should be noted that the pore water pressure increase rate depends on 1) the temperature increase rate and 2) the permeability of the medium. After some time, temperature increase rate decreases and excess pore water pressure starts to dissipate faster than they are generated by the temperature increase. Note that the dissipation of high pore pressures in the near field may also trigger an increase of pore water pressure in the far field.

Pore water pressure changes generated by temperature changes also contribute to the deformation of the medium through the effective stress concept.

Excess pore water pressure measured in the five sensors of the ATLAS experiment is plot against simulation results in Figure 48. The good agreement between measurements and simulation was achieved by introducing one change in the Boom clay reference parameter set: the equivalent water permeability was decreased from 3.2 $10^{-19}m^2$ to 1.1 $10^{-19}m^2$ (anisotropy ratio was kept constant). A similar agreement may have been reached by an increase of the stiffness.

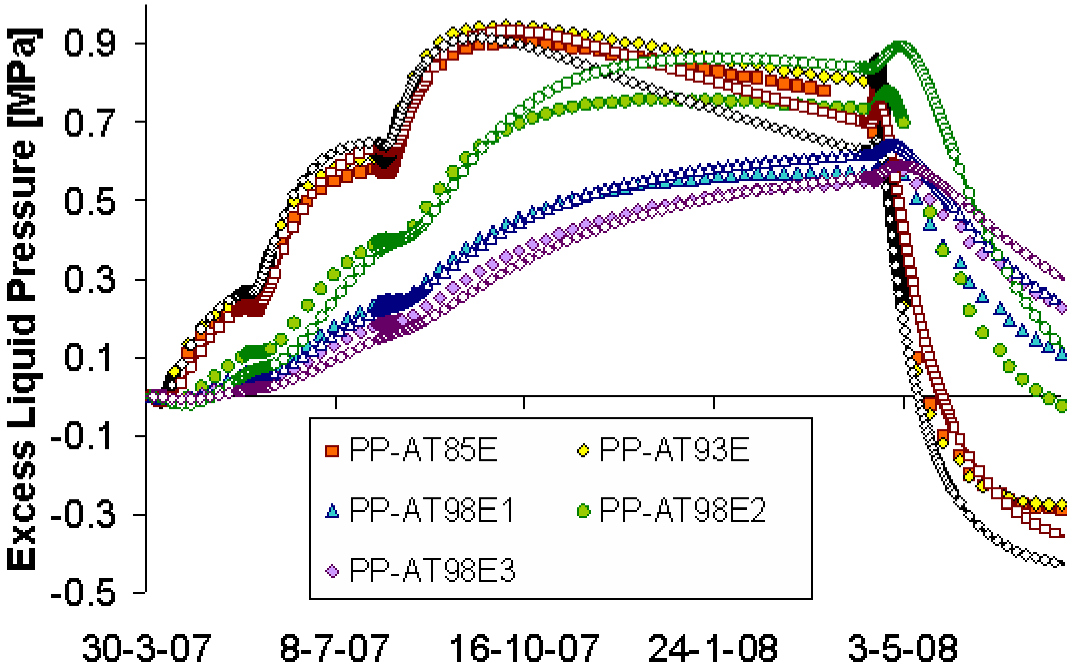

Figure 48: Measured (filled symbols) and simulated (white symbols) excess pore water pressure generated by heating in the ATLAS experiment from 30/03/07 to 26/07/08.

The sensitivity analysis of the permeability allows also for estimating the importance of this parameter. A difference of one order of magnitude between the two extreme cases indicates a non-negligible difference of 0.5MPa and 1.5MPa excess pore pressure.

3.1.4 Conclusions

The numerical modelling of the small-scale in situ experiment ATLAS III has been carried out in two successive steps. First, a benchmark exercise has been defined with three different geometries, based on the experimental set-up. The three configurations enable the participating teams to consider different levels of complexity: (1) a one-dimensional axisymmetric model is easy to handle and gives first insights of the relevant physical phenomena. (2) A 2D axisymmetric geometry helps to reproduce better the experiment, in the radial direction and the axial as well. (3) Finally, as far as anisotropy was suspected to play an important role, a fully 3D model has been also proposed for the benchmark exercise. All the participating teams were let free to select the geometry they want to deal with for this benchmark. Even if the in situ measurements were known at the beginning of the exercise, it was decided that the results of this exercise, provided by the different teams (ULg, EPFL, EURIDICE, CIMNE, NRG), consisted to blind predictions.

During the benchmark exercise, agreement between the predicted results of the different teams has been obtained. Also, first interpretations of predicted results have been made in term of principal stress evolution, followed stress path, pore water pressure and displacement profiles.

Then, in the second phase of simulations, the liberty was given to each team to focus on any specific features of behaviour related to the experimental evidences. The following aspects have been mainly addressed: (i) the contribution of each source of anisotropy (mechanical, hydraulical and thermal) of Boom Clay, (ii) the effect of the non-linear elasticity and the thermo-plasticity, (iii) the research of the best estimate for the anisotropic thermal conductivity and the anisotropic elastic moduli.

To reproduce the temperature modification and the pore pressure changes during the complex heating procedure, it has been noticed that plasticity does not play an important role for this experiment. The conclusion is that this in situ test characterizes mostly the THM behaviour of the undisturbed host rock. That is why most of the modelling uses thermo-elastic constitutive models.

The second aspect clearly evidenced by the experimental and numerical results is that anisotropy is really a key issue in the behaviour of the undisturbed rock. In order to reproduce the temperature field during the experiment, it is necessary to introduce an anisotropic thermal conductivity. The cross-anisotropic elasticity is mandatory for the modelling of the temporary pore water pressure decrease after increasing power and temporary pore water pressure increase after cooling observed in all the five piezometers. Moreover, for a correct prediction of the pore pressure increase, it is necessary to use higher elastic moduli than the one commonly used for numerical modelling of the EDZ.

As a conclusion, through numerical modelling of the in situ test ATLAS III, we have shown that the developed numerical models are able to reproduce the main processes that occur in Boom Clay during the hydro-mechanical hollow cylinder tests.

3.2 In-situ dilatometer tests in Mont Terri

The objective of in situ dilatometer tests modelling in Mont Terri in Timodaz project was to better understand and quantify the thermal impact of heat emitting radioactive waste on Opalinus Clay. These analysis are based on Selfrac and SE-H experiments.

3.2.1 Selfrac Experiment design – Loadings and hydraulic test

Figure 49(a) presents the general design of the Selfrac Experiment (long term dilatometer experiment). From the gallery of the Mont Terri rock laboratory, a new borehole, named BSE-3, is drilled by air circulation. In this borehole, a dilatometer probe is installed and combined with two inflatable packers in a single test string. The dilatometer is positioned at the lowest part of the multi-packer system. Therefore, it is placed into the bottom part of the borehole after installation of the equipment. The dilatometer acts as a normal hydraulic packer element, which can be set with different inflation pressure and isolates hydraulically the bottom section of the borehole from the upper ones.

The pressure in the dilatometer probe is increased stepwise to 5 MPa and hydraulic tests are periodically performed under different dilatometer pressures. Constant rate injection, pulse injection or pulse withdrawal tests are carried out periodically in the deepest interval following a chronological overview. Figure 49(b) summarizes the experiment process. It represents the evolution with time of the dilatometer pressure and the water pressures measured in I1, I2 and I3 intervals.

(a)

(b)

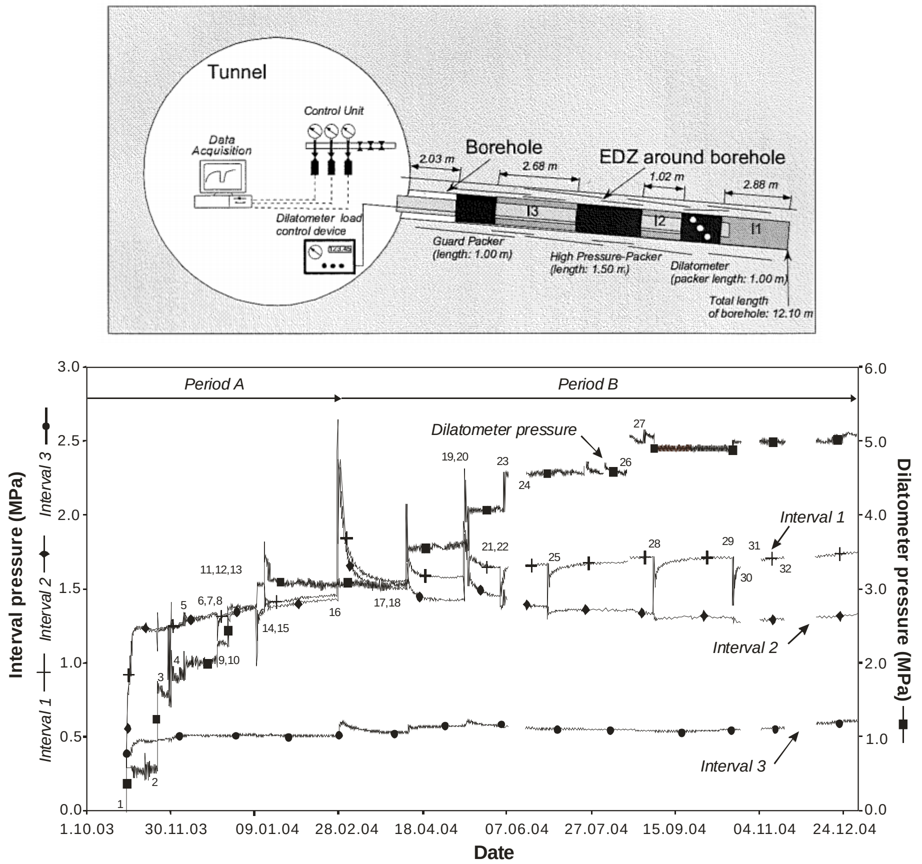

Figure 49: (a) Selfrac Experiment layout (Bülher, 2005); (b) Overview of the project progress (Bülher, 2005)

3.2.2 Selfrac experiment numerical idealisation

Starting from a hydromechanical coupling on which the permeability evolves, the aim of this numerical part is to check the capability of our finite element code to reproduce first qualitatively the experimental results: decrease of the permeability as of function of the dilatometer load. In a second step, we compare also quantitatively the experimental and numerical results in order to evaluate the ability of our model to catch the order of magnitude of the different phenomena. The 2D-axisymetrical finite element model associated with this experiment is presented on Figure 50.

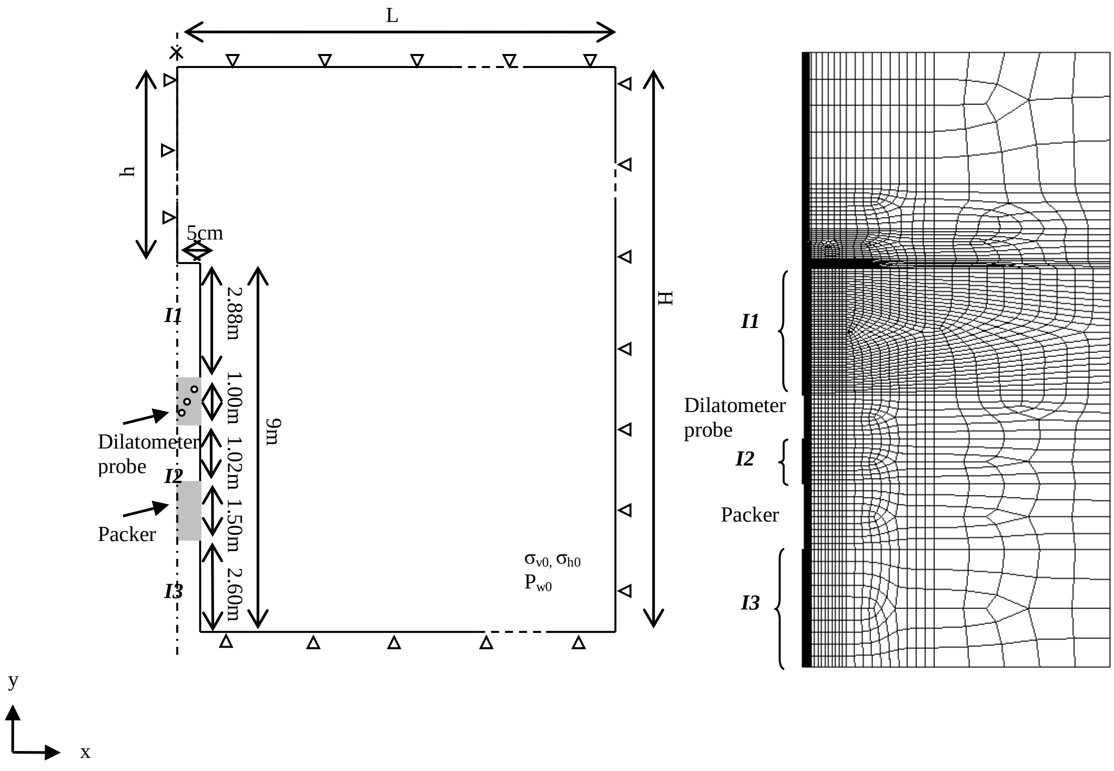

(a) **(b)**

Figure 50: (a) Axisymetric schematic representation of Mont Terri dilatometer test; (b) Associated 2D-axisymetric finite element model – performed with Lagamine code.

The two main steps of the modelling are the excavation and long term dilatometer test.

In **ULg approach**, the Opalinus Clay behaviour is modelled by an elasto-plastic frictional model with a Van Eekelen criterion, which consists of a smoothed Mohr-Coulomb plasticity surface. To take into account of the permeability evolution in the excavation damaged zone, the global permeability tensor of the medium can be evaluated from the tensile part of strain tensor. It corresponds to the sum of the contributions of each n-crack in EDZ as:

$$k_{ij} = \sum_{n=1}^{2} k_n^0 (1 + A_n \varepsilon_n^T)^3 \beta_{ij}(\alpha_n) \quad (0.19)$$

With k_n^0 the initial permeability in the direction of the n-crack (in m²)

$\varepsilon_n^T = \langle \varepsilon_n \rangle = \begin{cases} 0 & if \quad \varepsilon_n \le 0 \\ \varepsilon & if \quad \varepsilon_n > 0 \end{cases}$ with ε_n the strain in the normal direction of the n-crack

A_n the weight coefficient associated with the n-crack properties (without dimension)

$$\beta_{ij}(\alpha_n) = \begin{pmatrix} 1 - \sin^2 \alpha_n & \cos \alpha_n \sin \alpha_n \\ \cos \alpha_n \sin \alpha_n & 1 - \cos^2 \alpha_n \end{pmatrix}_{(e_1, e_2)}$$

α_n the orientation of cracks, which is assumed to follow the orientation of the principle strain directions:

$$\alpha_n = \frac{1}{2} arctg \left(\frac{2\varepsilon_{12}}{\varepsilon_{11} - \varepsilon_{22}} \right) + (n-2)\frac{\pi}{2} \qquad \text{with } n = 1,2$$

The first step of this modelling is the borehole drilling which induces the development of tensile strains within the excavation damaged zone. As a consequence, permeability tensor in EDZ becomes anisotropic as shown on Figure 51.

(a)

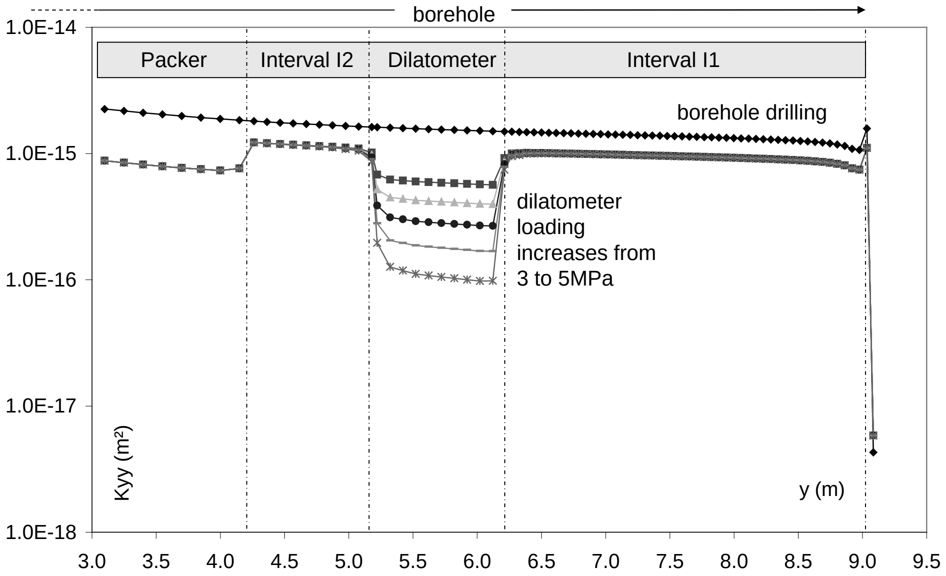

(b)

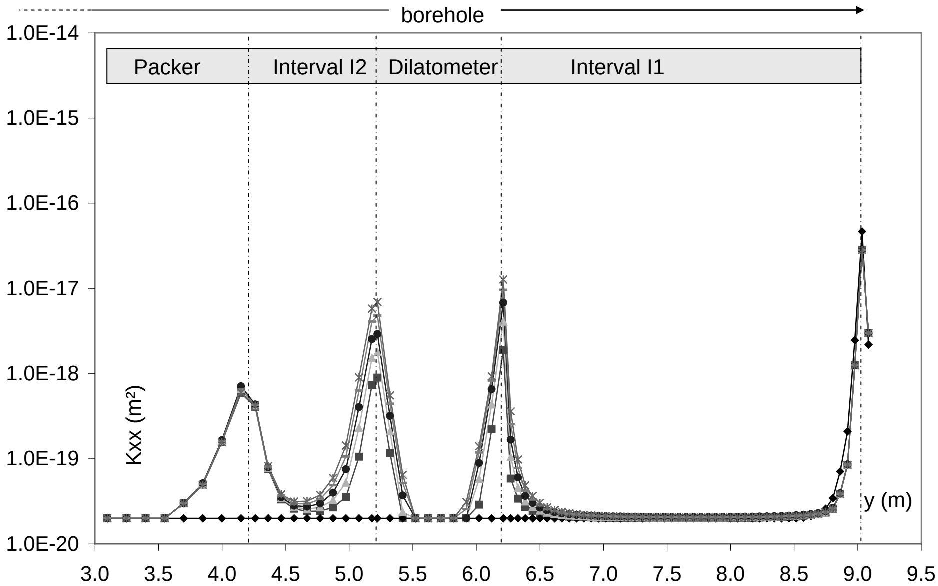

Figure 51: Permeability along the borehole after the borehole drilling and for different dilatometer loads (a) Axial K_{yy} – (b) Radial K_{xx}

During the second step of modelling, the dilatometer and the packer are installed in the borehole and their pressure increases to 3 MPa. This operation has a direct impact on the radial strains and the axial conductivity: the tensile strains decrease and the axial permeability is reduced especially near the dilatometer. The effect of the dilatometer loads can not be noticed in such amplitude in other part of the borehole.

During the third step, hydraulic tests are performed from I1 interval. The first hydraulic test is a constant rate injection test: water is injected at constant flow (83 ml/min) in I1 during several hours. This first hydraulic test is followed by a pulse injection test: 39 ml of water is injected during 35 seconds. The next hydraulic tests are one constant rate injection test and four pulse withdrawal tests. Some numerical results and comparison between experimental data are given on Figure 52.

(a)

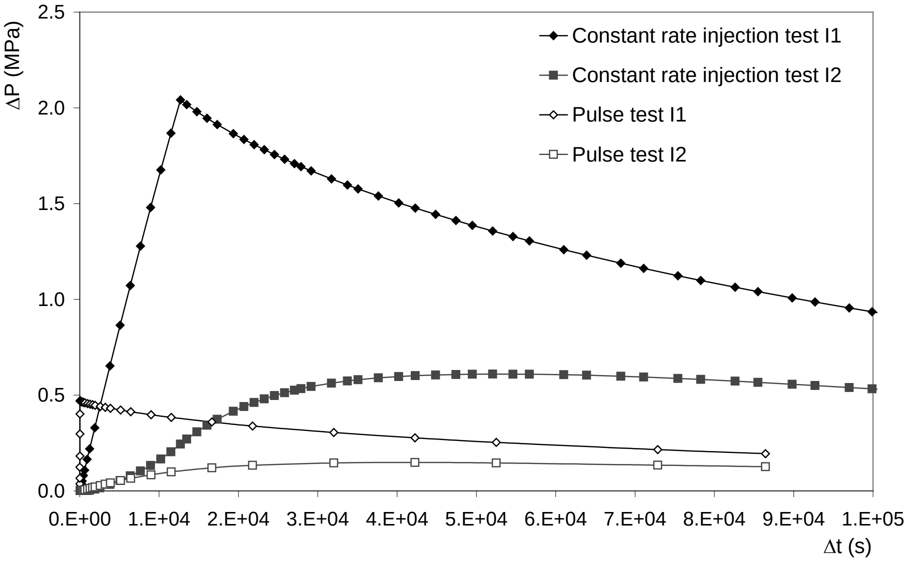

(b)

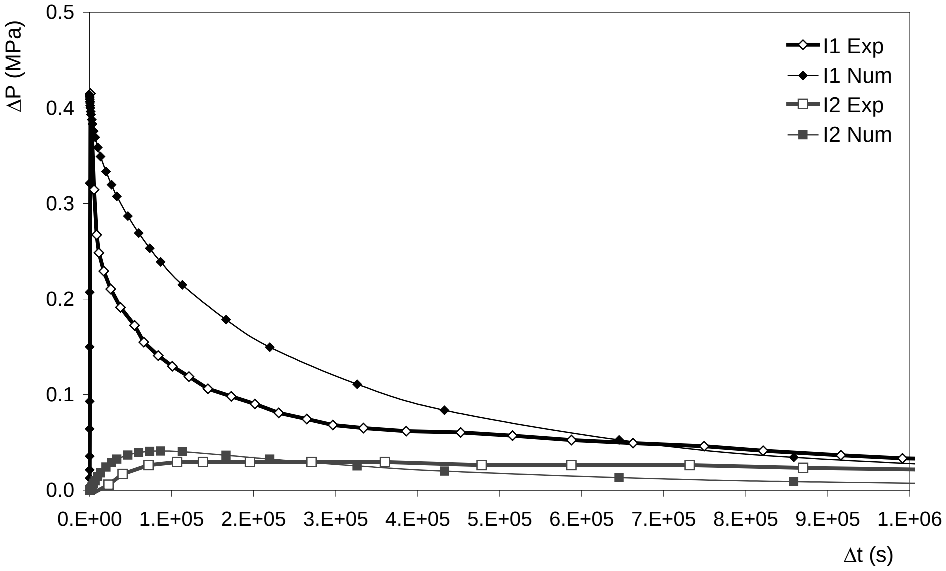

Figure 52: (a) Temporal evolution of the pressure in I1 and I2 intervals during the first constant rate injection test and during the first pulse injection (Pdilatometer = 3 MPa); (b) Comparison between experimental data and numerical results for the last pulse t pulse test ($P_{dilatometer}$ = 5 MPa).

In **CIMNE approach**, constant rate injection tests and pulse tests were modelled in a realistic way, taking the water of the test chamber into account. The understanding of the observed magnitude of the "pulse efficiency", defined as the ratio of the pore water pressure increase in the observation chamber and the pore water pressure decrease in the injection chamber (= $\Delta p_{w2}/\Delta p_{w1}$) with the dilatometer load, was the only objective of the modelling exercise treated by CIMNE. The computations presented by CIMNE were run using Code_Bright, a Finite Element code based on a multi-phase/multi-species approach (Olivella et al., 1994).

During the loading phase of the Selfrac experiment (increasing dilatometer load), three water permeability profiles around the borehole were considered. The pulse efficiency was shown to depend mostly on the permeability value of the rock close to the borehole: the higher the permeability, the less important the pulse magnitude. The amplitude of the water pressure increase was also shown to depend on the shape of the permeability distribution, defining a "possible flow volume".

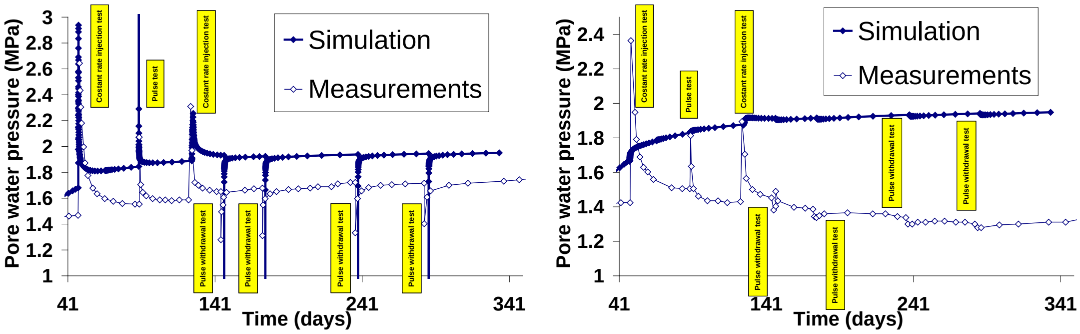

Figure 53 : Comparison of the measured and simulated pore water pressure in the injection chamber (in left) and in the observation chamber (in right) throughout the Selfrac experiment.

In **Itasca approach**, a *PFC2D*/*FLAC3D* coupled model is presented to reproduce the evolution of permeability of Opalinus clay subjected to different hydraulic injection/pumping loadings: a pure hydraulic computation is performed using *FLAC3D* (three-dimension finite difference method) while the mechanical response is calculated using *PFC2D* (two-dimension discrete element method).

Based on the Selfrac long term dilatometer modelling, the constitutive model proposed by Itasca to predict the evolution of the permeability within the EDZ relates the conductivity changes to micro crack formation and local displacement increments. Based on the relative displacement between particles this model is able to predict an anisotropic evolution of the permeability tensor during the excavation and to reproduce the behaviour of indurated clays. An EDZ a few centimetres thick can be identified after the excavation. This area is characterized by a permeability increase of up to two orders of magnitude and a decrease of permeability with the radial distance. The permeability increase is lower than the four orders of magnitude measured on the site. The relatively small permeability variation is due to the small fracture density obtained in the numerical model, compared to the fracture density observed on the site. Moreover, when the dilatometer pressure increases, the axial permeability close to this interval is reduced. This prevents any significant water flow around the dilatometer. Numerical predictions of the pressures in the intervals exhibit discrepancies with the measurements mainly due to 1) an insufficient variation of permeability with strain and 2) a low fracture density after unloading phase. However the model is able to qualitatively predict the main hydro-mechanical variations due according to hydro-mechanical loads.

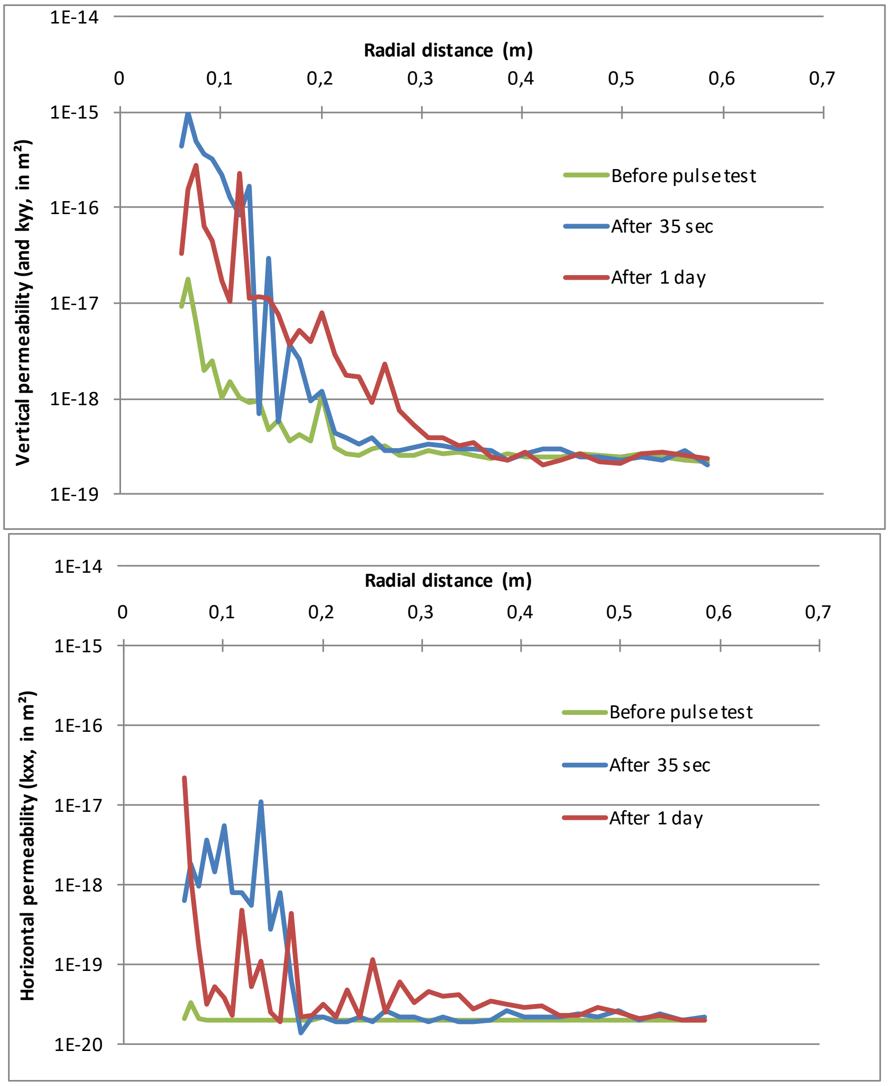

Figure 54 - Mean permeabilities in interval I1, before pulse test (in green), after 35 sec (in blue) and after 1 day (in red): vertical permeability (on the top) and X permeability (on the bottom)

3.2.3 Conclusions of the Selfrac experiment modelling

Based on the Selfrac long term dilatometer modelling, the constitutive model proposed by ULg to predict the evolution of the permeability within the EDZ relates the conductivity changes to the crack aperture in tensile mode. In indurated clay, like Opalinus Clay, EDZ is mainly characterized by extensional fracture. Using a hypothesis on the link between crack opening and the principal strain tensor, the model is able to predict an anisotropic evolution of the permeability tensor during the excavation and permits to reproduce behaviours of indurated clays.

An EDZ of few centimetres behind the borehole can be identified after the excavation. In this area, a high fracture density exists and is characterized by permeability increases of up to several orders of magnitude. This fracture density decreases with the radial distance. Moreover, when dilatometer pressure increases, the axial permeability decreases. No significant water flow can evolve in EDZ behind the dilatometer.

The comparisons between numerical predictions and measurements of the pressures in the intervals exhibit a good agreement and confirm that ULg model is able to catch the main hydro-mechanical processes occurring within the EDZ in indurated clay. Numerical tendencies in terms of pore water pressure are correct, even if for low dilatometer pressure, water pressure can be overestimated in front of the dilatometer and underestimated behind the dilatometer probe. These differences are partly due to assumptions in the finite element modelling and in the permeability tensor definition. To reduce them, further improvements could be imagined in this approach by considering anisotropic properties and in situ conditions of Opalinus clay through a 3D model or by another description of cracking through the development of a homogenisation model based on micromechanical concepts.

3.3 SE-H Timodaz thermo-dilatometer experiment

Selfrac experiment has shown that, at constant temperature, more the packer pressure increases, more the water flow in EDZ decreases due to the closure of EDZ micro-cracks. Compare to Selfrac experiment, SE-H thermo dilatometer test aimed to see if temperature has an additional effect on micro-crack closure and the on the EDZ hydraulic conductivity in Opalinus clay.

SE-H experiment is a thermo-hydro-mechanical experiment realised in the normal direction to the gallery 98 of the Mont Terri rock laboratory where initial stress state has been measured as σ_{0v} = 6.5MPa, σ_{0H} = 4.5MPa (normal to SE-H borehole direction), σ_{0h} = 2.2MPa (parallel to SE-H borehole direction). Initial pore pressure and temperature are equal to: p_{w0} = 2MPa and T_0 = 15°C = 288°K.

This experiment is composed of a main borehole (BSE-H2: 5.3m long and 76mm of diameter), drilled by air circulation from the gallery 98, which combines two inflated packers (P1 and P2) with one system of water circulation, which permit to impose pressure and temperature in the borehole (Figure 55). The effects of pressure and temperature loadings are measured by pore pressure and temperature sensors supposed to be placed at 70cm from BSE-H2 in two thin boreholes BSE-H3 and BSE-H4.

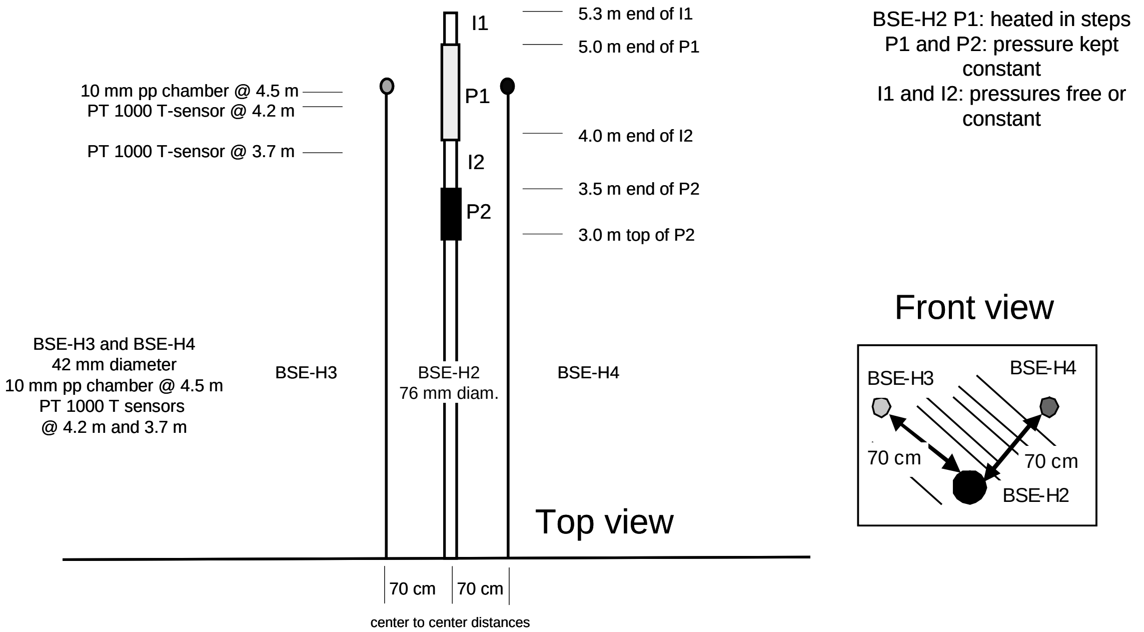

Figure 55: SE-H experiment: initial packer system setup

Hydraulic conductivity in EDZ is tested by some hydro-tests, which consist on constant rate injection tests performed from I2 interval (which is saturated). Injections provide water overpressures and water flows along micro-cracks through EDZ. The effects of these overpressures are then measured by pressure sensors in I1 interval (also saturated) and in BSE-H3 and BSE-H4 boreholes. Temperature is directly imposed in the BSE-H2 borehole by hot water circulation from I1 to P2 and controlled by sensors in each component of the borehole (in I1, P1, I2 and P2).

3.3.1 SE-H experiment numerical idealisation

Previous definition of experimental device clearly shows that the problem is 3-dimensional: the temperature and pressure vary in a direction normal to the borehole, towards the bedding; the consequences of thermal loadings are tested on hydraulic conductivity along the borehole, in EDZ. However, experimental results show that hydraulic conductivity seems to not radically change with packer loading and thermal variations. Then, in a first approximation, we have decided to simplify the numerical model by considering only a 2D plane strain modelling, normal to the borehole (like the front view of the schematic representation of the problem proposed on Figure 55).

The soil behaviour modelling needs a thermo-hydro-mechanical anisotropic coupling. An elastic orthotropic law is used. An anisotropic permeability tensor and thermal conductivity are initially defined and oriented along the previous anisotropic angle.

Three cases have been studied: Case 0 (modelling in the experiment conditions and with reference parameters defined from literature), Case 1 (modelling in the experiment conditions and with parameter calibrations to catch experimental results) and Case 2 (as the results of calibration give some non-physical parameters, investigations are made on thermal loading based in Packer 2 temperature evolution).

Figure 56, related to Case 2, shows that with a smaller thermal loading, like the one measured in packer P2, water pressure and temperature fields can be better captured with realistic parameters. Heating jump are well reproduced and water pressure evolution is well estimated (the steps due to temperature increase as well as the corresponding relaxations of water pressure). As in the experiment, we can observe that soil anisotropy provides an anisotropic response with a delayed T-response normal to bedding (BSE-H4). Unfortunately, the observed delayed P-response parallel to bedding (BSE-H3) is not obtained numerically. We can also notice that more temperature loading increases, more thermal evolutions and water pressure evolutions diverge from the measured ones: measured thermal effects are less important than the calculated ones; measured water pressure variations are smaller than the calculated ones. This could be the consequence of our 2D modelling which does not permit to well characterize 3D anisotropy effects in the thermal diffusion in soil and could also explain why the delayed P-response parallel to bedding (BSE-H3) is not obtained numerically. It could also be due to temperature field which is not exactly the one imposed to field because of dilatometer membrane isolation.

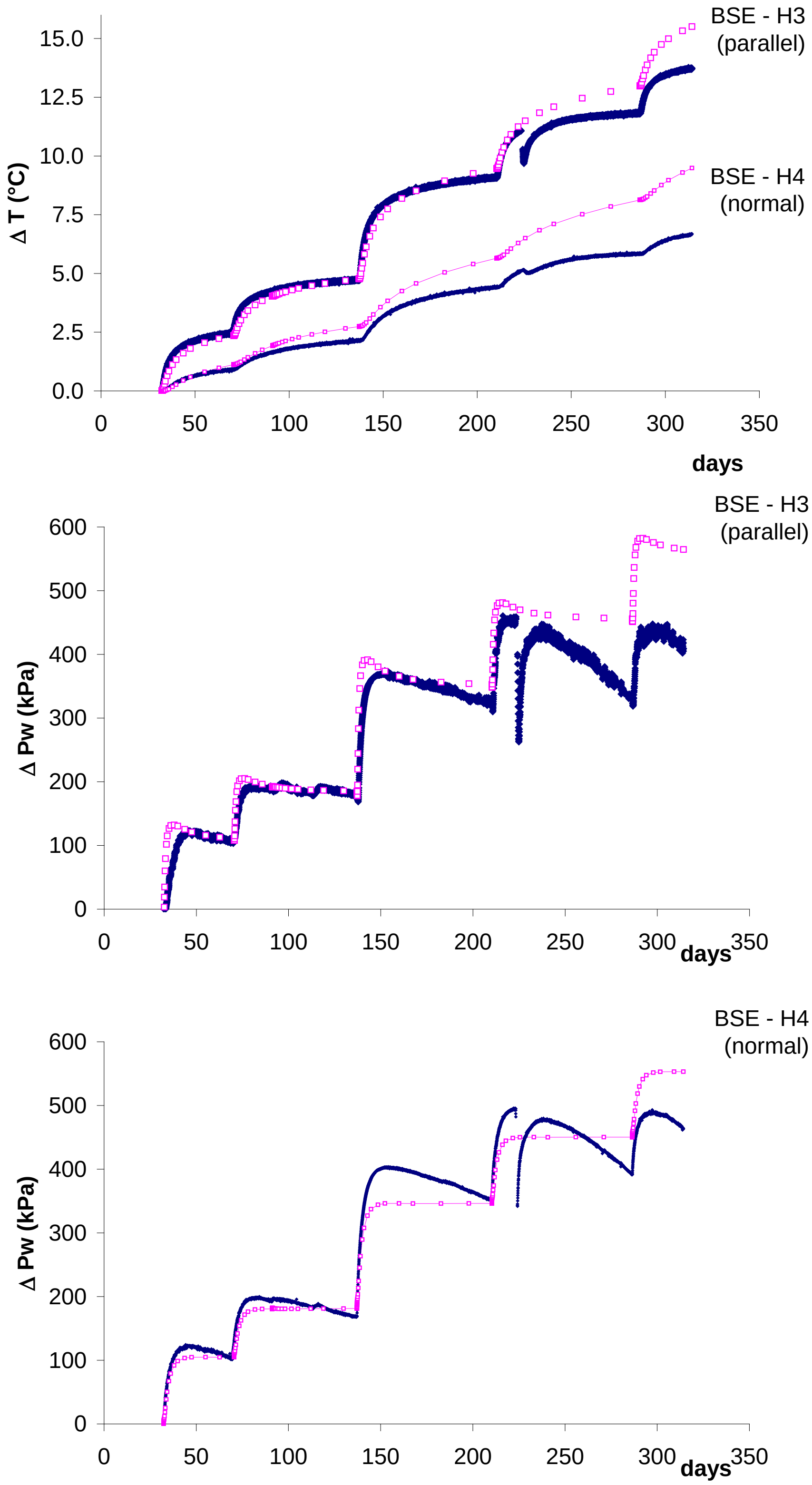

Figure 56: Temperature and water pressure variations in time for the borehole BSE-H3 and BSE-H4 (in the direction parallel and normal to bedding respectively) following conditions described in Case 2 and 2bis (pink squares) compared to in situ measurements (blue diamonds)

3.3.2 Conclusions on SE-H experiment modelling

The analysis of SE-H modelling through three these different cases has shown that to catch temperature and water pressure evolution of SE-H experiment with a 2D plane strain model, it is not only necessary to calibrate soil parameters, thermal loading in packer needs also to be reduced. This is due to the 2D modelling which does not permit to characterize the thermal diffusivity in the three directions of soil and more particularly the effect of "fresh" temperatures coming from I2 and P2; but also to an isolation of the packer membrane which reduce the effect of temperature on soil.

However, during the summer 2010, SE-H Experiment was finished and its geometry checked. It was observed that the front view of the packer system setup of SE-H experiment does not correspond to the expected one (the two observation boreholes are not at 70 cm from the heater but at 60 and 120 cm from the heater). This error in the experiment design casts doubt on all the analysis.

4 Large scale in situ test PRACLAY

4.1 Experiment description

Praclay is an experiment in progress within the Boom underground laboratory at a depth of some 200m, in a poorly indurated Boom Clay layer (Figure 57). The Praclay project was initiated in the middle of the 90'ties and intends to achieve several experiments, including the drilling of the connecting gallery, some on surface tests, and the Praclay gallery project, which is concerned in the Timodaz project.

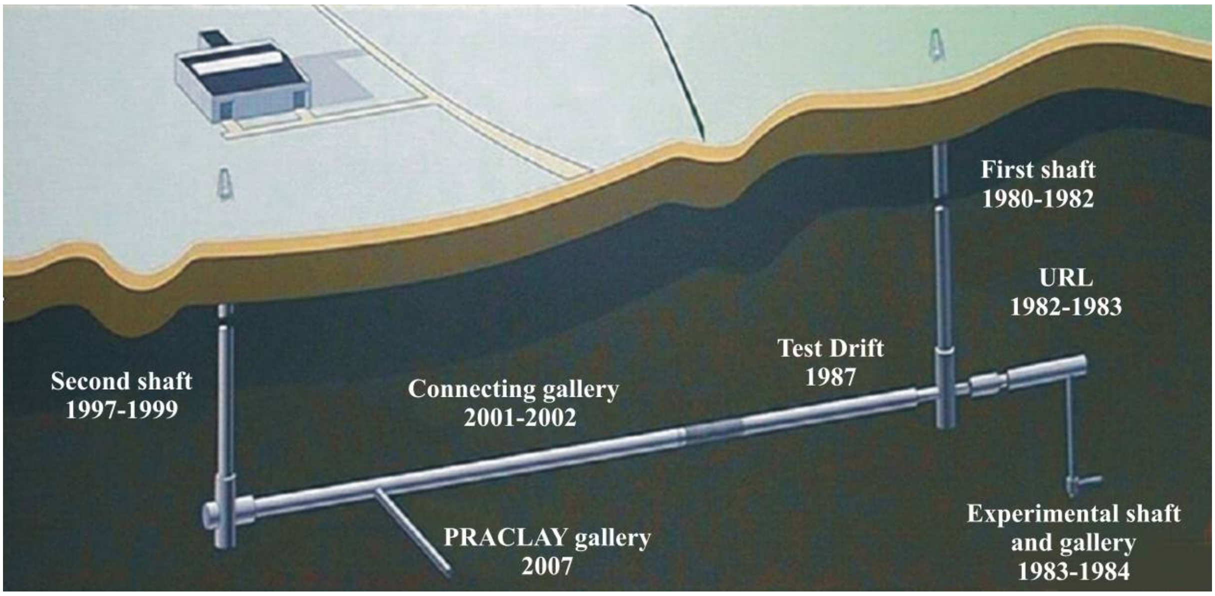

Figure 57: History and layout of the underground research facility HADES

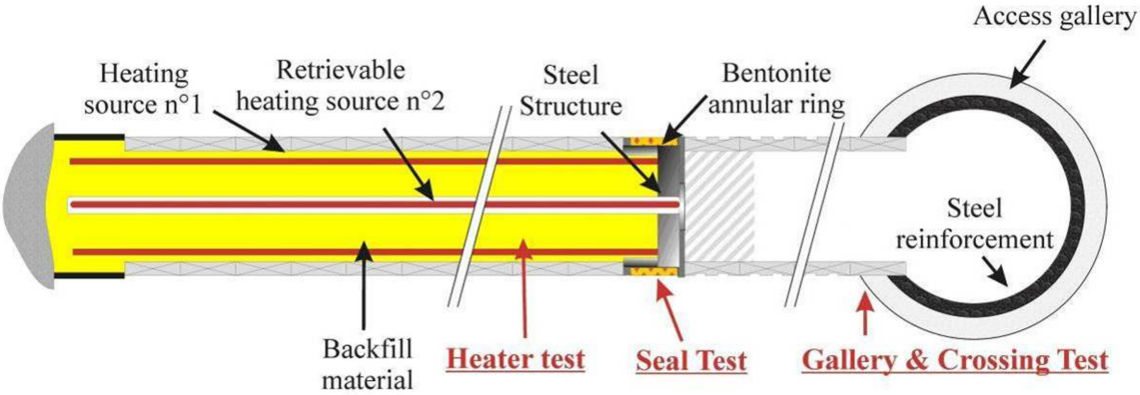

Figure 58: The PRACLAY in-situ experiment comprises three tests: the "Gallery&Crossing Test", the "Seal Test" and the "Heater Test"

The large In-Situ Experiment (Figure 58) comprises three tests:

1. the Gallery and Crossing Test further examining and demonstrating the construction of an underground repository by industrial method and examining the feasibility to construct a crossing between galleries;

2. the Seal Test examining the feasibility of hydraulically sealing the heated part of the PRACLAY gallery from the rest of the underground;

3. the Heater Test studying the response of the Boom Clay to a thermal impact.

The same excavation technique and type of lining as applied for the construction of the Connecting Gallery were selected for the PRACLAY gallery: excavating by an open-face tunnelling machine and installing a concrete wedge block lining. The design of the lining had to take into account a geotechnical loading due to the pressure exerted by the clay massif on the lining and a thermal loading due to the increased stresses in and on the lining during the Heater Test. The diameter of the PRACLAY gallery is set at 2.50 m. A reinforcement ring is placed in the Connecting Gallery prior to the excavation works to assure the stability of the lining of the Connecting Gallery.

The underground works started on 01.10.2007 with the cutting of the lining of the Connecting Gallery, and the construction of the PRACLAY gallery was successfully completed in 2007. A hydraulic seal was successfully installed in the PRACLAY gallery in 2010. The installation is part of the PRACLAY In-Situ Experiment and its main purpose is the creation of an undrained hydraulic boundary at the intersection between the heated part of the PRACLAY gallery and the non-heated part. Such an undrained boundary is required to achieve the most penalizing conditions that are reasonably achievable during the Heater Test.

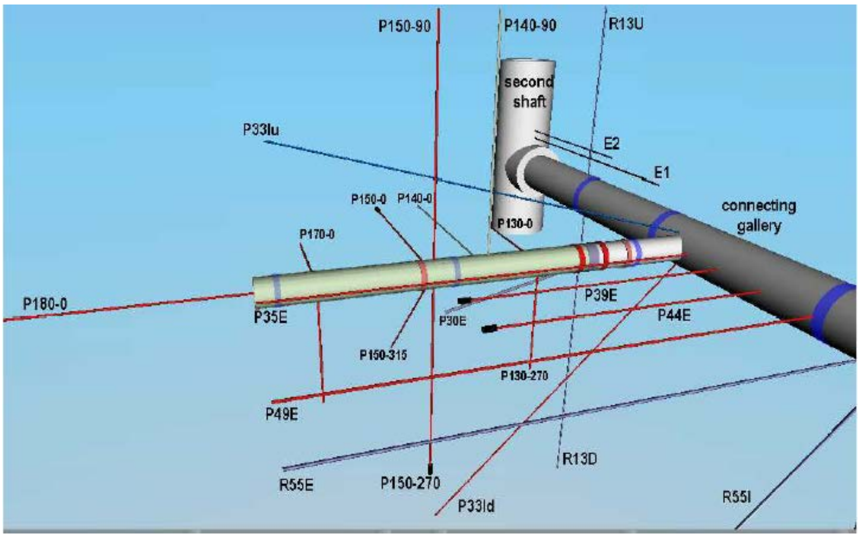

Figure 59: Lay-out of the instrumented boreholes around the PRACLAY gallery

The bentonite placed in an annular ring against the Boom Clay has to exert a swelling pressure of ca. 5 MPa against the Boom Clay to locally reduce the hydraulic conductivity of the Boom Clay around the seal and in that way create an undrained hydraulic boundary. It was decided to use MX80 bentonite compacted into bentonite blocks.

The last phase in the installation of the PRACLAY In-Situ Experiment will be accomplished in 2010 by the installation of the heating system and backfill material. The requirement for the heating system is that it has to impose a constant temperature of 80°C in the clay at the gallery extrados. The heater consists of a primary heater close to the gallery intrados and a secondary heater inside a central tube (Figure 58). Both heaters consist of electrical heaters.

The Figure 59 below gives an overview of the instrumentation program including temperature, pore water, total stresses and displacements measurements as well as the follow-up of the chemical evolution in the Boom Clay around the test.

4.2 Experiment idealisation

The main idea of the reported simulations is to reproduce the excavation of the PRACLAY gallery and the heating phase of the PRACLAY experiment with a coupled thermo-hydro-mechanical model. This modelling may be considered as a plane strain two-dimensional problem (this simple geometry allows taking into account anisotropy in 2D), a two-dimensional problem in axisymetric condition or a three dimensional problem. This last geometry allows taking into account the effect of the anisotropy of the clay for all the processes. Figure 4 illustrates the 2D plane strain model. The inner radius is equal to 0.95 m, the thickness of the liner is equal to 30 cm as seen in Figure 60.

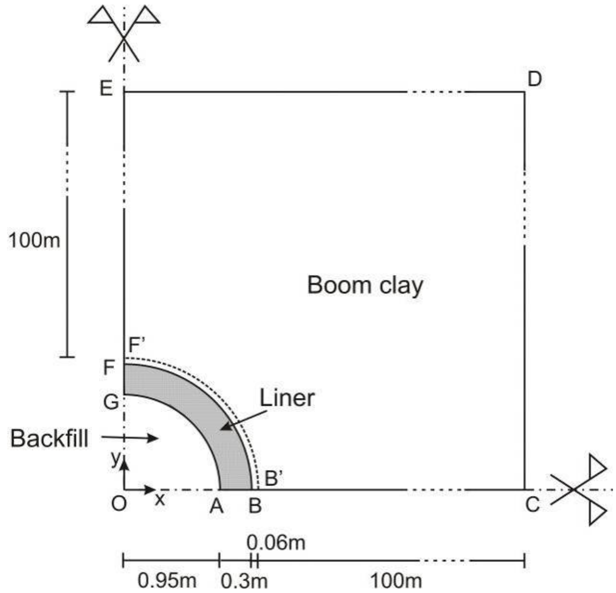

Figure 60: Schematic representation of the 2D plane strain modelling

The geometry of the modelling for the bi-dimensional axisymetric conditions is based on the geometry of the PRACLAY gallery, provided in Figure 61. The geometry of the 3D modelling is inspired of the plane strain and axisymetric cases (Figure 62).

Seven different materials are involved in the construction of the gallery. Most of the liner rings are made of concrete elements, but some steel components are also used for the seal and, at the end of the gallery, for the lost shield and the stiffened steel end.

The clay is initially considered as homogeneous and isotropic. It is supposed to be fully saturated. Initial state of stresses is anisotropic, unless for the axisymetric modelling.

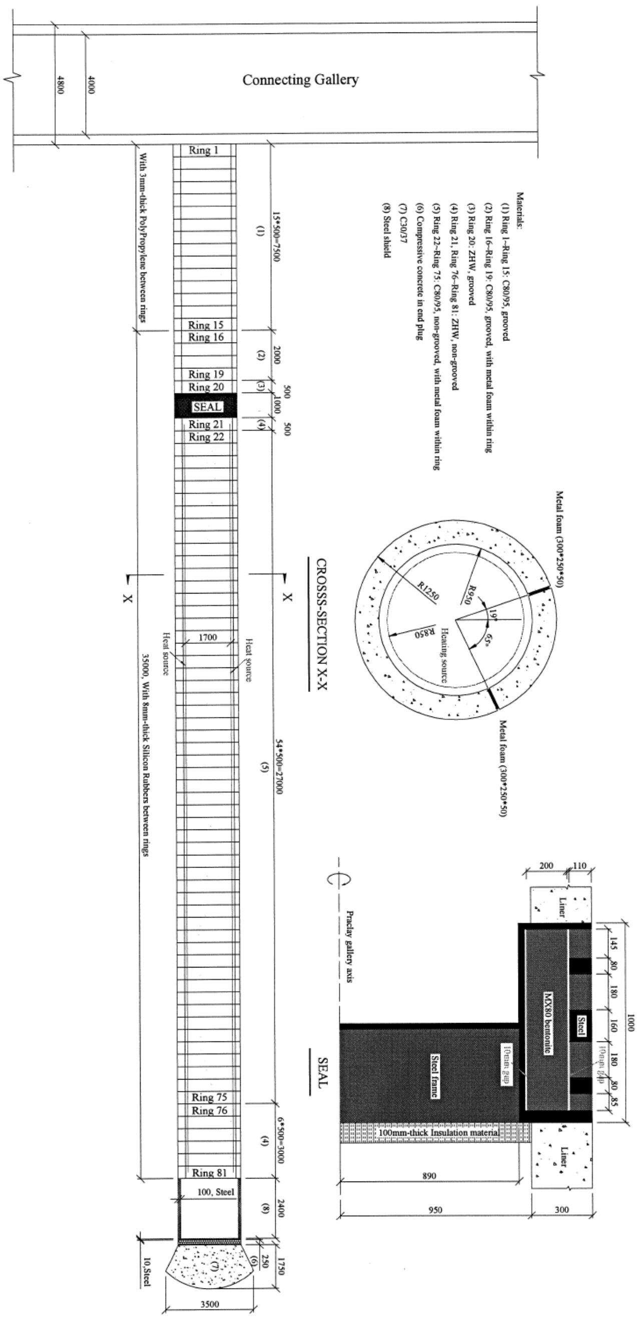

Figure 61: Schematic representation of the PRACLAY experiment

In the concrete liner, the initial conditions assume that the concrete is saturated at a temperature corresponding to the one of the host formation. The liner is composed of concrete C80/95. Due to joints, its permeability is taken 10 times greater than the clay permeability. The friction coefficient between the ring and the host clay depends on the external geometry of the concrete liner: some of them are grooved. The liner is supposed to be put after a convergence of 0.06 m.

The backfill material, constituted of sand with a 40% porosity and saturated in water, was not taken into account and not modelled in that benchmark for sake of simplicity.

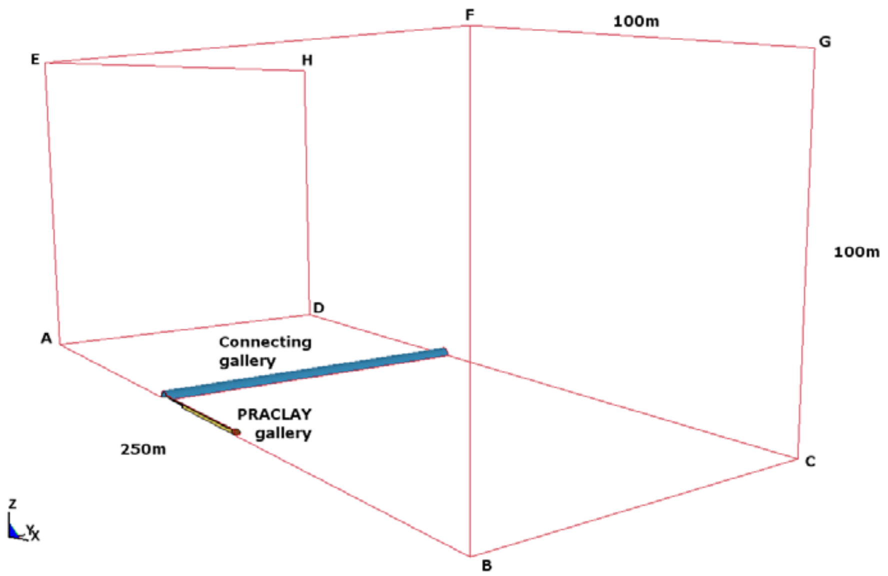

Figure 62: 3D model extent

The seal element is modelled with a steel ring (with the same thickness as the concrete one), without representing explicitly the bentonite. However, the action of the bentonite is modelled by imposing a total stress history corresponding to the swelling pressure and considering impervious condition at the steel extrados.

The modelling first consists in the excavation of the gallery and, in a second step, a thermal loading is applied at the extrados of the liner:

- Phase 1: Duration: 20 days: Excavation of the gallery; Temperature fixed at initial value on the whole domain.
- Phase 2: Duration: 2.5 years: Waiting phase: pore pressure fixed at 100 kPa on the liner intrados; Temperature fixed at initial value on the whole domain.
- Phase 3: Duration: 1 year: Installation of the seal (total stress increase, impervious boundary); Waiting phase: pore pressure fixed at 100 kPa on the liner intrados; Temperature fixed at initial value on the whole domain.
- Phase 4: Duration: 6 months. Heater phase: temperature linearly increasing from initial value to 85°C at the intrados of the liner; Water undrained conditions at the liner intrados in the part of the gallery after the seal. The hydraulic conditions remain the same as the ones in the previous phases, in the part of the gallery between the connecting gallery and the seal.
- Phase 5: Duration: 10 years. Stabilised heater phase: temperature fixed to 85°C at the intrados of the liner; Water undrained conditions at the liner intrados in the part of the gallery after the seal. The hydraulic conditions remain the same as the ones in the previous phases, in the part of the gallery between the connecting gallery and the seal.

The actual heater system is constituted of a pipes network with heat water flow inside; it is located 10 cm inside the intrados of the liner and imposes a temperature, as constant as possible, of about 80°C at the extrados gallery wall. This complex system is idealised simply by imposing an increase of the temperature directly at the intrados of the liner.

4.3 Results: Comparison of 2D and 3D models

Results were proposed by ULg, Euridice, CIMNE and NRG for 2D plane strain simulations, by EPFL, ULg, Euridice and CIMNE for axisymetric simulations and by ULg and CIMNE for 3D simulations.

4.3.1 Pore water pressure

The comparison of the p_w profiles obtained using the 3 different approaches leads to two main conclusions summarized on the following figures:

- At the end of the gallery excavation (Figure 63), the anisotropy of the initial stresses implies a higher p_w along the horizontal profile. Both 2D plane strain and 3D models include this anisotropy and they provide very similar results: the same difference between horizontal and vertical p_w profiles and the same overpressure (peak) along the horizontal profile (the same maximum value as well as the same location). With the 2D axisymetric model, which does not take into account the anisotropic initial stresses, the p_w profile is in-between.
- At the end of the experiment (Figure 64), the difference between the horizontal and vertical profiles is not so large anymore, as predicted by those models including this anisotropy, i.e. 2D plane strain and 3D models. The main difference is now between the 2D plane strain model that predicts a maximum p_w at the wall (about 2.7 MPa) and both 2D axisymetric and 3D models that agree on a maximum p_w around 2.5 MPa and located at about 9 to 10 m from the gallery axis.

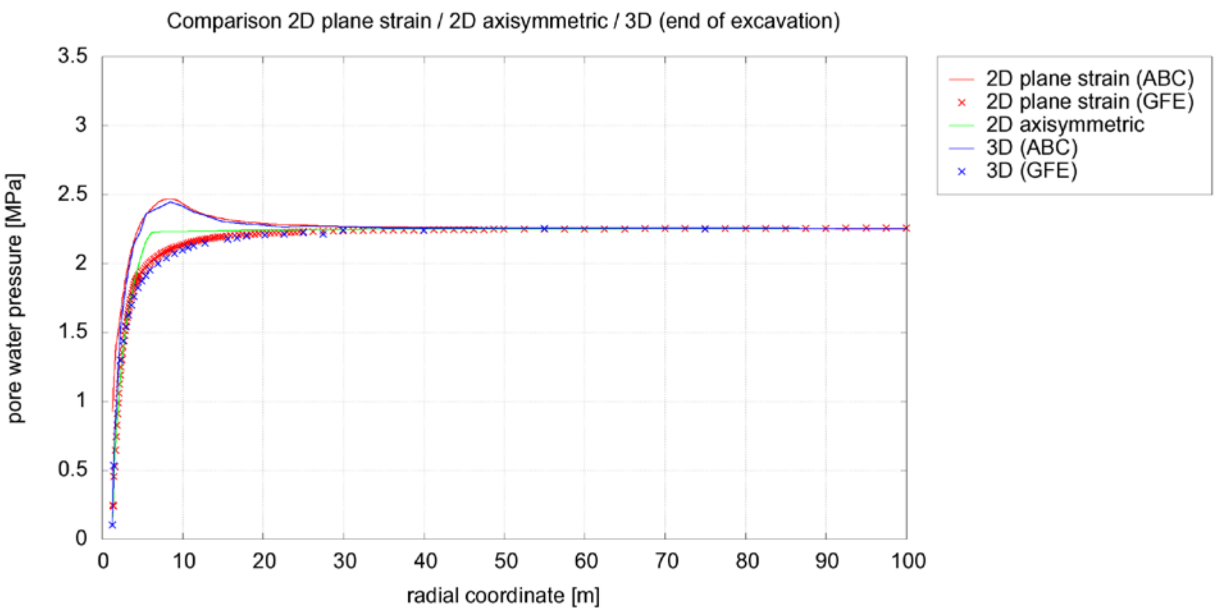

Figure 63: Comparison of the p_w horizontal and vertical profiles at the end of the excavation with the 2D plane strain, 2D axisymetric and 3D models (using BC2 in all models)

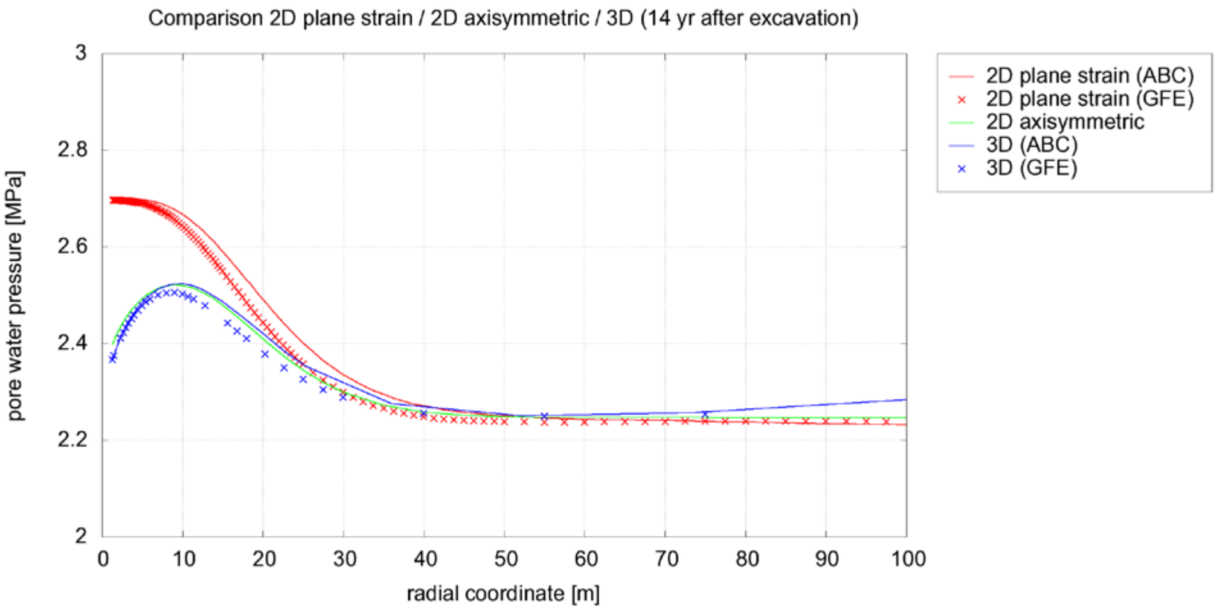

Figure 64: Comparison of the p_w horizontal and vertical profiles at the end of the experiment with the 2D plane strain, 2D axisymetric and 3D models (using BC2 in all models)

Hence, the 3D model is more complete than 2D models and it should indicate the most realistic results among the three approaches. In the short term results, the 2D plane strain model is in good agreement with the 3D model (since the stress anisotropy could be introduced).
In the long term results, the effect of anisotropy of the initial stresses is not as important as just after excavation. The 2D axisymetric and 3 models are therefore in good agreement, since the diffusion of p_w along the axial direction is allowed in the 2D axisymetric model and not in the 2D plane strain one.
Nevertheless, we should keep in mind that no other anisotropy but initial stresses is included in the 3D model. Otherwise, if some other anisotropic properties were taken into account (such as intrinsic permeability or thermal conductivity), we would expect to see a difference between the 2D axisymetric and the 3D approaches.

4.3.2 Temperature

The temperature profiles in all the models are very close, as illustrated in Figure 65, and no anisotropy can be observed since thermal properties are isotropic in all models (hence vertical and horizontal profiles are superposed in the figure).
The main difference is observed when comparing the 2D plane strain model with the two other models. Since there is no heat diffusion in the direction of the gallery axis in this model, the temperature is a little bit higher than the temperature predicted by the 2D axisymetric and 3D model, that are in very good agreement on this. The gap between the different approaches is maximum between 10 and 20 m and it reaches a few degrees (about 2°C).

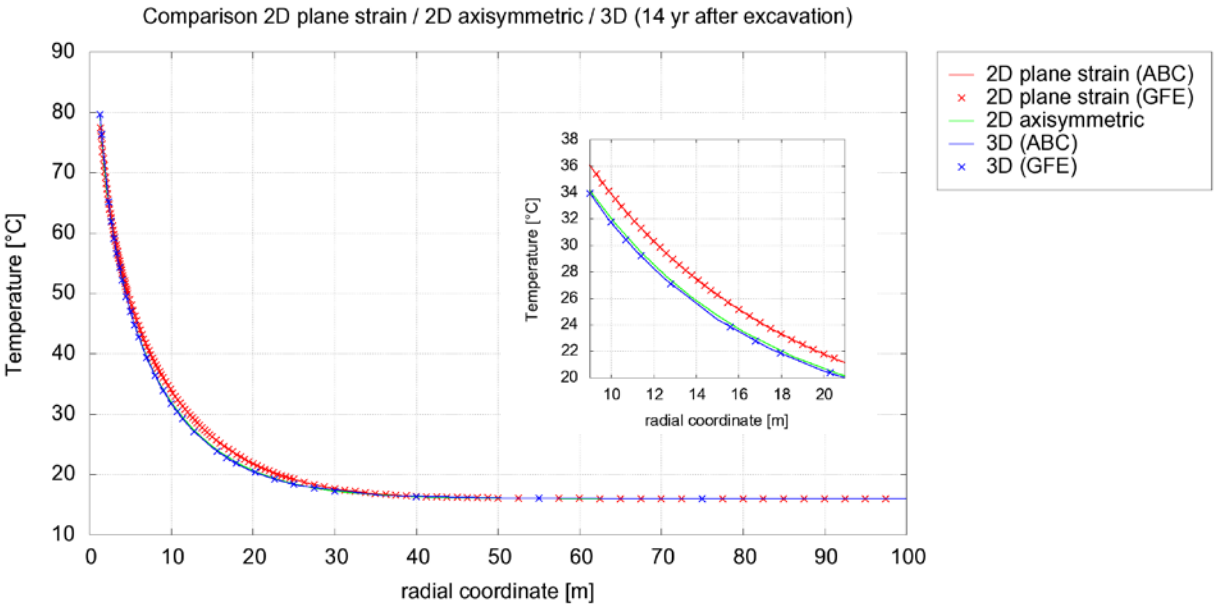

Figure 65: Comparison of the horizontal and vertical temperature profiles at the end of the experiment with the 2D plane strain, 2D axisymmetric and 3D models (using BC2 in all models)

4.3.3 Radial displacement

The comparison of the radial displacement at the end of the excavation using the different models (cf. Figure 66) is very similar to the analysis of the p_w profiles. The 2D plane strain and 3D models give the same different curves along the horizontal and vertical profiles and the 2D axisymetric model is again in-between. The reason is still a question of anisotropic initial stresses.

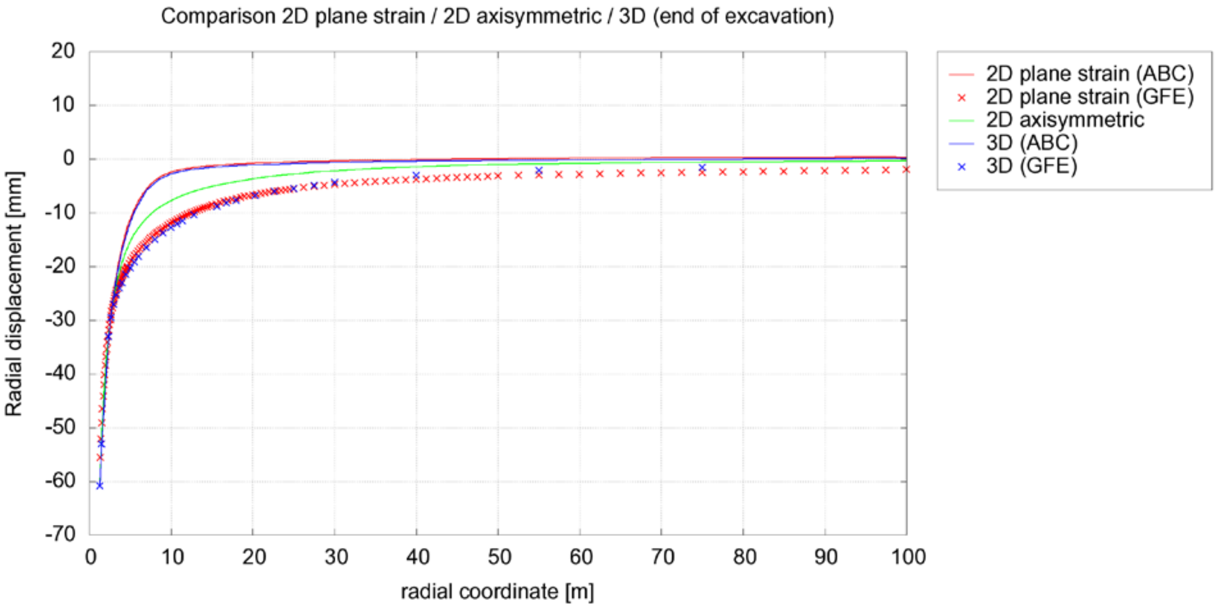

Figure 66: Comparison of the radial displacement along horizontal and vertical profiles at the end of the excavation with the 2D plane strain, 2D axisymmetric and 3D models (using BC2 in all models)

Observing the same profiles at the end of the experiment (Figure 67) is now different from the profiles of p_w 14 years after the excavation of the gallery: the agreement between 2D axisymetric and 3D models is not as good as in the Figure 64. The reason comes from the fact that the radial displacement is a cumulated value during all the experiment and the history in the 2D axisymetric and 3D models is not exactly the same, more especially in terms of plasticity as described in the next section. Even though similar pressure levels (and stress levels) can be observed at the end of the experiment in the two approaches (as in Figure 64), the plastic strain might be very different and so the corresponding displacement profiles might do (Figure 67).

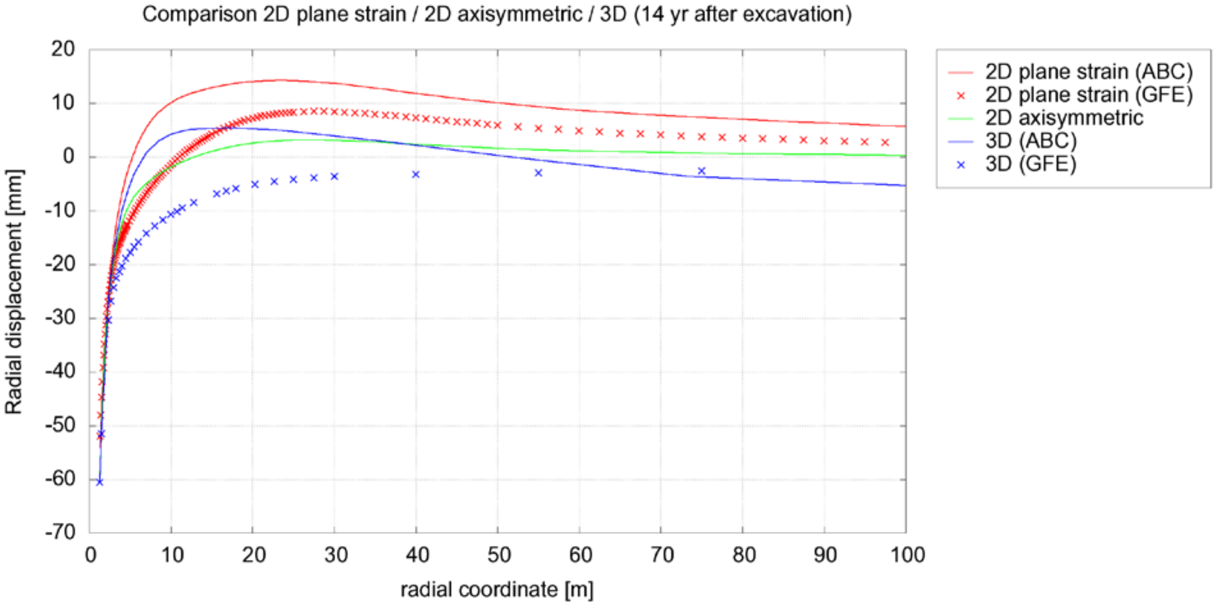

Figure 67: Comparison of the radial displacement along horizontal and vertical profiles at the end of the experiment with the 2D plane strain, 2D axisymetric and 3D models (using BC2 in all models)

4.3.4 Effective stress path

The main difference between the models comes from the initial stress state. As the initial effective stresses are isotropic in the 2D axisymetric model, the stress path start from another initial point in the invariants space:

- in the 2D plane strain and 3D models:

$$I_{1,ini} = -5.4\,\text{MPa} \quad \text{and} \quad I_{2,ini} = 0.675\,\text{MPa}$$

- in the 2D axisymetric model:

$$I_{1,ini} = -6.75\,\text{MPa} \quad \text{and} \quad I_{2,ini} = 0\,\text{MPa}$$

Considering the initial drained friction angle $\phi_{ini} = 5°$, the stress state reaches more quickly the plastic domain in the 2D plane strain and 3D models than in the 2D axisymetric model. As a consequence, the sensor P42E remains in the elastic domain according to the 2D axisymetric model, while it enters the plastic domain according the two other models, as shown in theFigure 70.

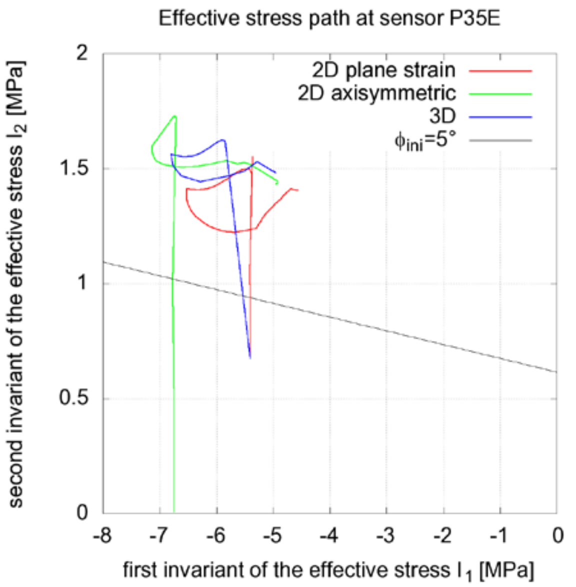

Figure 68: Stress path in the I_1-I_2 invariants space at sensor P35E

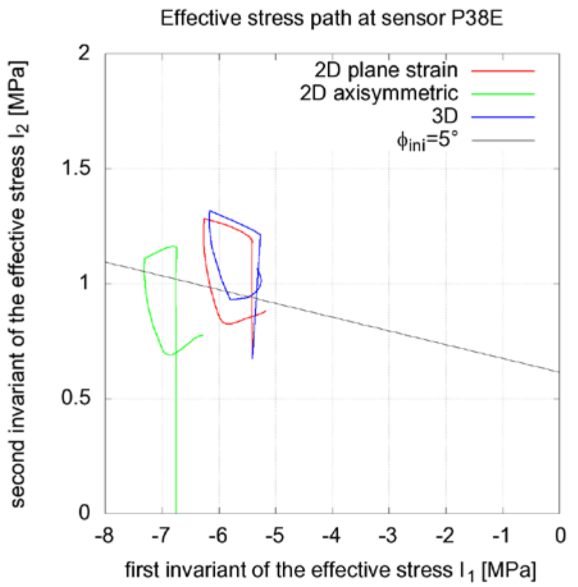

Figure 69: Stress path in the I_1-I_2 invariants space at sensor P38E

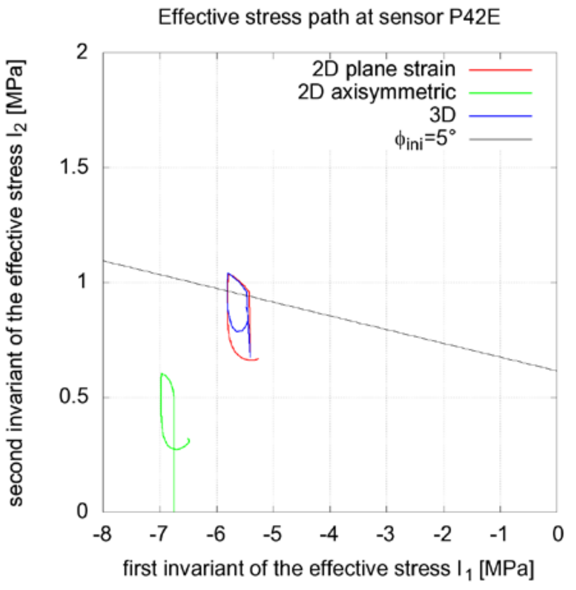

Figure 70: Stress path in the I1-I2 invariants space at sensor P42E

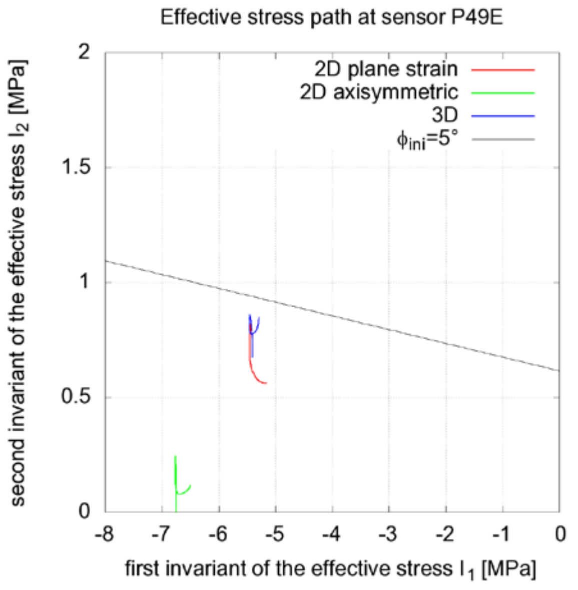

Figure 71: Stress path in the I_1-I_2 invariants space at sensor P49E

For all four sensors, the 2D plane strain and the 3D models are in relatively good agreement (cf. Figure 68 to Figure 71), the main drawback of the 3D model being the lack of a complete path during the excavation because of numerical reasons.

4.3.5 Plastic zone extent

To illustrate the extent of the plastic zone, the figures below represent the contour levels of the Coulomb's friction angle ϕ at the end of the excavation. The initial value is 5°, represented in white in this figure. Due to plastic hardening, ϕ increases up to those colorized values in the scale, i.e. from blue (5°-6°) to red (up to 16°).
The 2D axisymmetric model predicts a less extended plastic zone, the thickness of which being 2.6 m (cf. Figure 72).

The 2D plane strain and 3D models are in good agreement, predicting a plastic zone extending up to 3 m along the vertical direction and about 3 times deeper in the horizontal direction, up to 9 m - 11 m (cf. Figure 73 in 2D plane strain, and Figure 74 in 3D).

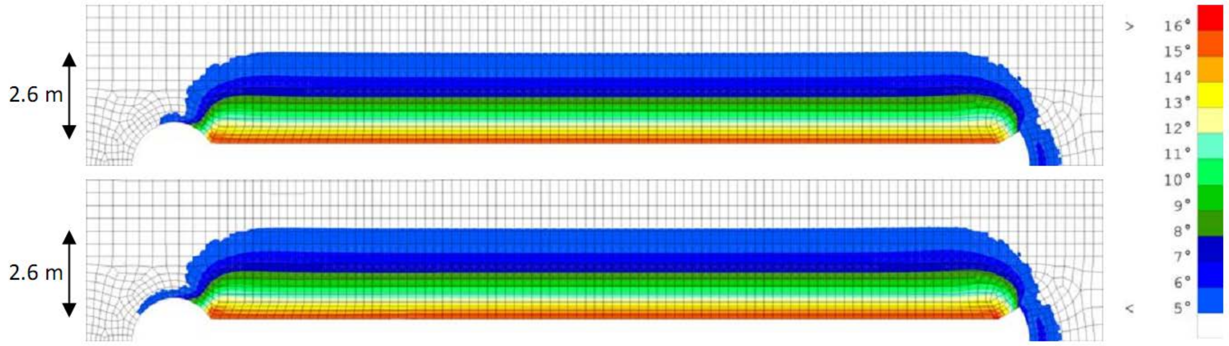

Figure 72: 2D axisymmetric model - Actualized ("hardened") Coulomb's friction angle at the end of the excavation (above) and at the end of the heater experiment (below). Initial value is 5° (in white)

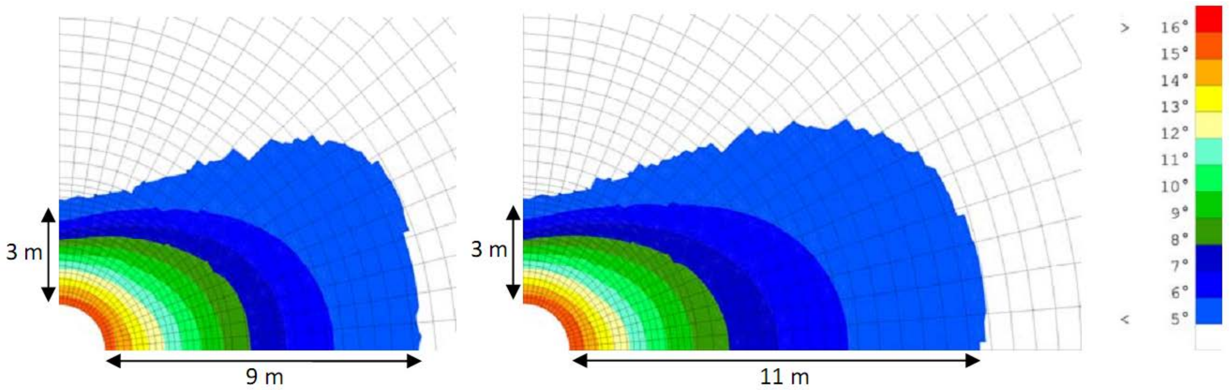

Figure 73: 2D plane strain model - Actualized ("hardened") Coulomb's friction angle at the end of the excavation (left) and at the end of the heater experiment (right). Initial value is 5° (in white)

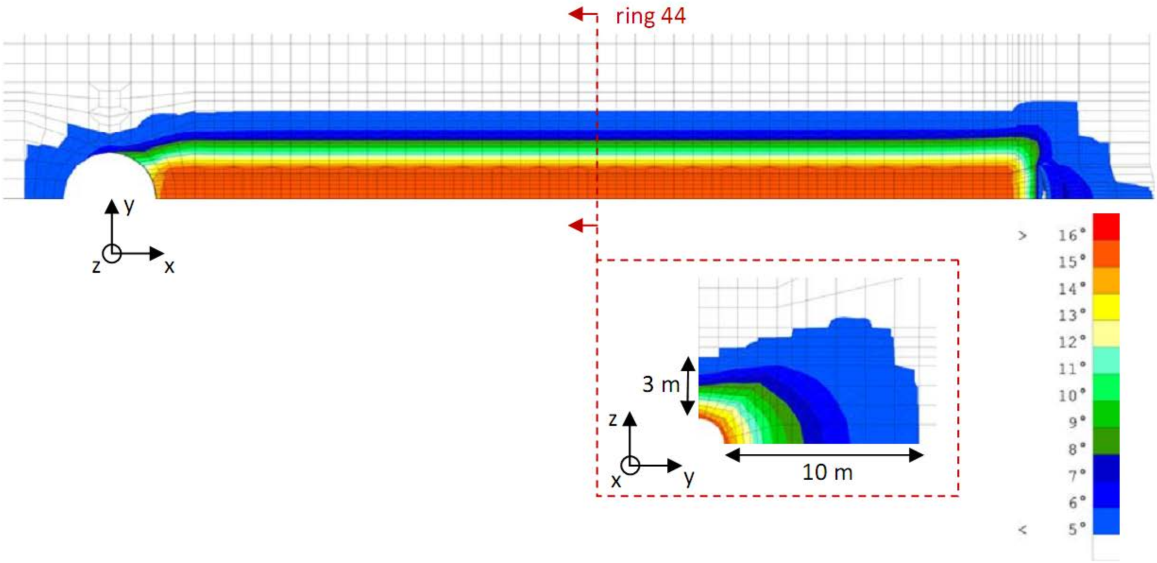

Figure 74: 3D model - Actualized Coulomb's friction angle at the end of the excavation. Initial value is 5° (in white)

4.3.6 Additional simulations

EPFL

EPFL carried out computations to assess the influence of non-linear thermo-elasticity and thermo-plasticity on the THM response of the repository, using the ACMEG-T constitutive law in both 1D axisymmetric and 2D axisymmetric models.

The obtained pore pressures and stress fields differ from those obtained with the other models. The differences are mainly due to the non-linear elasticity and the thermo-plasticity of the ACMEG-T model. An increase in rigidity as well as progressive plasticity induced by heating, causing an increase of the preconsolidation pressure, is considered in ACMEG-T. This causes an increase in excess pore water pressures, and consequently in effective stresses.

ULg

ULg has compared 2D plane strain simulation results based on 3 different thermoplastic laws, Drucker-Prager, TSOIL and ACMEG-T. Pore pressures are only slightly affected by the model of thermo-plasticity. This is probably due to the kind of thermo-plasticity involved by these models, which only affects the cap, i.e. the high isotropic stress states, and not the deviatoric mechanism.

ULg has also modelled in 3D the effect of anisotropy in thermal conductivity and in permeability. The main effect is observed on the pore water profile (Figure 75) where the anisotropic permeability (case $3D_{III}$) is different from the others.

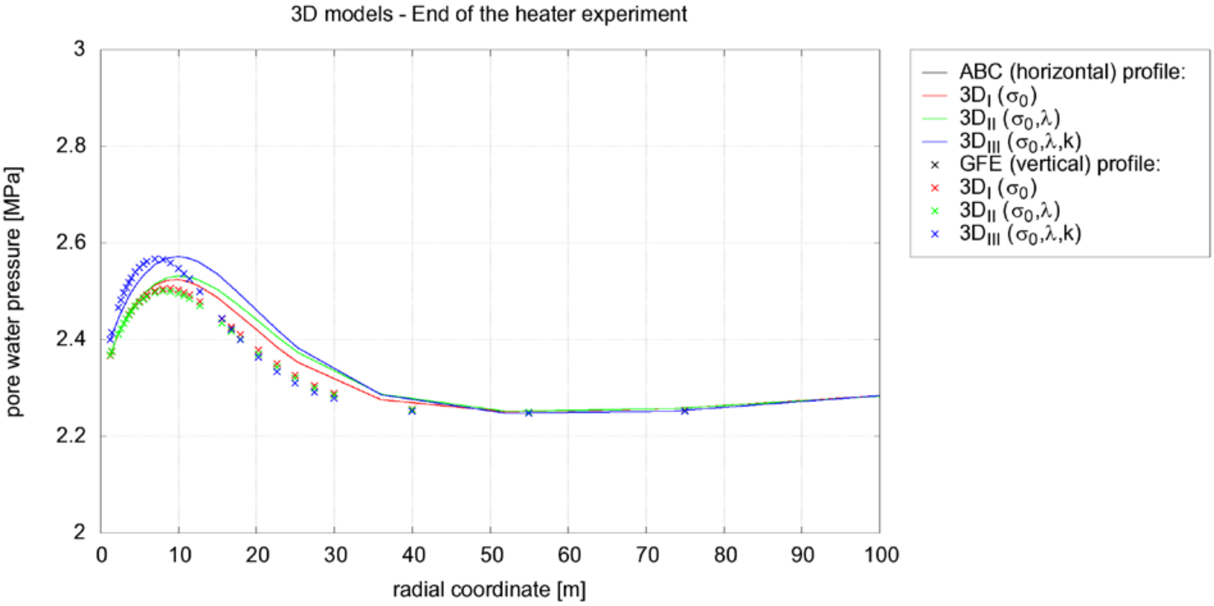

Figure 75: Pore water pressure profiles at the end of the heater experiment. Effect of the anisotropic parameters

EURIDICE

Euridice has tested the effect of the far field boundary conditions: fixed stress vs. fixed displacement, boundary at 100 or 300 m. As an example, the Figure 76 presents the pore water pressure profiles along boundary ABC after heating for 10.5 years. It appears that case 2 should be avoided. However in the actual case of PRACLAY boundary conditions in vertical direction are nearer then modelled.

Euridice has also analysed the effect of stress anisotropy, and has showed that it explains a number of features observed in situ, such as pore pressure evolution and gallery convergence, which are different on horizontal and vertical axis.

Eventually Euridice has shown that the large conductivity of the backfill material may significantly modify the longitudinal distribution of pore pressures in the near field.

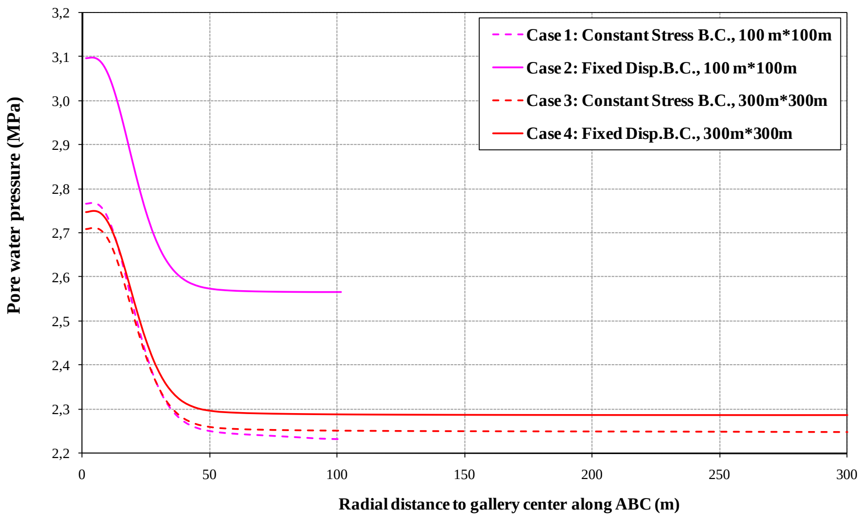

Figure 76: Pore water pressure profiles along boundary ABC for the four cases after heating for 10.5 years

CIMNE

CIMNE has analysed the initial state around PRACLAY experiment. It is known that the hydro-mechanical state is highly heterogeneous because it is influenced by the different excavations realized. Moreover, the low permeability of the clay rock delays significantly the reach of the steady state for pore pressure distribution, which affects in turn the stress distribution. the effect of the excavation of the connecting gallery on the hydro-mechanical state around Praclay experiment is studied.

An anisotropic model with a Mohr-Coulomb failure criterion has been used. Figure 77 shows a comparison between the pore pressure computed by the full anisotropic model and the isotropic model for one sensor located in a borehole in front of the test drift. It evidences the capability of the anisotropic model to capture the peak in pore pressure as the front approaches the sensors. This peak is mainly controlled by the anisotropy of elastic moduli.

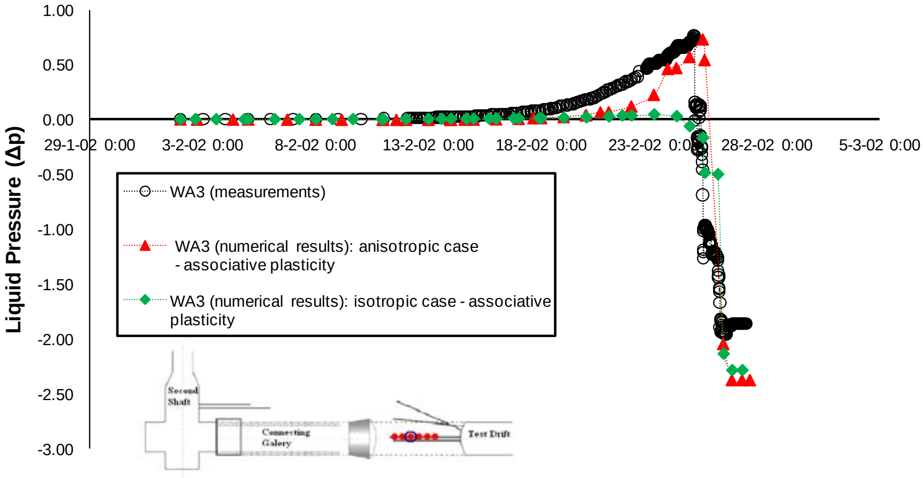

Figure 77: Computed pore pressure vs measurement at sensor A3 for the isotropic and full anisotropic model.

Figure 78 shows the profile of pore pressure along the centre axis of Praclay gallery previous to its excavation. It evidences an increase of pressure in a zone at a distance from the connecting gallery wall between 20 and 50m, that is around the second middle of Praclay heater. Magnitude of the increase reaches a maximum of 500 kPa (with respect to value of pore pressure in the far field) at 28m from the connecting gallery.

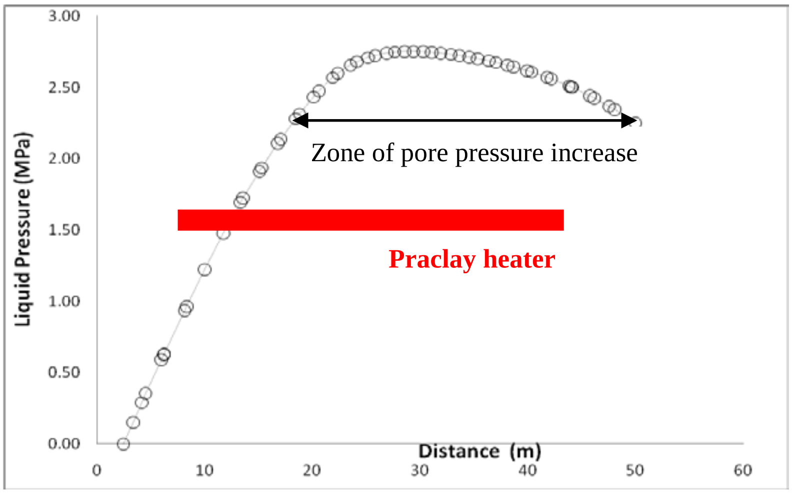

Figure 78: Profile of pore pressure along the centre axis of Praclay gallery previous to its excavation

The effect of anisotropy on the thermal field around PRACLAY experiment was also checked by CIMNE and found significant.

4.4 Conclusions

Globally, the results obtained by the different teams participating to the benchmark are in good agreement.
As expected, some differences are noticeable between the different 2D and 3D approaches, due to the inherent assumptions and limitations of each model:

- On one hand, the 2D plane strain model allows taking into account the anisotropy of the initial, leading to different behaviors in the horizontal and the vertical direction (this is mainly visible at the end of excavation in the pore water pressure profiles, the effective stresses field and the plastic zone extent). On the other hand, neither heat nor water flow is allowed in the out-of-plane direction, so the dissipation is only possible in the plane of the model. Hence, some values (such as the pore water pressure) are higher than in the 2D axisymmetric and 3D models, more especially in the vicinity of the PRACLAY gallery.
- The 2D axisymmetric model offers the possibility to model the PRACLAY experiment including details all along the axial direction, amongst which the bentonite sealing, the connecting gallery, the end plug, etc. Flows in the axial direction are also included and they clearly influence the results, i.e. the pore water pressure profiles. However, the lack of anisotropic properties in this approach constitutes the major drawback of the model when looking at the plastic behavior, leading to the differences observed in the stress paths and in the axisymmetric and less extended plastic zone extent.
- The 3D model appears as the ideal solution: both anisotropy and axial modeling can be included. However, this approach is much more resources consuming (computing time and required memory). To overcome this problem, a compromise must be found between a faster coarse mesh and a more precise and numerically stable refined mesh. The 3D model presented in this report is the fruit of several attempts to solve this problem within a few days of computation and getting results globally in accordance with the best predictions of the 2D plane strain and the 2D axisymmetric models.

5 Modelling laboratory experiments

This section presents the modelling of the experimental works realised within the WP3.1. For furthers details concerning the experiments, we refer to the deliverable related to this work package.

5.1 Introduction

In this section experimental and the numerical results are compared. The methodology used is the following. First, simulation has been realised with the parameters of a Drucker-Prager model used in the PRACLAY exercise. In a second step, a variation of the parameters is done in order to fit the experiment if necessary.

Table 5 presents the different sets of parameters tested. The three first sets come from the benchmark exercise on the Boom clay Hollow cylinder. The last set takes into account experimental points (from tests on Boom Clay performed before the beginning of the project) corresponding to failure in the (*p'*,*q*) plane, thanks to which it is possible to find rupture parameters. Figure 79 presents the different couple of (*p'*,*q*) point which corresponds to the failure of the clay. Using linear interpolation, the values of cohesion and of the friction angle of the clay can be estimated.

	E (MPa)	ν	c_i (kPa)	c_f (kPa)	B_c	ϕ_{ini} (°)	ϕ_{ini} (°)	B_ϕ	Ψ (°)	p_c (MPa)
Simul 01	300	0,125	300	300	0	18	18	0	0	2,3
Simul 02	300	0,125	300	300	0	5	18	0,01	0	2,3
Simul 03	300	0,125	300	100	0,01	5	18	0,01	0	2,3
Simul 04	200	0,25	115	115	0	15	18	0,01	0	2,3

Table 5: Table of parameters used for the first calculation of different laboratory experiment (Radu, 2009)

Figure 80 presents the axial strain versus the deviatoric stress during drained triaxial tests. This one illustrates comparisons between experimental and numerical results. Figure 81 presents the evolution of the volumetric strain with the axial strain. It can be observed in those figures that the set of parameters Simul02 seems to better fit all the different experiments.

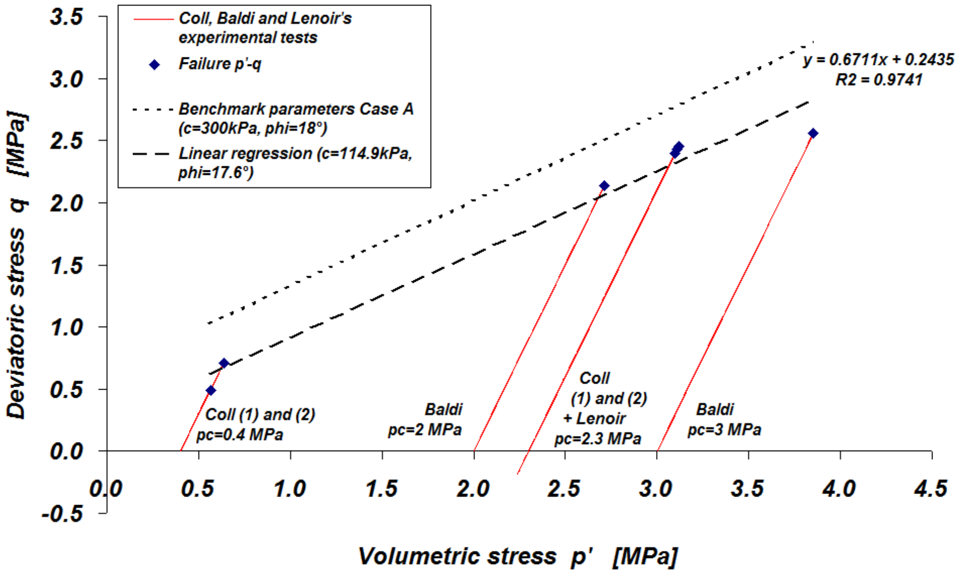

Figure 79: Deviatoric stress versus volumetric strain. Illustration of the different (p',q) couple corresponding to the failure of the sample for the different experiments

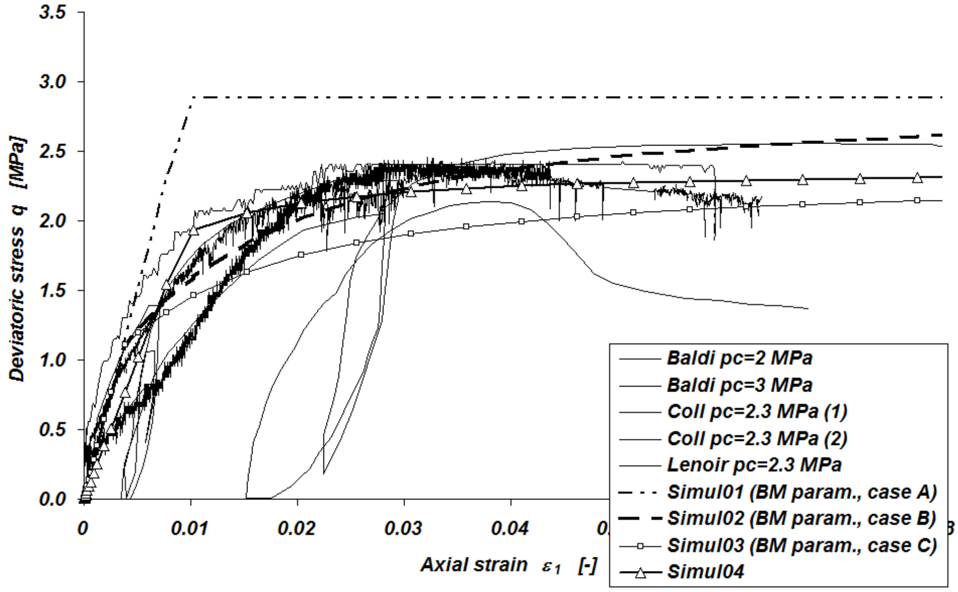

Figure 80: Deviatoric stress versus axial strain. Comparisons experimental and numerical results

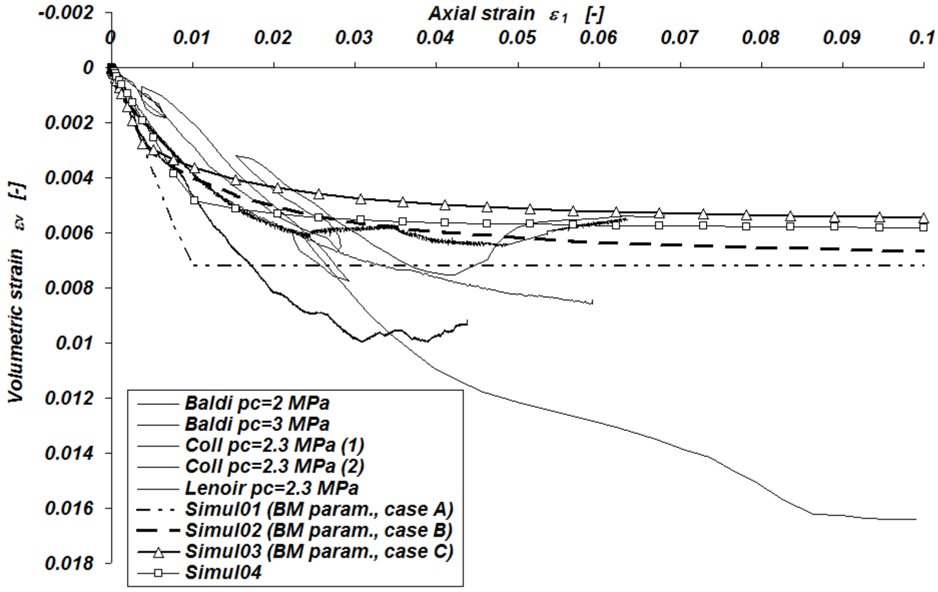

Figure 81: Axial strain versus volumetric strain. Comparisons experimental and numerical results

5.2 Numerical results and comparisons with experiments

As mentioned previously, the modelling is first done with the set of parameters used to model PRACLAY (SIMUL02). This set is called PARAM1 in Table 6, Table 7 and Table 8. Then a variation of these parameters are realised. This second set is called PARAM2_Team. In order to be coherent, PARAM2 is the same for all tests from one laboratory.

5.2.1 CERMES (ENPC)

CERMES has realised a drained test and an undrained test on a hollow cylinder made in Boom Clay. The undrained test is realised with a constant total mean stress. Table 6 presents the value of the different parameters used in this modelling. For the drained test, the parameters used for the PRACLAY modelling (PARAM1) fit well the curves. Nevertheless, a modification of the hardening rule may be done to improve the numerical predictions.

For the drained test, Figure 82 presents the modellings realised in this case and shows that the numerical prediction is able to reproduce the deviatoric behaviour with both sets. On the other side, the evolution of the volumetric strain is underestimated (Figure 82(b)). Concerning the undrained test, the mean total stress was kept constant during the test. Concerning the deviatoric behaviour Figure 83(a) shows that the numerical prediction underestimated the experimental observations. Moreover, the experimental evolution of the pore water pressure is overestimated but the tendency is well reproduce.

	E [MPa]	ν	c_i [kPa]	c_f [kPa]	β_c	ϕ_i [°]	ϕ_f [°]	β_ϕ	ψ [°]	p_c' [MPa]
PARAM 1	300	0.125	300	300	0	5	18	0.01	0	2.3
PARAM2_ENPC	300	0.125	300	300	0	7	18	0.02	0	2.3

Table 6: Parameters used to model the hollow cylinder test done by CERMES

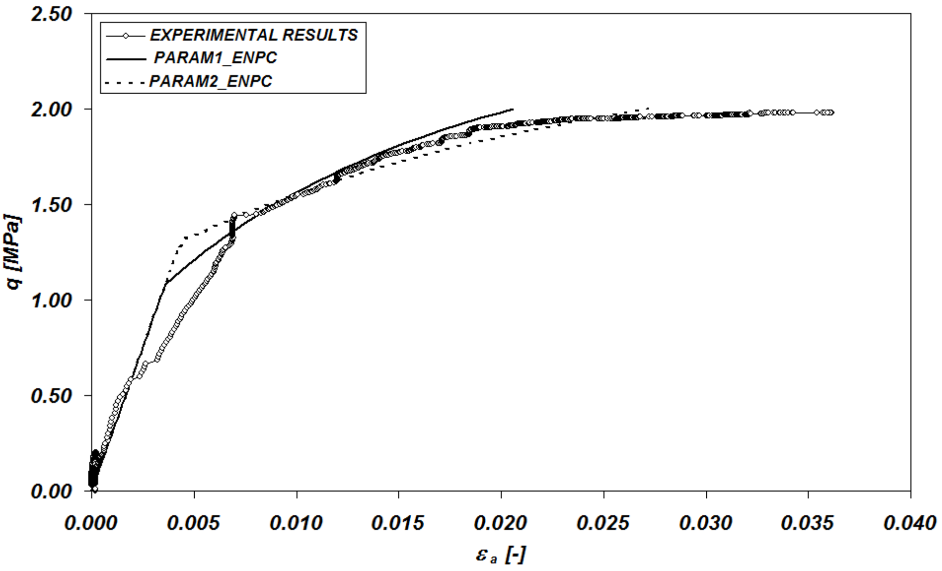

(a)

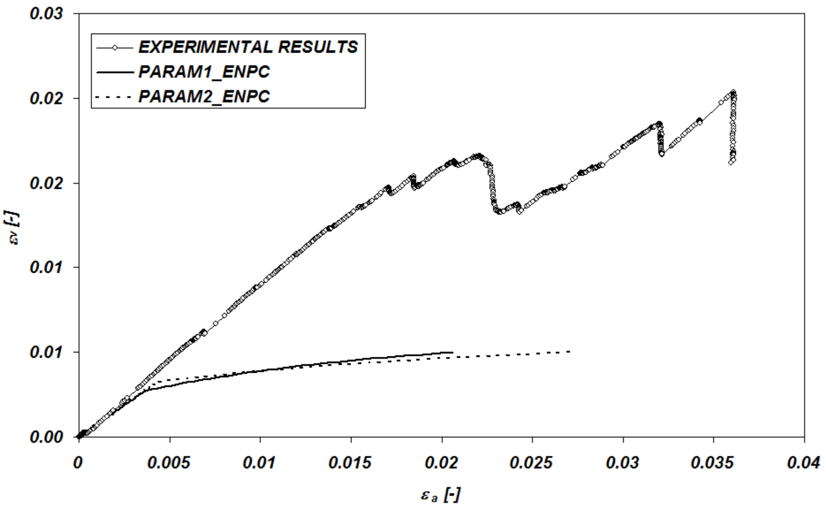

(b)

Figure 82: (a) Deviatoric stress versus the axial strain for the drained test realised by CERMES. (b) Axial strain as a function of the volumetric strain

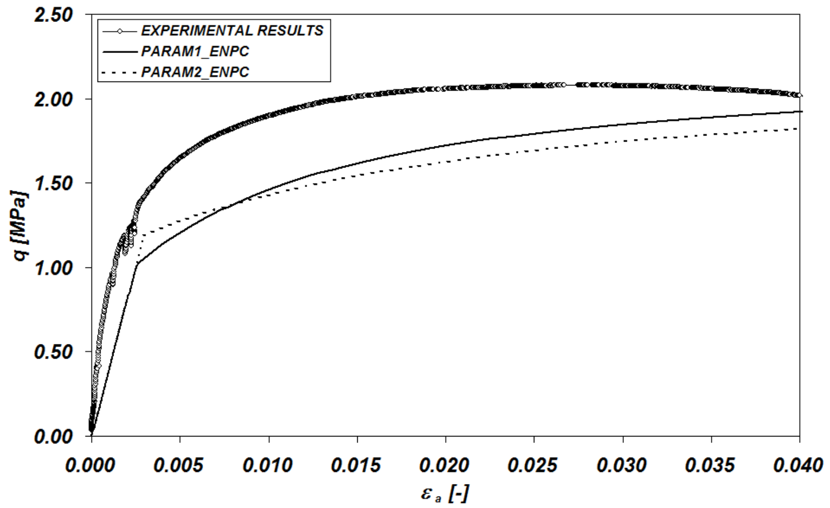

(a)

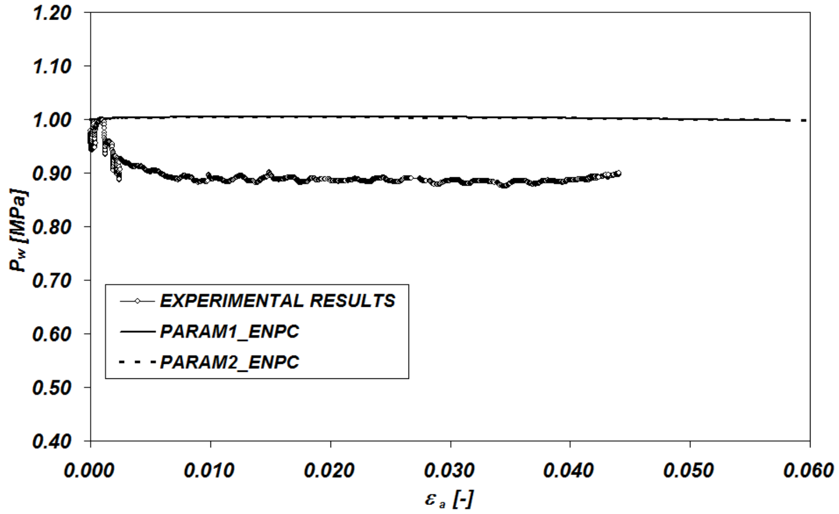

(b)

Figure 83: (a) Axial strain versus deviatoric stress for the undrained test realised by CERMES. (b) Axial strain versus volumetric strain

5.2.2 L3S-R (UJF)

This part presents the comparisons between experimental and numerical results for the two tests realised by L3S-R. For memory, UJF has realised a non-conventional shear test and an undrained triaxial test.

Non conventional shear tests

Table 7 presents the parameters used to model the different experiments of L3S-R. Figure 84 presents the deviatoric stress as a function of the mean total stress. It can be observed that the numerical modellings with the set of parameters PARAM2 fit well the experimental curves.

PARAM1 parameters do not permit to fit the curves. Calibrations can be well done if the rigidity (E) and the dilatancy angle (ψ) are increased. The dilatancy angle is justified experimentally

(Figure 86) by the decrease of the pore water pressure with the axial strain. Figure 85 presents the evolution of the deviatoric stress with the axial strain.

	E [MPa]	ν	c_i [kPa]	c_f [kPa]	βc	ϕ_i [°]	ϕ_f [°]	β_ϕ	ψ [°]	p_c' [MPa]
PARAM 1	300	0.125	300	300	0	5	18	0.01	0	2.3
PARAM2_UJF	800	0.125	300	300	0	8	18	0.003	10	2.3

Table 7: Parameters used for the modelling of the experiments of L3S-R

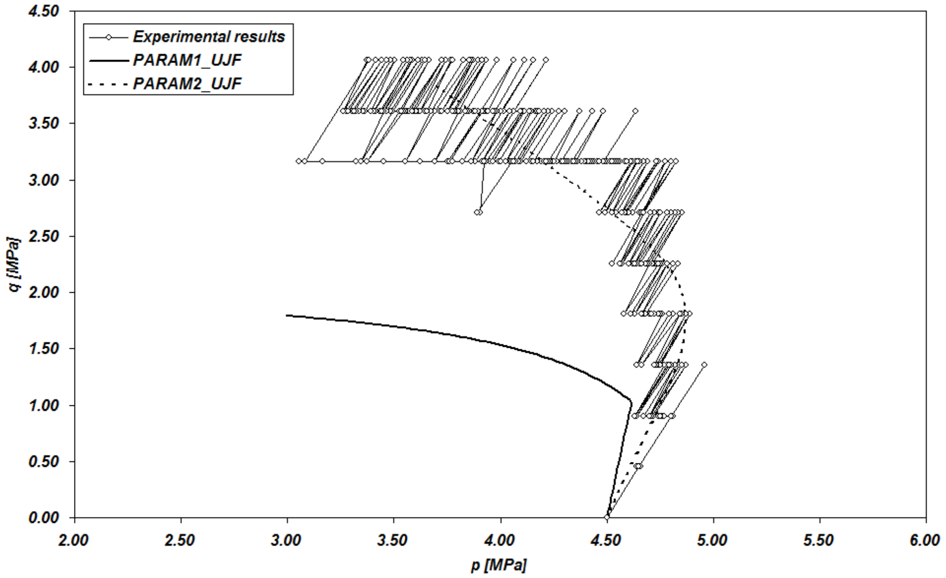

Figure 84: Deviatoric stress versus mean total stress

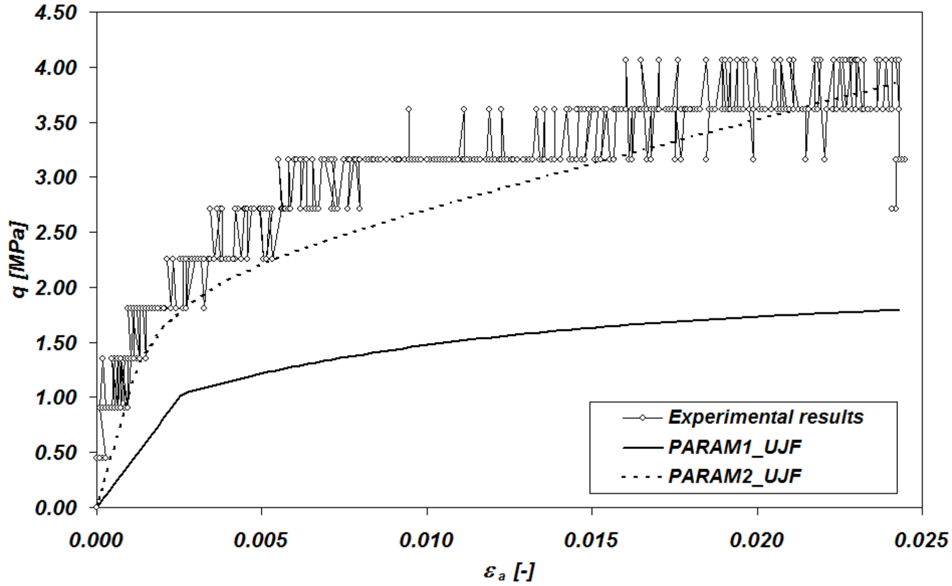

Figure 85: Deviatoric stress versus axial strain

Figure 86 illustrates the evolution of the pore water pressure during the non-conventional shearing test. During the test, the pore water pressure decreases during the increase of the axial strain. This decrease may be explained by the apparition of volumetric plastic strain or dilatancy effect. Unfortunately, calibrations provide a dilatancy angle which overestimates the pore water pressure decrease.

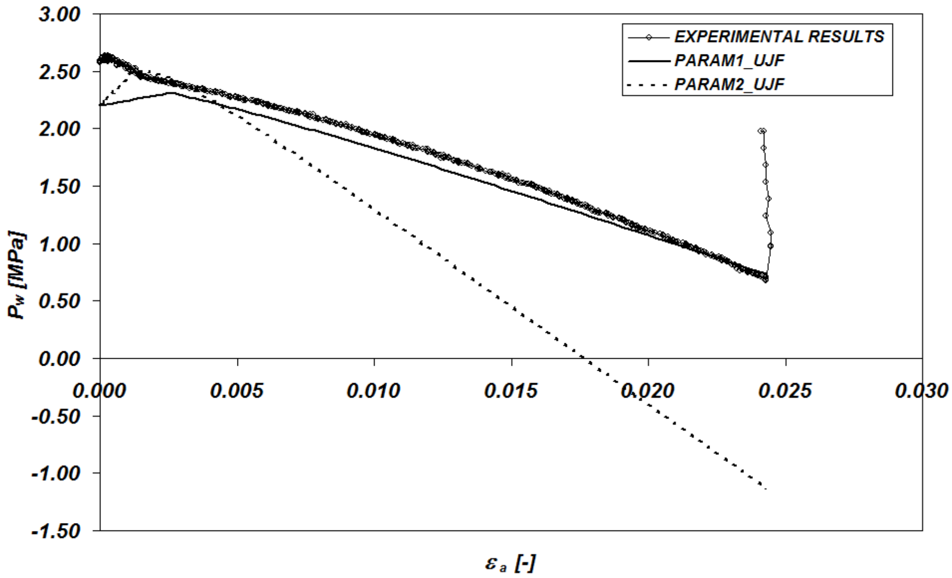

Figure 86: Pore water pressure versus axial strain during the non-conventional shear test

Conventional undrained triaxial shear test

Figure 87 presents the evolution of the deviatoric stress as a function of the axial strain. The same conclusion as the non-conventional shear test may be done. The model is able to fit the experimental results with the set PARAM2. But, in this case, the rigidity seems over-estimated. Nevertheless, it can be shown that parameters initially calibrated on non-conventional shear test still provide a good calibration of conventional undrained test. In this case, the pore water pressure seems constant during the test. The use of dilatancy angle does not permit to reproduce this behaviour (Figure 88).

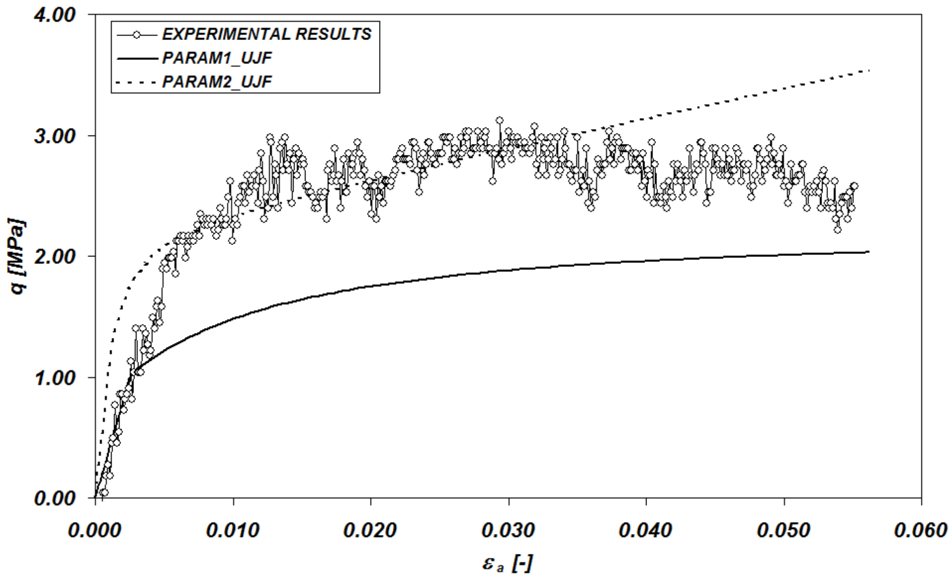

Figure 87: Deviatoric strain versus axial strain for the undrained shear test

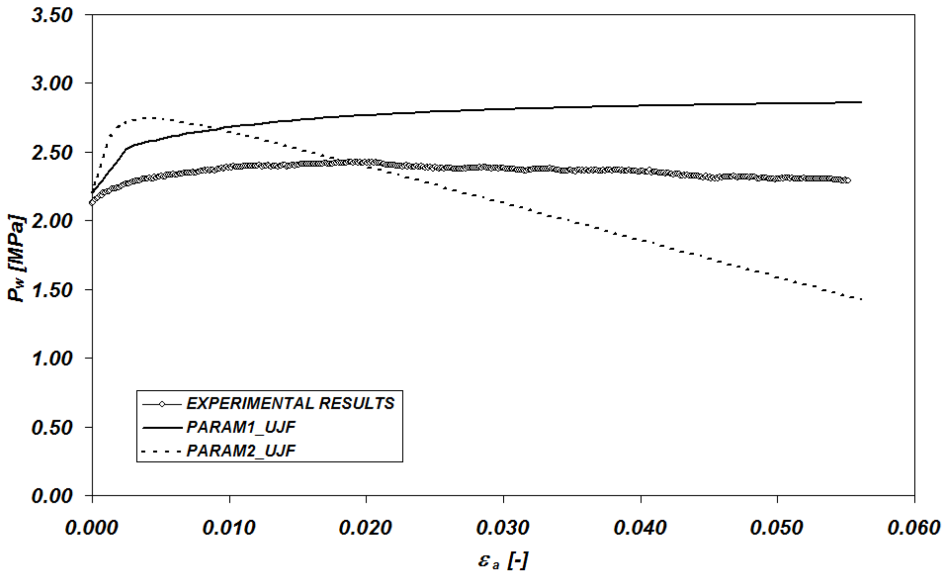

Figure 88: Pore water pressure versus axial strain for the undrained shear test realised by L3S-R. Comparisons between the numerical and the experimental curves

5.2.3 GEO3 (ULg)

Table 8 presents the parameters used for the modelling of the experiments realised by GEO3. Figure 89 presents the comparisons between the numerical and the experimental results for the different undrained tests realised by GEO3. To fit the numerical curves, an angle of dilatancy is included in the model. It can be observed that considering a dilatancy angle of 5° provides a good calibration in term of deviatoric behaviour. On the other wise, the evolution of the pore water pressure is not reproduce as shown in Figure 90.

	E [MPa]	ν	c_i [kPa]	c_f [kPa]	βc	ϕ_i [°]	ϕ_f [°]	β_ϕ	ψ [°]	p_c' [MPa]
PARAM 1	300	0.125	300	300	0	5	18	0.01	0	2.3
PARAM2_ULg	300	0.125	300	300	0	8	18	0.001	5	2.3

Table 8: Parameters used for the modelling of the experiments realised by GEO3

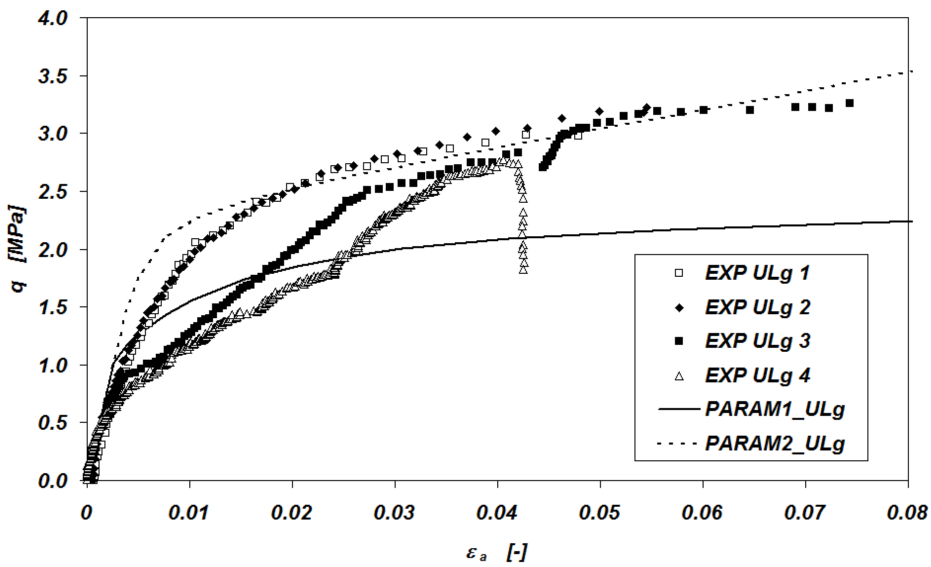

Figure 89: Axial strain versus deviatoric stress. Comparisons between experimental and numerical results for the undrained tests realised by GEO3

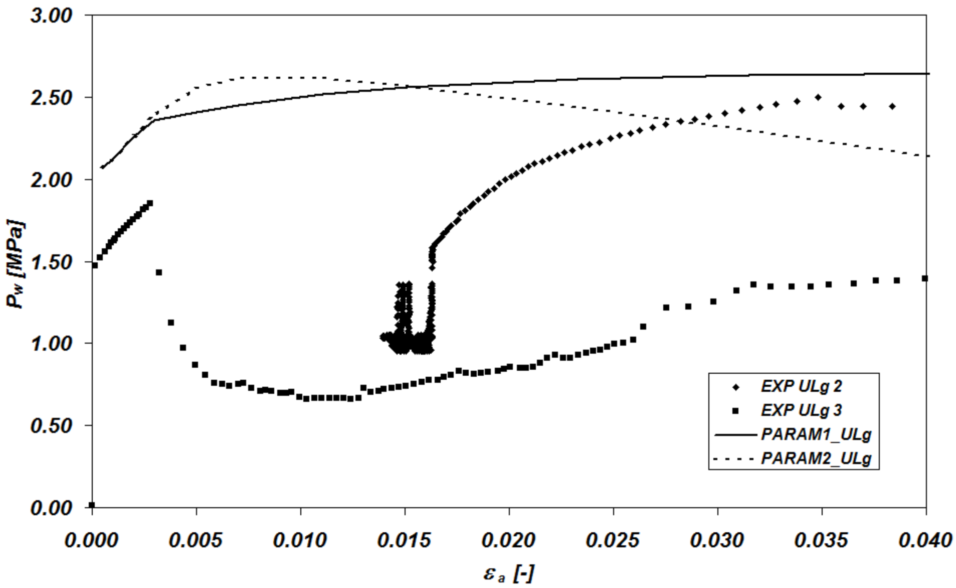

Figure 90: Example of evolution of axial strain versus pore water pressure for this modelling of the experiment by ULg

5.2.4 Conclusions

Several laboratory experiments (drained, undrained, etc.) have been modelled. Figure 91 and Figure 92 presents a synthesis of this experimental work and the associated modellings. In term of stress path, Figure 92 presents the stress paths followed during the experiments for all the teams. Figure 92(a), (b) and (c) present the stress path in the (*p*,*q*) plane while Figure 92(a'), (b') and (c') present the stress path in the (*p'*,*q*) plane. UJF proposed to reproduce a drained triaxial test and a non-conventional shear test. These paths are described in Figure 92(a) and Figure 92(a'). CERMES proposed to study a drained and an undrained path as illustrated in Figure 92(b) and Figure 92(b'). Finally, ULg proposed to apply an undrained triaxial path as presented in Figure 92(c) and Figure 92(c'). For this last experiment, a loop at the end of the test indicates the failure of the sample.

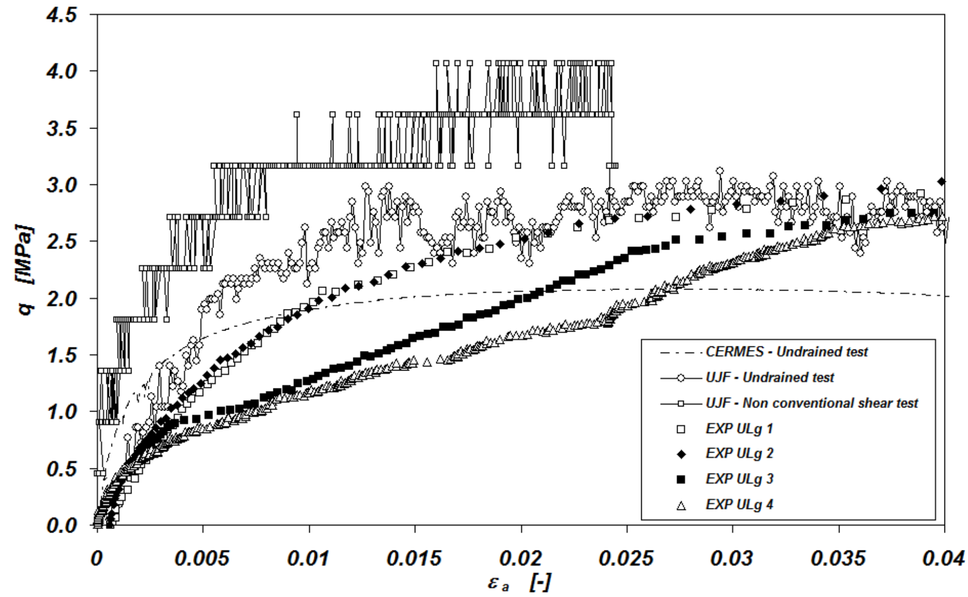

Figure 91: Synthesis of the laboratory experiment in the (ε_a, q) plane

In order to fit the experiments, a variation of the set of parameters (PARAM1, defined for PRACLAY) has been done in section 5.2. This set of parameters corresponds to a Drucker-Prager criterion. As compared to initial set (PARAM1), only a few parameters have been modified to fit the experimental curve. The major modification concerns the dilatancy angle and the modification of the hardening rule of the friction angle criterion. Notice that the elastic parameters through the Young modulus, has also been changed to fit the experiments by UJF. Table 9 summarises the variation of the parameters realised in these modellings. Figure 92 presents the comparisons of the experimental and the numerical stress path for all teams and shows that the experimental results can be reproduce globally.

	E [MPa]	ν	c_i [kPa]	c_f [kPa]	βc	ϕ_i [°]	ϕ_f [°]	β_ϕ	ψ [°]	p_c' [MPa]
PARAM 1	300	0.125	300	300	0	5	18	0.01	0	2.3
PARAM2_UJF	800	0.125	300	300	0	8	18	0.003	10	2.3
PARAM2_ENPC	300	0.125	300	300	0	7	18	0.02	0	2.3
PARAM2_ULg	300	0.125	300	300	0	8	18	0.001	5	2.3

Table 9: Summary table of the different parameters used to model experiments. The principal difference with param1 comes from the dilatancy angle and the hardening rule

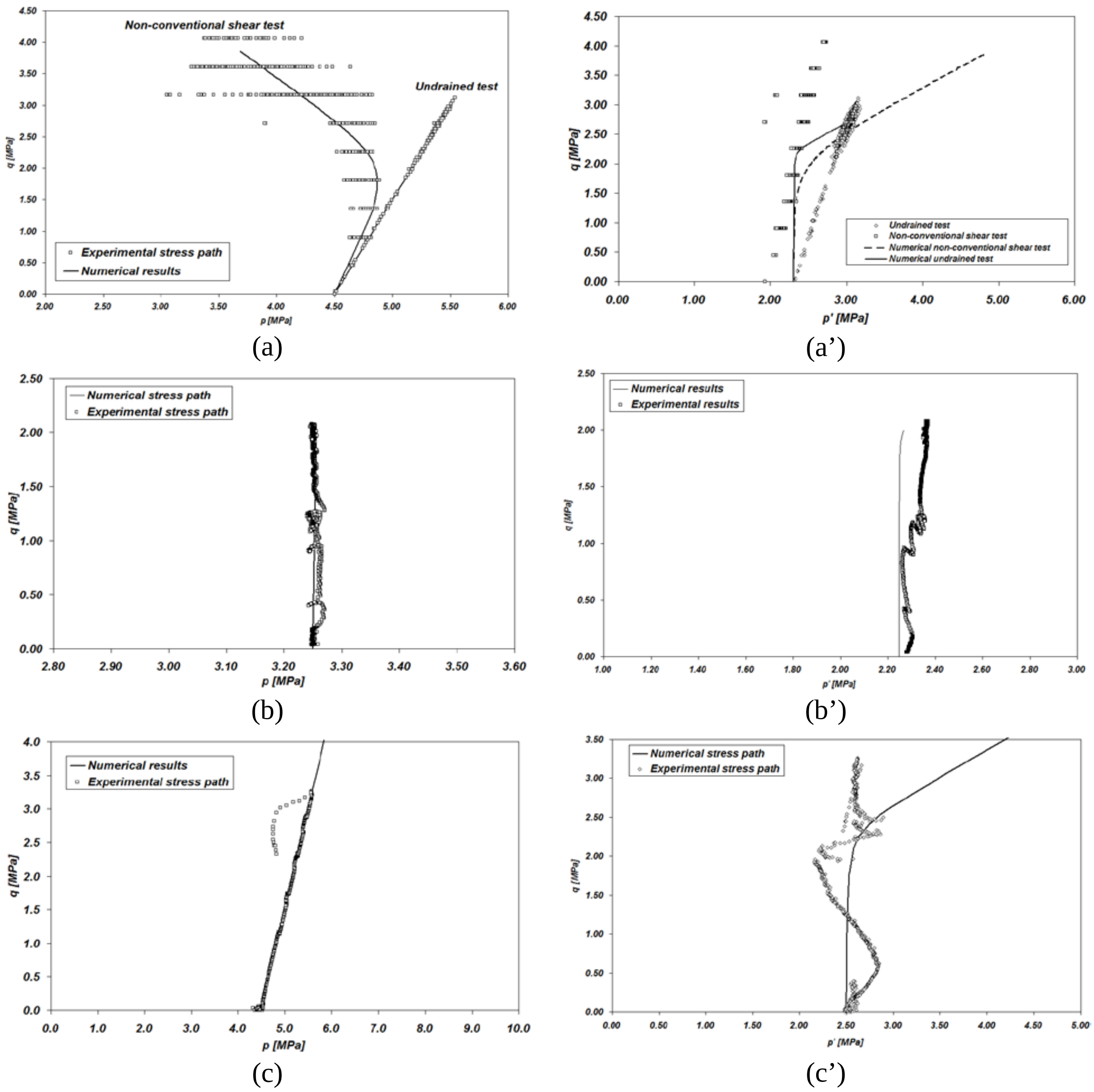

Figure 92: Comparison between numerical and experimental stress path. Comparison for UJF (a) and (a’), for CERMES (b) and (b’) and for ULg (c) and (c’). (a), (b) and (c) represent the stress path plot in the (*p*,*q*) plane while (a’), (b’) and (c’) illustrate the stress path in the (*p’*,*q*) plane

5.3 Global comparisons between experimental and numerical stress paths

This section presents a comparison between the stress paths studied experimentally and the stress path followed in the modelling of the hollow cylinder and of PRACLAY. Figure 93 presents the whole stress paths for both modellings in the (*p*, *q*) plane (Figure 93(a)) and in the (*p’*, *q*) plane (Figure 93(b)). The entire stress paths are plotted for a point in the ten first centimetres of the surface of the cavity for PRACLAY and at the surface of the cavity for the hollow cylinder. Considering the hollow cylinder, the clay can be considered as an isotropic (ISO) or an anisotropic material. Two cases of anisotropy are considered. The first one considers the anisotropy of the elastic parameters while the surface of plasticity is isotropic (ELAST ANISO). The second one takes into account the anisotropy of the plasticity surface in addition to the anisotropic elasticity (ELASTOPLAS ANISO). Of course, when the anisotropy is considered, several directions are analysed (0°, 45° and 90°). For the PRACLAY modelling, a 2D plane strain (2DE) and an axisymmetric (axisym) case are studied. For further details of these stress paths, we refer to the different annex of this deliverable and in particular to annex 1 and annex 5. If we except the parameters used and the difference of hardening rules in the modellings, it can be observed that all the curves present the same shape which is linked to an excavation process. Indeed, all the curves seem to be in a spindle.

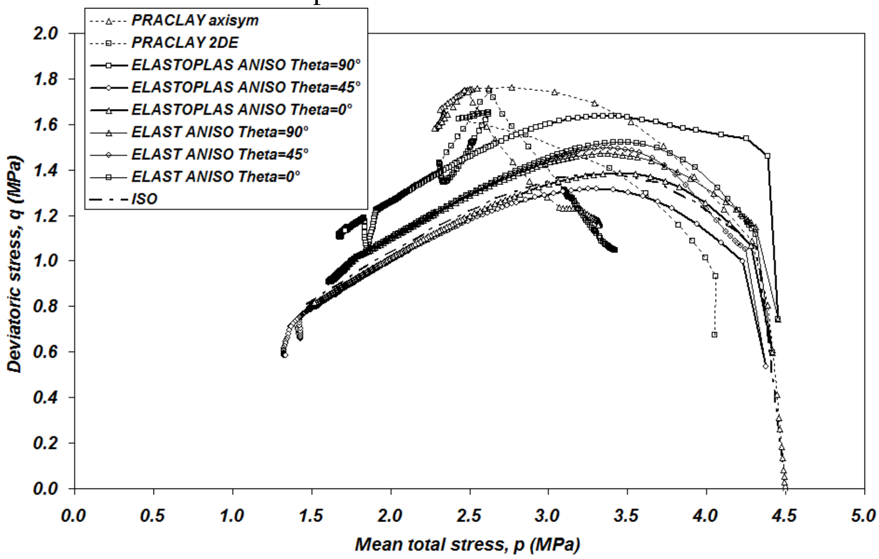

(a)

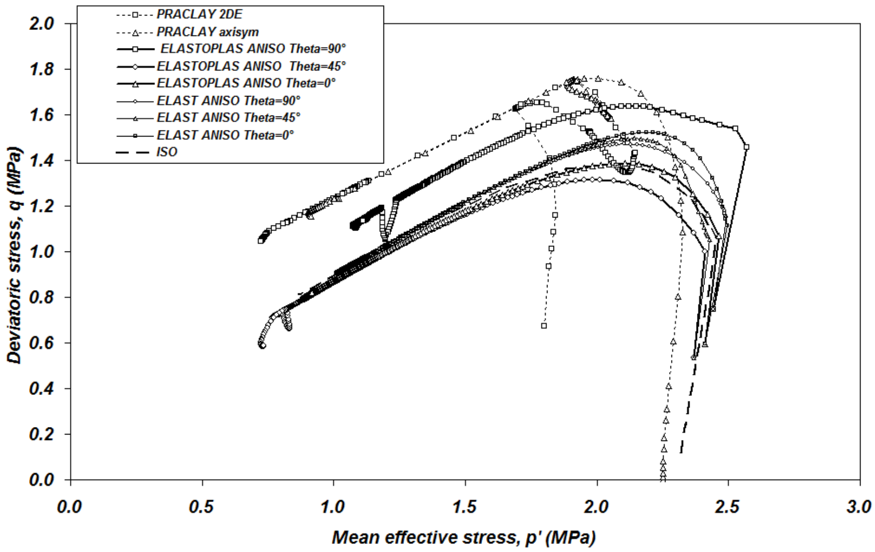

(b)

Figure 93: Representation of the different stress path of the hollow cylinder modelling and of the PRACLAY modelling. The stress path are plotted in the (*p*, *q*) plane and in the (*p'*, *q*) plane

A comparison between the different stress paths followed in the laboratory experiments and the stress path followed by a point located at the surface of the cavity of the hollow cylinder (see D13 – Annex 1) can be seen in Figure 94. This last stress path corresponds to a modelling realised with the same set of parameters as PRACLAY (PARAM1). The stress paths are plotted in the (*p*, *q*) plane (Figure 94(a)) and in the (*p'*, *q*) plane (Figure 94(b)).

In the following, we compare the total stress paths. For the classical undrained triaxial test, the followed path is the same for ULg and UJF. The undrained test realised by CERMES is a vertical path, the total mean stress was kept constant during the test. Finally, the two last paths correspond to the non-conventional shear test realised by UJF and the numerical stress path of the hollow cylinder. It may be observed with these last two paths that their shape is similar. As a consequence, the non-conventional shear test looks like the excavation path of the hollow cylinder and seems to the most appropriate to reproduce the stress path of an excavation.

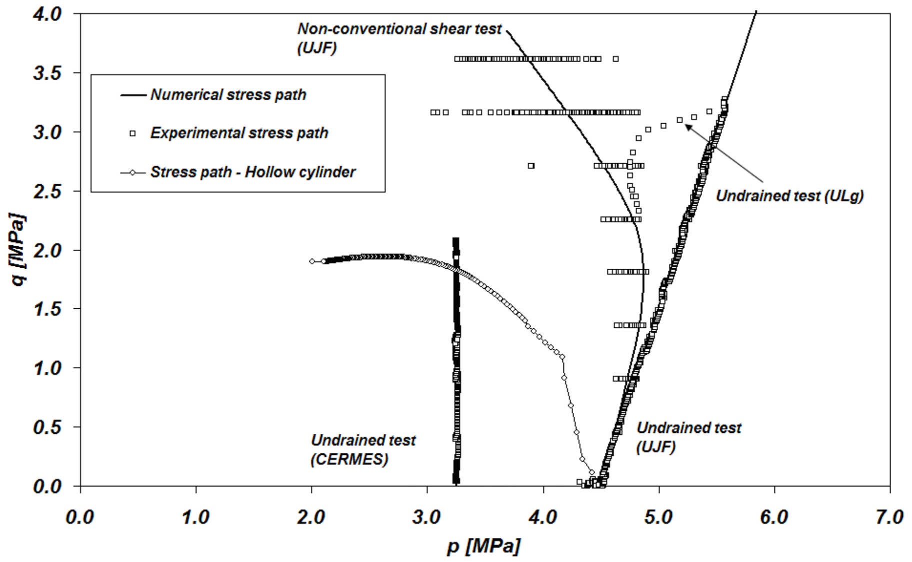

(a)

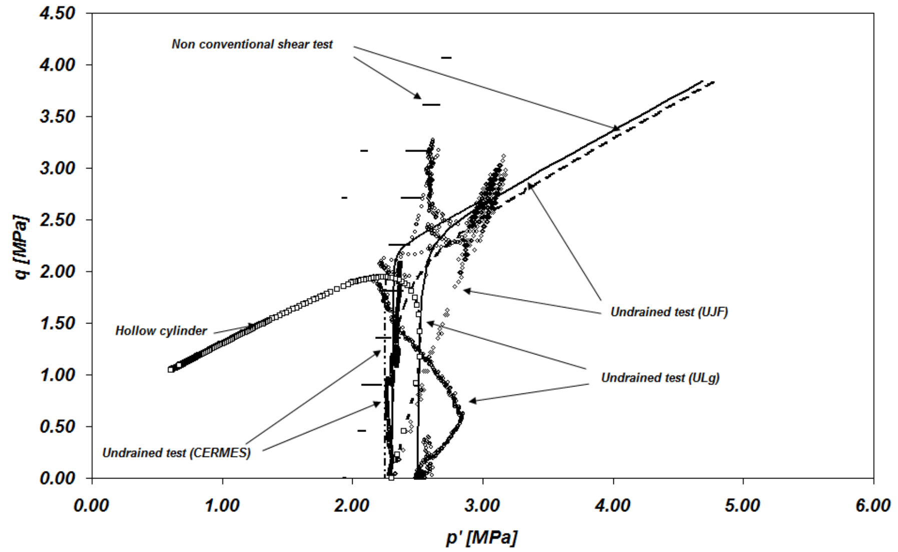

(b)

Figure 94: Comparison between various stress paths from the experimental work to the numerical work including the stress path of the modelling of the hollow cylinder. The stress path are plotted in the (*p*, *q*) plane and in the (*p'*, *q*) plane

6 Relevance of the modelling work and results to the performance assessment (PA) and repository design

6.1 Background

The excavation damaged zone (EDZ) in clay is currently not considered to be a critical issue for PA (Bernier et al. 2006). However, a sound scientific understanding regarding the evolution of the damaged zone (DZ) to thermal/chemical/gas changes through time is required to adequately support the arguments presented within a safety case (Sillen et al., 2008).

The experimental works performed in TIMODAZ WP3 and WP4 investigate various aspects of the interacting processes occurring within the clay around a disposal system for heat-emitting radioactive waste during the thermal transient. Sound characterization of the clay behaviour under these evolving conditions and the supporting modelling work for the interpretation of the experimental results enable a better understanding of the processes that are relevant to the long-term safety of the repository. Furthermore, as the thermal transient is expected to span several centuries, the development and calibration of the phenomenology-based models are essential steps towards meeting the safety case requirement of adequate understanding of the long-term evolution at the repository scale. The well calibrated models make the sound quantification of the thermal impact on the host-clay and its Damaged Zone (DZ) at long-term scale and repository scale feasible.

6.2 Contribution of modelling works in WP5 to PA

In a clay-based geological repository hosting heat-emitting radioactive waste, thermal-hydro-mechanical (THM) coupled processes occur within the clay as they have been extensively observed in the laboratory and in-situ tests. The majority of the efforts made in WP5 aims at improving the predictive capability of models describing the relevant processes including THM couplings and to obtain a better characterization of these processes through the calibration of model parameters and to the extent possible through validation of the physical models and their parameters.

The extensive benchmarking exercises carried out in WP5 helped modellers improve their capability in manipulating the numerical tool for complex THM problems. These benchmarking exercises primarily serve as a tool to detect and fix code errors and to avoid the inadequate use of the codes. In TIMODAZ, comparisons of numerical results among different teams using different numerical tools have shown that the majority of participants obtain similar results in all benchmark exercises. This not only provides evidence for the verification of these numerical tools in solving THM coupled problems, but also demonstrates that the modellers are applying these different tools in a similar, arguably proper way.

Numerical modelling software is a powerful, fast and rather cheap tool to study the mechanism related to the physical phenomena observed in laboratory experiments and field tests. But the precondition is that the conceptual model is reasonably extracted from the real problem. Figure

76 gives an example of the bias caused by the far-field mechanical boundary conditions on the pore water pressure.

HM perturbation is believed to be reasonably well understood and can be realistically reproduced for the excavation and ventilation phases (Bernier et al., 2006; Bernier et al., 2003; Su (eds)) . In TIMODAZ, numerical modelling for HM disturbances within host clay induced by excavation of the PRACLAY gallery suggests that the initial stress anisotropy is a key factor to reproduce the anisotropic convergence around the gallery and the observation that the water pressure decreases above or below the gallery while it increases to the right and left of the gallery. This is a concrete example of a modelling study which draws attention to a specific feature (here: anisotropy) and hence proves to be helpful in steering the R&D programme (here: effort to better characterise in situ stresses and material anisotropy in Boom Clay).

Benchmarking campaigns for the ATLAS III heater test show that the essential features of the THM responses during the thermal transient can be captured, especially the temperature evolution can be reproduced fairly well (Figure 41). Concerning the evolution of the pore water pressure in the surrounding clay induced by the heater, variation pattern in the 3D modelling is quite similar to the experimental data. However, the numerical results underestimate the measurements (Figure 42). The discrepancy can be minimized by increasing the elastic modulus which could be justified by the non-linear behaviour of clay (Mair et al., 1992). Figure 95 shows a satisfactory correspondence between modelling results and measurements for pore-water pressure by doubling the Young's modulus.

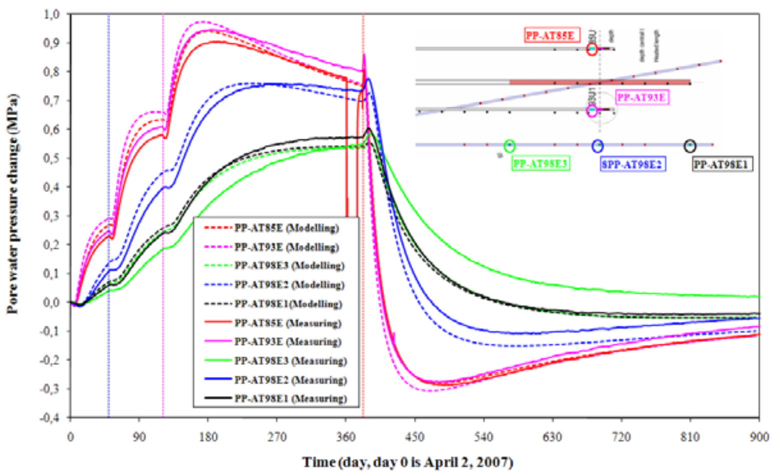

Figure 95: Comparison between numerical simulations and measurements of excess pore water pressure (additional computations by EURIDICE)

Numerical modelling works carried out in WP5 improved the accuracy of model parameters through calibration with in-situ test results. Transverse anisotropic thermal conductivity is well quantified through a medium-scale test: the ATLAS III heater test. The improved knowledge of thermal conductivity enables a more reliable description of the temperature evolution in clay. This is significant to the repository design which is based on an acceptable increase in temperature with respect to a criteria established independently on the basis of technical considerations (for the EBS) and legal considerations (for the subsoil) (Dujacuier, 1996). Taking into account the anisotropy in the temperature evaluations is anticipated to result in a better optimization of the spacing of galleries and the spacing of the waste packages in these galleries.

Another valuable contribution of the TIMODAZ project is to confirm the anisotropy of the clay host from various experimental tests. Besides the transverse anisotropy of the thermal conductivity mentioned above, including other structural anisotropic properties (elastic modulus, permeability, etc.) and in situ stress anisotropy for clay in the numerical modelling has been proven to improve the simulation results significantly. Considering the initial stress anisotropy in PRACLAY simulations results in elliptic hydraulic equipotential patterns around the gallery, which are consistent with the in-situ observations. Some specific features exhibited in the ATLAS III heater test, e.g. the reversed variation of pore water pressure for a short time at the beginning of each power change, can only be reproduced by including cross-anisotropic elasticity. It was also found that the mechanical anisotropy is the reason of the apparent anisotropic convergence around the central hole in the medium-scale hollow-cylinder tests. The characteristic of transverse anisotropy in clay results that the heat and gas in the repository system are prone to diffuse preferentially along the bedding plane, thus enhancing sub-horizontal rather than vertical transport.

Several constitutive models with emphasis on strain/damage localization have been attempted in the simulation of the medium-scale hollow-cylinder tests. A second gradient model was added to the strain cohesion softening model by UJF to simulate the evolution of the strain localization around the inner part of the sample. The embedded fracture model (permeability-strain coupling model) adopted by ULG allows the reproduction of the drastic increase of the permeability of the damaged sample, while the porosity-dependent relationship (Kozeny's model) can not (Figure 18). With the help of imaging techniques, effective validation of these new numerical models becomes a possibility. Comparing with conventional continuum models, these advanced models shed light on the evolution of DZ structure and the quantification of its properties.

6.3 Remaining open questions

Numerical simulations have been used to interpret the test results and to help understanding the mechanisms in relation with the observed phenomena. Significant progress has been gained within the TIMODAZ project for both the understanding of the processes and the development of the advanced models. However, some uncertainties could be further reduced in the future.

Numerical simulations of the hollow-cylinder tests enable a better understanding of the creation and evolution of the damage zone at the laboratory scale under conditions reasonably analogue to those of a real repository. The developed models are able to reproduce the main processes that occurred in the tests. However, the uncertainties embedded in the tests (pre-existing cracks, influence of membrane and boundary conditions, indirect displacement measurements, etc.) make a quantitatively satisfactory reproduction of displacement field rather difficult.

Advanced stress-strain models incorporating thermal impacts have potential applicability, but the calibration of the model parameters of such complex models still needs improvement. Laboratory tests related to thermal loading are not easy to conduct. Both the relative sparseness and the diversity of the previous test results make the calibration a big challenge. With the newly developed apparatus and strictly regulated testing procedures, the consistency in the test results have been much improved, which will definitely facilitate the model calibration in the future provided that the test equipment developed with considerable effort for TIMODAZ can now be used on a regular basis.

The geological repository is a very complex system with thermo, hydraulic, mechanical and chemical processes evolving simultaneously. The application of cementitious backfill/liner in the gallery imposes an alkaline attack on the clay in the near field. In combination with high temperature, the reactivity of some types of clay particles (e.g. smectite, organic matter, etc.) may alter the clay in the long-term. Under these circumstances, whether the combined effects of temperature and the alkaline perturbation would change the THM behaviour of the clay in a significant way still remains somewhat uncertain.

The current numerical models incorporate models for the heat/moisture transfer, mechanical stress-strain evolution as well as their interactions, especially in relation with the thermal effects. These models are capable of describing the main processes occurred within the host clay around a repository hosting heat-emitting nuclear waste (see previous section). More complicated models are under development with the intention to improve the predictive capability by including more complete aspects in the models. With the increasing complexity involved in the models, the number of parameters expands and the uncertainty increases at the same time, which might not be helpful to a clear understanding of the relevant processes. Similar as the compromise we need to seek between 2D and 3D conceptual models, a balance between the models complexity and interpretation transparency should be made. Experiences from the parameter determination in the ATLAS III test give a good example of successful quantification of model parameters from the test designed with "simple and clean" boundary conditions.

In brief, the current status of the modelling work with respect to the formation and evolution of the DZ with time is concluded as:

- Considerable progress **has been made** within the framework of TIMODAZ in adequately capturing key features and processes occurred within the host clay around a repository hosting heat-emitting nuclear waste (e.g. HM coupling, anisotropy, THM coupling, thermoplasticity, damage-dependent permeability, etc);
- Quantification of the plastic zone (i.e. how far it goes) and the evolution of DZ extent, as well as far field perturbations seems **within reach**;

Modelling of the plastic zone itself, in particular the part of the plastic zone which corresponds to a DZ, (e.g. fracture patterns) and quantification of its properties (e.g. permeability) **remain elusive**.

7 Conclusions

The initial work forecasts have been more or less followed. However, as we had in mind the numerical simulation of lab and in situ experiments, the project was evolving following the experimental results acquisition.

The numerical simulation of small scale lab hollow cylinder test has been done with different mechanical elastoplastic models (Drucker-Prager, Mohr-Coulomb, ACMEG-T, different hardening / softening scheme). During the project, it appeared that hydromechanical anisotropy and permeability evolution with strain were important topics. New developments have been achieved (see deliverable D10) and used in our numerical simulations: mechanical anisotropy and permeability changes are crucial for a good simulation of the experiments. Moreover, micro tomography of samples before, during and after tests by EPFL, suggest some strain localisation. So numerical simulation of strain localisation has been achieved using second grade models and using advanced constitutive models including anisotropy. They have shown that the observed strain pattern is partly reproduced.

Atlas medium scale in situ heating test modelling shows again the anisotropy importance, and especially that mechanical anisotropy may explains some observed specificities of pore pressure evolution, that where nor understood in the preceding. This implies that 3D models are needed. Non linear elastic mechanical behaviour has also been checked.

The Mont Terri medium scale in situ tests put in evidence the mechanically induced permeability and its anisotropy evolution. Further progresses in these experiment modelling will require to take into account strain localisation and 3D effects.

The Praclay large scale in situ test was the last analysed experiment. Its complexity is much larger then the other experiments ones, as it includes a liner – host rock interaction, a gallery crossing effect and 3D aspects. A number of progresses obtained in the preceding exercises have been valorised in this simulation. It has been shown the 2D plane strain or axisymetric simulations only partly cover the complexity and that only a 3D anisotropic simulation may allow a full understanding of the tests.

A comparison of some used constitutive models and set of parameters to experimental results show a partial agreement. Comparing the stress paths with the hollow cylinder and Praclay large scale test, some agreement exist but new lab experiments would give some additional information that will be needed for next researches.

Some major conclusions of the numerical simulations are the importance of:

- The initial and induced anisotropy, including stress anisotropy, elastic anisotropy, plastic anisotropy, permeability anisotropy and thermal conductivity anisotropy.
- The cohesion evolution induced by plasticity, damage and thermal loading.
- The permeability induced by strain in the damage zone.

We hope that these themes will be the subject of future funded collaborative projects.

8 List of annexes

Annex 1: Hollow cylinder test in Boom Clay

Annex 2: Hollow cylinder tests on COX argillite

Annex 3: Hollow cylinder tests on Opalinus Clay

Annex 4: In-situ heating test ATLAS in Mol

Annex 5: In-situ dilatometer tests in Mont Terri

Annex 6: Large scale excavation and heater in-situ experiment: the PRACLAY experiment

9 References

Bernier F., Li X.L., Bastiaens W., Ortiz L., Van Geet M., Wouters L., Frieg B., Blümling P.,Desrues J., Viaggiani G., Coll C., Chanchole S., De Greef V., Hamza R., Malinsky L., Vervoort A., Vanbrabant Y., Debecker B., Verstraelen J., Govaerts A., Wevers M., Labiouse V., Escoffier S., Mathier J.-F., Gastaldo L., Bühler Ch. SELFRAC (2006): Fractures And Self-Healing Within The Excavation Disturbed Zone In Clays - Final technical report, EUR 21224, European Commission, Luxembourg

Bernier, F., Li, X.L., Verstricht, J., Barnichon, J.D., Labiouse, V., Bastiaens, W., Palut, J.M., Ben Slimane, J.K., Ghoreychi, M., Gaombalet, J., Huertas, F., Galera, J.M., Merrien, K.and Elorza, F.J. (2003) Clipex: Clay instrumentation programme for the extension of an underground research laboratory. Report EUR 20619 EN. European Commission, Luxembourg.

Bühler Ch. (2005) Selfrac (SE) Experiment: long term dilatometer experiment. Mont Terri Project - Technical Note, TN 99-03

CODE-BRIGHT. A 3D program for thermo-hydro-mechanical analysis in geological media. Users guide, 2004

Collin F., Li X.L., Radu J.-P., Charlier R. Thermo-hydro-mechanical coupling in clay barriers. Engineering geology, 2002, 64, p.179-193

Deliverable 7: Laboratory EDZ-Simulation Tests on Large Hollow Cylinders of the COX Argillite (GRS contribution), within TIMODAZ-WP3.3, 2010

Dujacquier L., Températures admissibles et critères derives pour l'évacuation des déchets chauffants dans l'argile. ONDRAF/NIRAS Memorandum 96-1938, 1996

Garitte B., Vaunat J., Gens A. Determination of the thermal conductivity of the Callovo-Oxfordian clay stone in TER experiment. ANDRA report D.RP.0UPC.09.0002, 2009.

Gens A., Olivella, S. Coupled Thermo-Hydro-Mechanical Analysis of Engineered Barriers for High-Level Radioactive Waste. Chinese Journal of Rock Mechanics and Engineering, 2006, 25(4), 670 -680

Gens A., Vaunat J., Garitte B., Wileveau Y. In situ behaviour of a stiff layered clay subject to thermal loading: oobservations and interpretation. Géotechnique (2007) 57, No. 2, 207-228

Levasseur S., Charlier R., Frieg B., Collin F. Hydro-mechanical modelling of the excavation damaged zone around an underground excavation at Mont Terri Rock Laboratory. International Journal of Rock Mechanics & Mining Sciences (2010) 47, n°3, p.414-425

Mair R.J., Taylor R.N., Clarke B.G. (1992) Repository tunnel construction in deep clay formations, Final report. EUR 13964 EN , Luxembourg: Commission of the European Communities

Olivella S., Alonso E.E. Gas flow through clay barriers. Géotechnique (2008) 58, 3, pp. 157-176

Olivella, S., Carrera, J., Gens A., Alonso, E.E. (1994) Non-isothermal Multiphase Flow of Brine and Gas through Saline media.Transport in Porous Media, 15, 271-293.

Radu J-P, Dizier A., Collin F, Charlier R, Triaxial tests on Boom Clay, TIMODAZ meeting, Grenoble (France), January 2009

Sillen, X., Vietor, T. & Hart, J. (2008). Significance and current handling of the Damaged Zone in Performance Assessment, TIMODAZ Deliverable 4
Su, K., (eds) Analysis of the capacity of numerical models to simulate excavation in deep argillaceous rock. MODEX-REP, Deliverable 1, FIKW-CT2000-00029

Vaunat J., Alonso E.E., Gens A. Constitutive model of short and long term behaviour of the Meuse/Haute-Marne argillite. Deliverable 2&3 of the project MODEX-REP, FIKW-CT2000-00029, 2003

Vaunat J., Gens A. Aspects of modelling geotechnical problems in hard soils and soft argillaceous rocks. Proc. In. Symp. on Numerical Models in Geomechanics, 2004

Vaunat J. Damage-elastoplastic model for argillaceous rocks. CODE-BRIGHT Seminar 2009, GRS Braunschweig